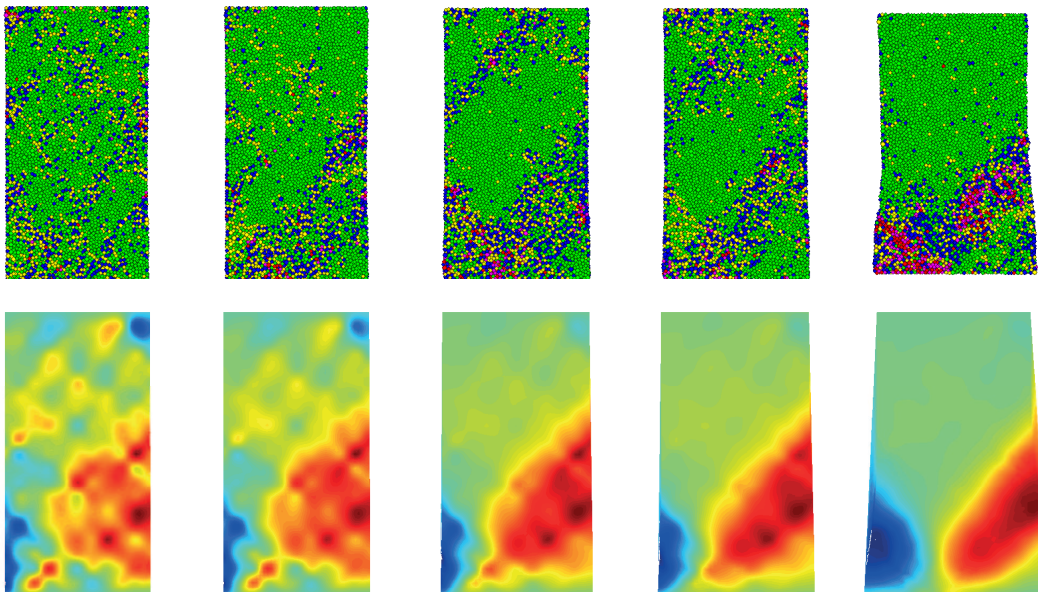


UNIVERSITÄT FÜR BODENKULTUR WIEN

Department für Bautechnik und Naturgefahren
Institut für Geotechnik

Dissertation

Linking DEM with micropolar continuum



Jia Lin
April 2010 - March 2013

UNIVERSITÄT FÜR BODENKULTUR WIEN

Institut für Geotechnik

Definition of tasks

Studiengang: Kulturtechnik und Wasserwirtschaft

Name des Studenten: Jia Lin

Linking DEM with micropolar continuum

Tasks:

This project focuses on the continuum modeling of granular materials with constitutive equations and its relationship to DEM simulations. Some emphasis will be given to the micropolar theory, which is particularly relevant for granular materials with discrete rotating particles. A constitutive model will be developed within the framework of micropolar theory. DEM simulations of element tests will be carried out and the results will be interpreted in the light of micropolar theory.

Erklärung zur Dissertation

Ich, Lin Jia, bestätige hiermit, dass ich die beiliegende Dissertation selbstständig verfasst habe. Ebenso bestätige ich, dass keine anderen als die angegebenen Quellen und Hilfsmittel benutzt wurden.

Wien, November 2012

Declaration of dissertation

I, Lin Jia, hereby confirm, that I write the enclosed dissertation all by myself. I also confirm, that nothing more than the given sources and auxiliary materials are used.

Vienna, November 2012

Acknowledgment

Foremost, I would like to express my sincere gratitude to my advisor Prof. Wei Wu for the continuous support of my PhD study and research. His guidance helped me in all the time of research and writing of this thesis.

Besides my advisor, I would like to thank all other professors and coworkers: Prof. Stefan Ludwig, Prof. Jin Ooi and all the supervisors, experienced researchers and early stage researchers in PARDEM group. I am also thankful to all the coworkers in Institute of Geotechnical Engineering BOKU.

My sincere thanks also goes to Prof. Wenxiong Huang, who offered me his finite element subroutine for his micropolar hypoplastic model implementation.

Finally, I would like to thank the EU Marie Curie actions ITN for the funding, which support my research work for three years.

Contents

Definiteion of tasks	2
1 Introduction	1
1.1 Background	1
1.2 Discrete and continuum methods	2
1.3 Contents	3
2 Discrete element method	4
2.1 Theory	4
2.1.1 Contact laws	5
2.1.2 Calculation procedures	7
2.1.3 Discrete element softwares	8
2.2 Simulations	8
2.2.1 Biaxial test	8
2.2.2 Stress boundary condition	13
2.2.3 Simple shear test	14
2.3 Averaging methods	16
2.3.1 Stress	16
2.3.2 Strain	18
2.3.3 Micropolar terms	20
3 Continuum methods	25
3.1 Introduction	25
3.2 General principles	26

3.3	Constitutive models	29
3.3.1	Hypoplastic model	29
3.3.2	Micropolar theory	38
4	Complex micropolar hypoplastic model	42
4.1	Mathematical background	42
4.1.1	Tensor functions	42
4.1.2	Representation theorem	43
4.1.3	Complex tensor	44
4.2	Complex micropolar hypoplastic model	45
4.2.1	Formulation	45
4.2.2	Assumptions and simplification	47
4.2.3	Discussion of the new model	49
4.3	Expansion of complex formulation method	50
5	Finite element implementation	51
5.1	Finite element method	51
5.2	Background of Abaqus	52
5.3	Implementation	53
6	Result and discussion	57
6.1	Single element simulation	57
6.2	Biaxial test	58
6.3	Pore ratio dependent behavior	63
6.4	Periodic shear test	68
6.5	Simple shear test	70
6.6	Discussion	73
7	Conclusion and outlook	74
7.1	Conclusion	74
7.2	Outlook	77
	Bibliography	82

List of Figures

2.1	Contacts in DEM	6
2.2	General schema of discrete element method	7
2.3	DEM model of biaxial test, model generation	9
2.4	DEM model of biaxial test, loading, $\varepsilon_1 = 0.12$	10
2.5	Stress strain and volume strain curves of the DEM simulation of biaxial test	10
2.6	Ball velocities (left) and contact forces (right) in biaxial simulation from Figure 2.4	11
2.7	Biaxial test simulation with 40000 ($\varepsilon = 0.11$) and 80000 balls ($\varepsilon = 0.08$)	11
2.8	Stress strain and volume strain curves of the DEM simulation of biaxial test with 40000 balls	12
2.9	Stress strain and volume strain curves of the DEM simulation of biaxial test with 80000 balls	12
2.10	Stress boundary condition	13
2.11	Biaxial test simulation with the new stress boundary condition, strain 0.01, 0.02 and 0.0565	14
2.12	Simulation of simple shear test	15
2.13	Simulation result of 2D simple shear test, shear strain 0.03	15
2.14	Simulation result of 3D simple shear test, shear strain 0.045	15
2.15	Stress-strain curve of DEM simulation of 3D simple shear test	16
2.16	Stress averaging	17
2.17	Voronoi-Delaunay tessellation in 3D, colors are used to distinguish different tetrahedrons	19
2.18	A tetrahedron of Voronoi-Delaunay tessellation	20
2.19	Rotation averaging in 2D case	22

2.20	Example for rotation averaging	23
2.21	Different averaging volumes	23
3.1	Stress and couple stress in a 2D continuum element	27
3.2	Stress-strain and volume strain curves of the DEM simulation and hypoplastic model of biaxial test	35
3.3	Stress-strain curves for triaxial compression and extension	36
3.4	Volumetric strain vs. axial strain with different dilatancy angles	36
3.5	Contours for parameter identification	37
5.1	General schema of finite element method	52
5.2	A 2D element for micropolar continuum in Abaqus	53
6.1	Single element simulation in Abaqus	57
6.2	Stress-strain and volume strain curves	58
6.3	FEM model of the biaxial test, normal and soft elements are dark and light gray	59
6.4	FEM simulation results of the biaxial test on undeformed mesh, internal lengths 0.1, 0.25, 0.5, 0.75 and 1.0 mm	60
6.5	FEM simulation results of the biaxial test on deformed shape, internal lengths 0.1, 0.25, 0.5, 0.75 and 1.0 mm, unified deformation and color bar (in radian)	60
6.6	Stress strain curve of the FEM simulation	61
6.7	FEM simulation results of the biaxial test with different mesh size	62
6.8	Relationship between shear band width and internal length	62
6.9	Pore ratio distribution: (a) CT image (b) FEM simulation	63
6.10	FEM simulation results of the biaxial test, vertical strain 0.0073, 0.0146, 0.0219 and 0.0292, colorbar in radian	64
6.11	Contour of norm of incremental displacement ($\sqrt{u^2 + v^2}$) from Digital Image Correlation (DIC). Color bar in mm, vertical strain 0.06	65
6.12	FEM simulation results of the biaxial test with different internal length: (a) 4.2 mm (b) 2.1 mm (c) 1.05 mm (d) 0.42 mm	65
6.13	Periodic boundary conditions in periodic shear test	68
6.14	FEM simulation results of periodic shear, internal lengths 0.2, 0.5, 1.0 and 2.0 mm, rotations are shown by colors	69

6.15 FEM simulation results of periodic shear, internal lengths 0.2, 0.5, 1.0 and 2.0 mm, magnitude of rotations are shown	69
6.16 DEM simulation of simple shear test	70
6.17 FEM model of simple shear test	71
6.18 FEM simulation of simple shear test, colorbar in radian	71
6.19 Shear force of simple shear test	72
6.20 Shear stress of simple shear test	72
7.1 Linking DEM with micropolar continuum	76

List of Tables

2.1	Stresses obtained from different averaging volume inside and outside the shear band.	18
3.1	Material parameters for the DEM simulation of biaxial test	34
3.2	Hypoplastic material parameters for the DEM simulation of biaxial test	34
3.3	Material parameters for hypoplastic model.	35
5.1	Stiffness matrix of micropolar hypoplastic model	56
6.1	Material parameters for the FEM simulation of biaxial test	59
6.2	Material parameters for the FEM simulation of biaxial test with pore ratio dependency	66
6.3	Simulation of biaxial test (a) DEM (b) FEM	67
6.4	Material parameters for the FEM simulation of periodic shear test	68
6.5	Material parameters for the FEM simulation of simple shear test	70

Chapter 1

Introduction

1.1 Background

Granular materials are in abundance in nature and constitute over seventy five percent of all raw material feedstock to industry. Processing, handling and storage of particle systems in the form of granular materials are widespread in all sectors of industry. This includes sand, gravel, plastic pellets, agricultural grains, coal and other minerals, pharmaceutical powders, sugar and flour etc. Many of these industrial solid particle systems display unpredictable behavior and thus are difficult to handle. Problems caused by granular material such as natural disasters or industry material handling issues lead to extensive economic losses.

One of the first studies on granular materials was carried out by researchers in soil mechanics, and was later taken up by many other disciplines, in particular chemical, mechanical mining and food engineers. Due to the complexity of this research field, many physicists and mathematicians are also involved.

There are many open problems to be studied in granular materials. For a single particle, there can be different size, shape, density, roughness, hardness, moment of inertia, crushability, etc. The interactions between particles are also very complicated. They can be hard or soft contact, frictional or frictionless, cohesion or cohesionless, time dependent or time independent, particle fluid interactions, and even long range interactions. All the problems mentioned above are only in particle scales. If we move to macroscale, all these problems increase exponentially, which causes qualitative changes of the material behavior. Hence, modeling of granular material is a very challenging topic and requires comprehensive research works.

The research works in this dissertation focus on different modeling methods for granular materials. The topic is ‘linking DEM with micropolar continuum’, which considers both discrete and continuum methods, the two basic methods of granular material modeling. The aim is to improve both discrete and continuum methods and find links between them.

1.2 Discrete and continuum methods

In order to model granular materials, people follow two different approaches, one is discrete methods on the microscale, the other is continuum modeling on the macroscale. The discrete methods are based on Newton's laws and contact mechanics. They use discrete elements to model individual particles in granular materials. Hence, discrete methods are able to capture the details of microscale material behavior. However, due to the computational complexity, discrete methods are too slow to be used for modeling of the macro scale problems. On the other hand, continuum methods are much faster and simpler for calculations. Continuum methods assume materials to be continuous and use constitutive models to simulate the material behavior. For granular materials, the microstructure behavior can not be very precisely described by existing constitutive models. In summary, discrete methods are more accurate but slow, continuum methods are fast but less accurate. There have been many attempts to link these two methods together. The basic idea in this dissertation is, by using advanced constitutive models, which are hypoplastic and micropolar models, the microstructure of the materials can be better described and similar results as by discrete modeling can be obtained. The most prominent discrete approach is discrete element method (DEM), which is a numerical method used to compute the motion of a large number of particles. In recent decades, the discrete element method (DEM) has been used and advanced extensively for scientific purposes and has increased rapidly our understanding of both macroscopic and microscopic behavior [38, 47]. DEM can be used to simulate a wide variety of granular flow and rock mechanics situations. It also allows a more detailed study of the microscope characteristics than is often impossible using physical experiments.

Continuum methods are conventional approaches to model granular materials, yet problems still exist due to the limitations of constitutive models. Micropolar model is one of the advanced constitutive models which describe the microrotations of materials. By using micropolar continuum, researches [42, 46] have shown that many characteristic behavior of the granular materials such as shear band can be fairly well modeled. However, micropolar models require additional material parameters. A proper way to calibrate these material parameters by experiments does not exist since the material behavior in microscope are very hard to observe or measure. Due to the lack of experimental data, the development of constitutive model needs to follow a mathematical approach, which is one of the main results of this dissertation.

1.3 Contents

The second chapter introduces the theories of discrete element method (DEM) and some benchmark problems simulated with DEM. There is a section in Chapter 2 about averaging methods, which obtain continuum terms from DEM. Chapter 3 describes continuum methods, apart from the basic principles, two important constitutive models are discussed, namely hypoplastic model and micropolar theory. These two models are the basis of the constitutive model developed in this dissertation. Chapter 4 shows the mathematical background and the way to derive the new constitutive model. The finite element (FEM) implementation of the new model is shown in Chapter 5. In Chapter 6, the results of both DEM and continuum modeling is compared and discussed. Finally, in Chapter 7 conclusions and main findings in this dissertation are summarized and an outlook is given.

Chapter 2

Discrete element method

A discrete element method (DEM) is any of family of numerical methods for computing the motion of a large number of particles of micrometer-scale size and above. The basic mechanics of DEM is simply contact mechanics and Newton's second law. However, since the overall behavior of granular materials are model by a large number of discrete particles, accumulative complexities are shown in DEM. The idea of DEM is first given by Cundall [15] in 1979. In the early stage of DEM, only 2D disc elements are realized. Later, 3D ball elements or elements with certain shape (clumps of balls) can be used, which is more similar to the granular material in the real world. With advances in computing power and numerical algorithms for nearest neighbor sorting, it has become possible to numerically simulate millions of particles on a single processor. Today DEM is becoming widely accepted as an effective method of addressing engineering problems in granular and discontinuous materials, especially in granular flows, powder mechanics, and rock mechanics.

2.1 Theory

DEM integrates the motion of a set of discrete particles that represent the individual grains of the material. Given a particle i with position \mathbf{x}_i , angular velocity $\boldsymbol{\omega}_i$ and moment of inertia I_i , Newton's equations of motion are

$$m_i \frac{d^2}{dt^2} \mathbf{x}_i = \mathbf{f}_i + m_i \mathbf{g} \quad (2.1)$$

$$I_i \frac{d}{dt} \boldsymbol{\omega}_i = \mathbf{t}_i \quad (2.2)$$

where \mathbf{f}_i and \mathbf{t}_i are the total forces and torques acting on the particle, given by

$$\mathbf{f}_i = \sum_c \mathbf{f}_i^c \quad (2.3)$$

$$\mathbf{t}_i = \sum_c (\mathbf{l}_i^c \times \mathbf{f}_i^c + \mathbf{q}_i^c) \quad (2.4)$$

where \mathbf{f}_i^c is the contact force between particle i and its particle at contact c and \mathbf{q}_i^c is the torque induced by the contact (i.e. due to rolling or torsion resistance). These equations are numerically integrated over time using techniques such as those described in [3, 43].

2.1.1 Contact laws

The contact forces and torques are specified by the normal and tangential contact forces models, the details of which can depend heavily on the properties of the grains (eg. surface roughness, elasticity, shape, wetting). Numerous examples of contact models exist in the literature. The most commonly used normal contact models are linear contact model and Hertz-Mindlin contact model.

Linear normal contact model results in a force that leads to inelastic collisions requires at least two terms: repulsion and dissipation. The simplest force with the desired properties is the damped harmonic force:

$$F_n = -K_n \delta - B_n \dot{\delta} \quad (2.5)$$

where B_n is a damping constant, K_n is related to the stiffness of a spring whose compression is the overlap δ .

Hertz-Mindlin contact model formulates a more refined force than equation (2.5), one can use the results of the Hertz [27] theory of elastic contacts, which predicts the following repulsive force for the case of spheres:

$$F_n = -K_n \delta^{\frac{3}{2}} \quad (2.6)$$

For the tangential degrees of freedom, there are three different force and torque laws to be implemented: friction, rolling resistance, and torsion resistance [40].

For dynamic (sliding) and static friction, the relative tangential velocity v_t of the contact points is to be considered for the force and torque computations with the total relative velocity of the particle surfaces at the contact.

$$\mathbf{v}_t = \mathbf{v}_{ij} - \mathbf{n}(\mathbf{n} \cdot \mathbf{v}_{ij}) \quad (2.7)$$

$$\mathbf{v}_{ij} = \mathbf{v}_i - \mathbf{v}_j + a'_i \mathbf{n} \times \boldsymbol{\omega}_i + a'_j \mathbf{n} \times \boldsymbol{\omega}_j \quad (2.8)$$

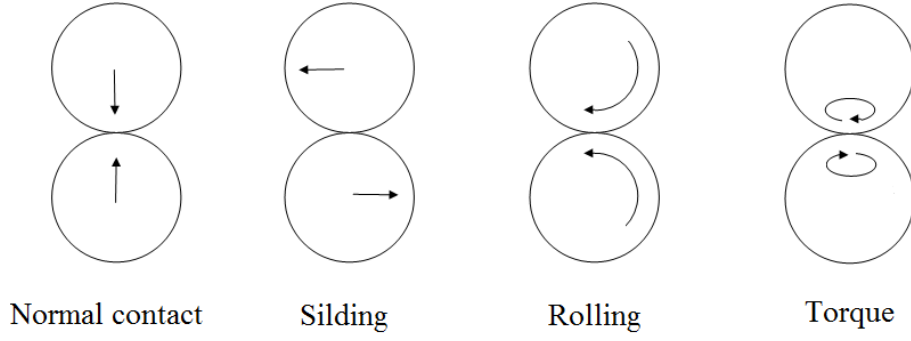


Figure 2.1: Contacts in DEM

where \mathbf{n} is the unit vector pointing from j to i , $\boldsymbol{\omega}_i$ and $\boldsymbol{\omega}_j$ are angular velocities of i and j respectively and a'_α as corrected particle radius relative to the contact point $a'_\alpha = a_\alpha - \delta/2$, for $\alpha = i, j$ and δ is the overlap. Tangential forces acting on the contacting particles are computed from the accumulated sliding of the contact points along each other. Two particles can rotate together, due to both a rotation of the reference frame or a non-central collision. The angular velocity of the rotating reference has a tangential component which is related to the relative velocity, while the normal component is not. Also, tangential forces and torques due to sliding can become active only when the particles are rotating with respect to the common rotating reference frame [40].

The rolling velocity should quantify the distance that two surfaces roll over each other (without sliding). Therefore, it is equal for both particles by definition. An objective rolling velocity is obtained by using the reduced radius:

$$a'_{ij} = \frac{a'_i a'_j}{a'_i + a'_j} \quad (2.9)$$

so that

$$\mathbf{v}_r = -a'_{ij}(\mathbf{n} \times \boldsymbol{\omega}_i - \mathbf{n} \times \boldsymbol{\omega}_j) \quad (2.10)$$

In this case, any common rotation of the two particles vanishes by construction. A more detailed discussion of this issue can be seen in [20, 39] and the references therein. A rolling velocity defined in analogy to the sliding velocity ($\mathbf{n} \times \boldsymbol{\omega}_i - \mathbf{n} \times \boldsymbol{\omega}_j$), would not be objective in general [20, 39], only in the special cases of equal-sized particles or for a particle rolling on a fixed flat surface. A rolling velocity will activate torques, acting against the rolling motion, e.g., when two particles are rotating anti-parallel with spins in the tangential plane. These torques are then equal in magnitude and opposite in direction.

For torsion resistance, the relative spin along the normal direction,

$$\mathbf{v}_o = a_{ij}(\mathbf{n} \cdot \boldsymbol{\omega}_i - \mathbf{n} \cdot \boldsymbol{\omega}_j)\mathbf{n} \quad (2.11)$$

is to be considered, which activates torques when two particles are rotating anti-parallel with spins parallel to the normal direction. Torsion is not activated by a common rotation of the particles around the normal direction, which makes the torsion resistance objective.

In summary, the implementation of the tangential force computations is assumed to be identical, i.e., even the same subroutine is used, but with different parameters. The difference is that friction leads to a force in the tangential plane (changing both translational and angular momentum), while rolling- and torsion-resistance lead to quasi-forces in the tangential plane and the normal direction, respectively, changing the particles angular momentum only. For more details on tangential contact models, friction, rolling and torsion, see [8, 16, 20, 39].

2.1.2 Calculation procedures

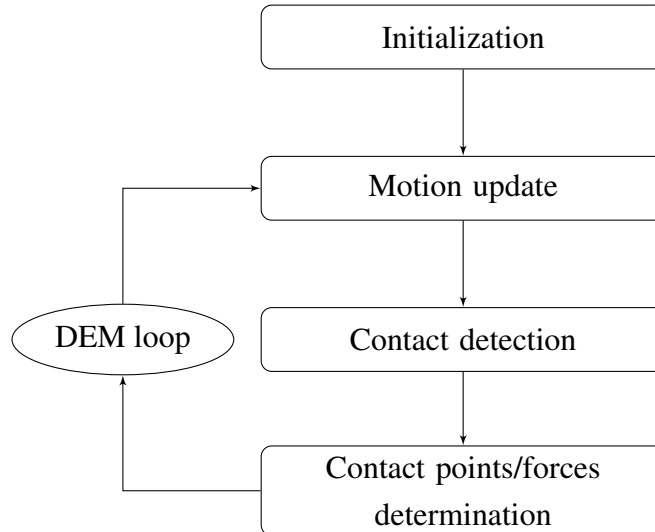


Figure 2.2: General schema of discrete element method

A DEM-simulation is initialized by first generating a model, which results in spatially orienting all particles and assigning an initial velocity (Initialization). In the next step (Motion update), the motion of every object in the simulation is computed. Later we search for pairs of objects which are in contact (Contact detection). The forces which act on each particle pair are computed from the data and the relevant physical laws and contact models (Contact points/forces determination), as shown in Figure 2.2. The critical time step is a half period of the oscillation calculated by:

$$t_{crit} = \frac{\pi}{\omega} \quad (2.12)$$

where

$$\omega = \sqrt{\frac{k}{m} + \left(\frac{b}{2m}\right)^2} \quad (2.13)$$

where t_{crit} is the critical time step, m is the average mass of the discrete element, k is the contact stiffness, b is the damping coefficient. This equation is applied for all contacts and the minimum critical time step is used for DEM loops.

2.1.3 Discrete element softwares

The most commonly used commercial DEM softwares are PFC (particle flow code) by Itasca and EDEM by DEM solutions. A variety of open source DEM programs also exist, such as YADE, LIGGGHTS, etc. Here, PFC 3D 3.10 is used to simulate some element tests for granular materials.

PFC is a discontinuum code used in analysis, testing, and research in any field where the interaction of many discrete objects exhibiting large-strain and/or fracturing is required. Because PFC is not designed to examine a particular type of problem, its range extends to any analysis that examines the dynamic behavior of a particulate system.

2.2 Simulations

2.2.1 Biaxial test

The biaxial test is one of the most commonly used tests in granular mechanics carried out under a plane strain condition. Hence, it is also known as plane strain test. DEM simulations of biaxial tests are carried out in the following, which have three general steps: model generation, isotropic loading and biaxial loading.

First, six walls are generated to apply boundary conditions for the biaxial test, two fixed walls in the plane strain (Y) direction and four walls in perpendicular (X and Z) direction, see Figure 2.3. Then, balls are generated within the area between the walls to model granular materials. For the generation of balls, the radius expansion method is used. First, balls with smaller radius is randomly generated in the space. Then, the radius of balls are expanded to obtain the desired pore ratio. Due to the radius expansion, there are big overlaps between balls. In order to avoid this, several steps of calculations are carried out until a statical state is reached. During the generation of balls, all the walls remain stationary. In this model, there are 15000 balls with a pore ratio of 0.67. Radius of balls are distributed linearly, the ratio of largest to smallest ball radii is 3 : 2. The friction coefficient on the ball surface is 0.577.

The second step is isotropic loading in which the model is loaded to an isotropic stress state

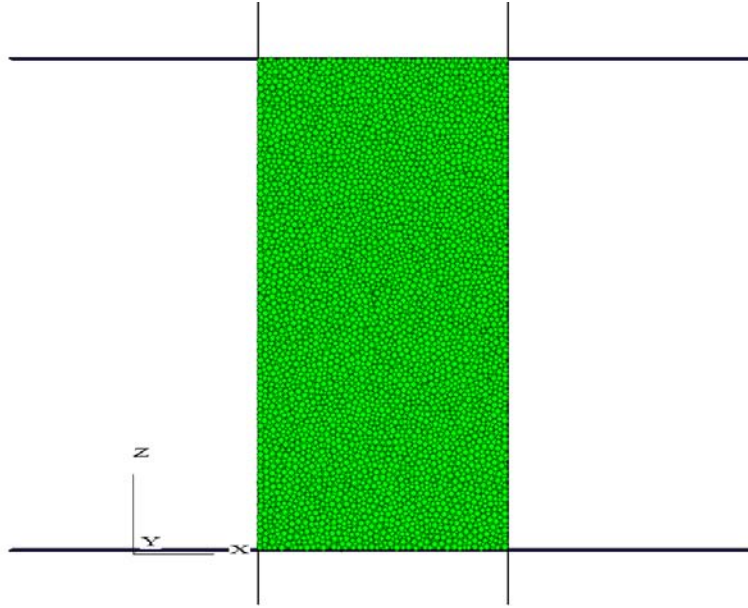


Figure 2.3: DEM model of biaxial test, model generation

in X and Z direction. This is realized by a servo mechanism. If the wall stress is larger than the required stress, the wall will move away from the balls, if the wall stress is smaller than the required stress, the wall will move towards the balls, see equation (2.14).

$$\Delta r = \frac{\alpha A}{k_n^{wall}} (\sigma^{wall} - \sigma^{req}) \quad (2.14)$$

where Δr is the wall displacement, A is the wall area, k_n^{wall} is the contact stiffness on the wall, σ^{wall} and σ^{req} are the wall stress and the required stress, α is a relaxation factor between 0 and 1. k_n^{wall} is calculated by summing the contact stiffness of all the balls in contact with the wall. In this way, the model can be loaded to the required isotropic stress (6000 kPa is used in this simulation), which is the starting point of biaxial loading.

During the biaxial loading, the lower wall is fixed and the upper wall moves down with a constant speed, which applies a constant strain rate in Z direction. The stress on X direction is kept constant by continue applying the servo mechanism (equation (2.14)) on the two walls perpendicular to X direction. With this loading condition, a shear band can be observed from the DEM simulation, see Figure 2.4.

Colors are used to show the rotational speeds in Y direction of each particles. Red and yellow show high and medium rotation in clockwise direction, magenta and blue show high and medium rotation in counterclockwise direction, while green means rotation is almost zero. This color table are also applied to other DEM simulations in this chapter.

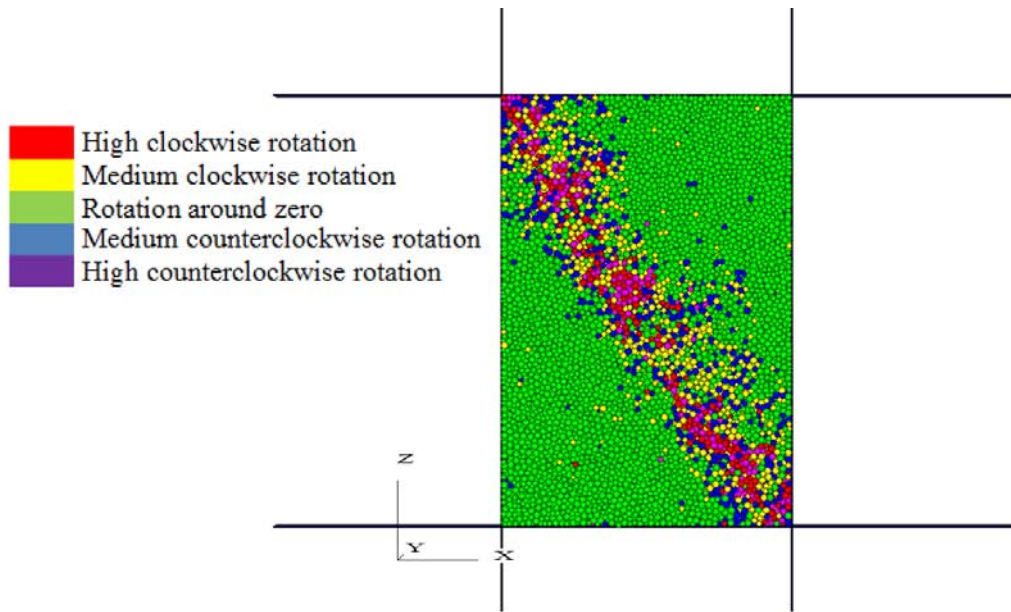


Figure 2.4: DEM model of biaxial test, loading, $\varepsilon_1 = 0.12$

The stress-strain and volume strain curves of the DEM simulation of biaxial test are shown in Figure 2.5, in which σ_1 denotes the stress in Z direction, σ_3 is the stress in x direction, ε_1 is the strain in Z direction and ε_v is the volumetric strain.

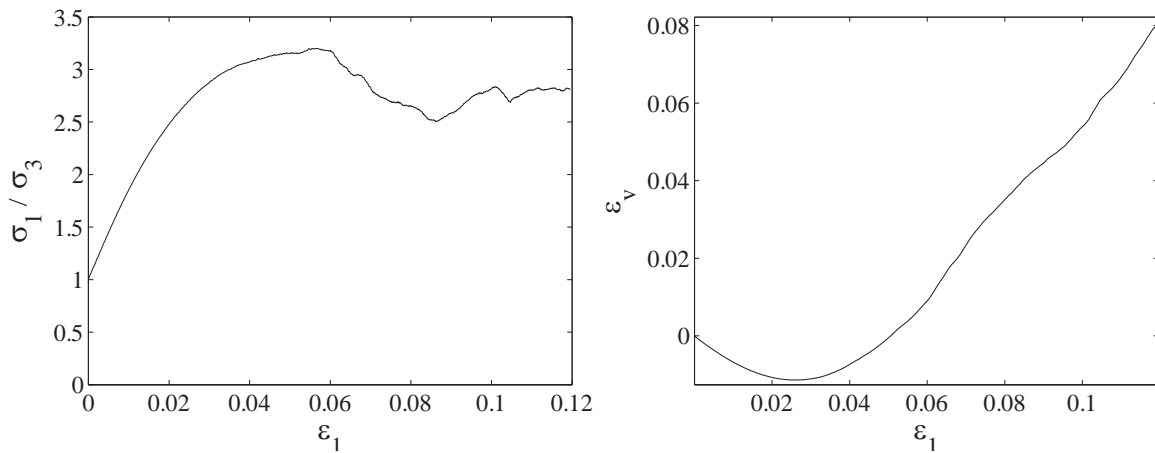


Figure 2.5: Stress strain and volume strain curves of the DEM simulation of biaxial test

It can be seen that the stress-strain behavior and volume strain in biaxial tests can be fairly well predicted by DEM simulations. In the stress-strain relationship, failure point, softening and critical state can be clearly observed.

In addition, some microscale information can be obtained from the DEM simulation. For example, the velocities of individual balls and the contact force net are shown in Figures 2.6.

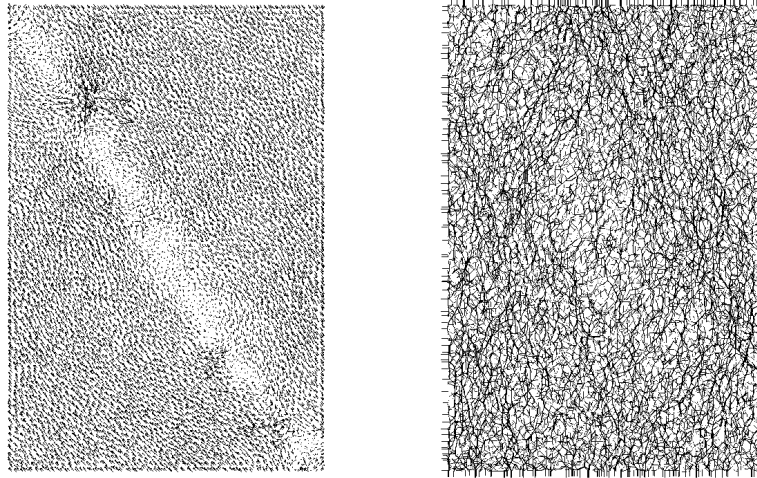


Figure 2.6: Ball velocities (left) and contact forces (right) in biaxial simulation from Figure 2.4

The shear band can be observed from the microstructure of the biaxial test simulation. In the shear band, the particles show large rotation in Y direction and very small moving speed compared to other particles.

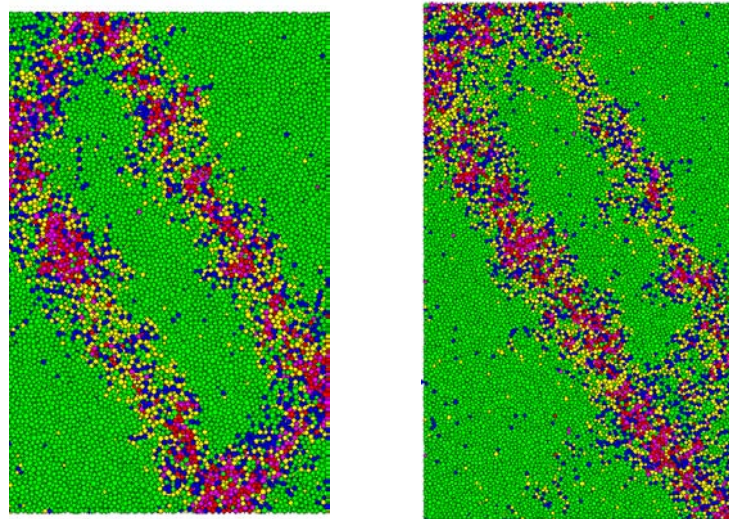


Figure 2.7: Biaxial test simulation with 40000 ($\varepsilon = 0.11$) and 80000 balls ($\varepsilon = 0.08$)

In addition, simulations with 40000 and 80000 balls are carried out with the same material parameters and boundary conditions. Different shear band patterns are found in these simulations, see Figure 2.7. The stress strain curve and volume strain curve of these two simulations

are plotted in Figure 2.8 and 2.9.

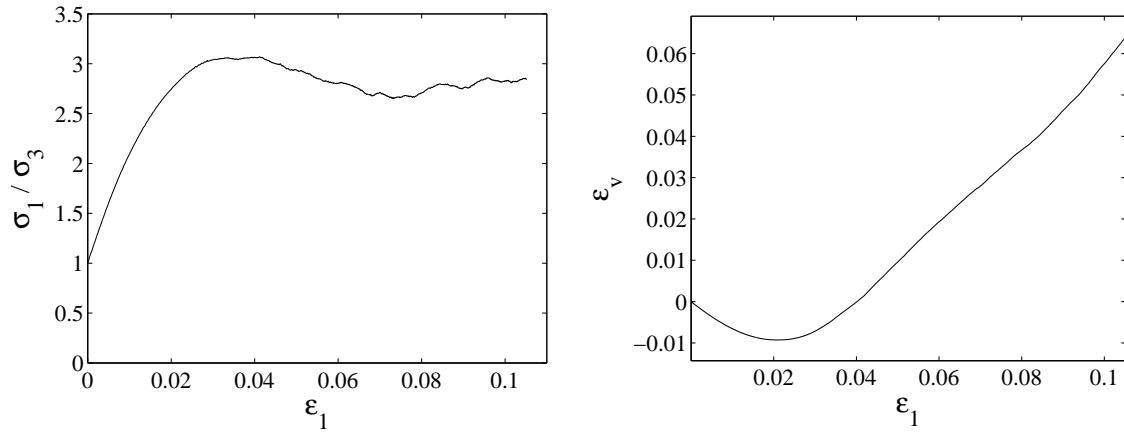


Figure 2.8: Stress strain and volume strain curves of the DEM simulation of biaxial test with 40000 balls

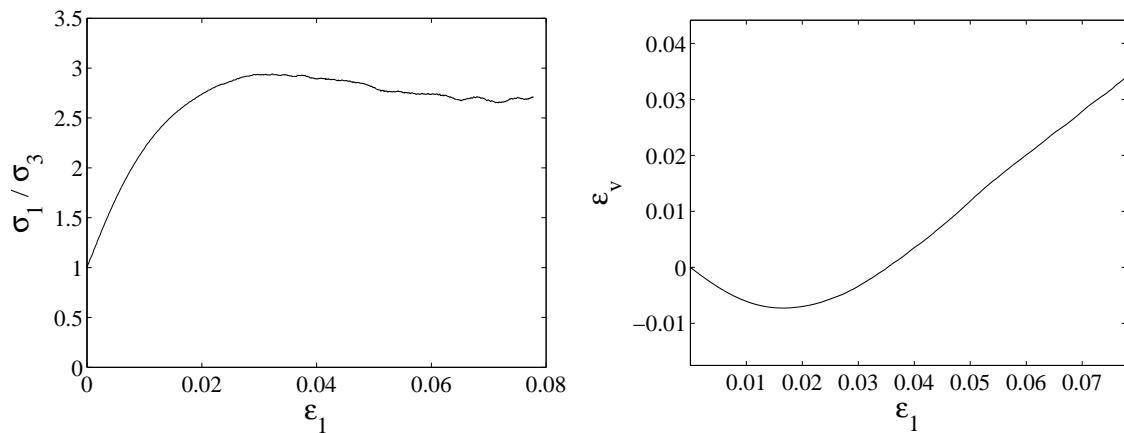


Figure 2.9: Stress strain and volume strain curves of the DEM simulation of biaxial test with 80000 balls

It can be seen that for different particle diameters, the patterns of the shear band are different. The thickness of the shear band is size dependent, for smaller particles, the thickness is smaller. However, the inclination angles of the shear bands are the same for all three simulations. Hence, the shear band angle does not depend on the particle diameter. Also, it can be seen that if a shear band starts from the middle of a rigid wall, a conjugate shear band must exist.

2.2.2 Stress boundary condition

In the DEM simulations of biaxial tests in section 2.2.1, the stress boundary conditions are given by wall elements. However, the walls can not have large deformations. In experiments, the stress boundary conditions are normally applied by rubber bags with hydraulic pressures, which allow large deformations. Hence, the real behavior of stress boundary condition in the biaxial test can not be realized with wall elements.

A novel method of applying stress boundary conditions to DEM simulation is shown here, which can be applied for both plane or cylindrical boundaries. The general steps of this method is shown in the following:

First, the balls on the boundaries are found out. This is done by going through all the contacts on each ball, if all the contact points are in the inside half of the ball, the ball is considered as a ball on the boundary. For example in Figure 2.10 all the boundary balls are shown with red color.

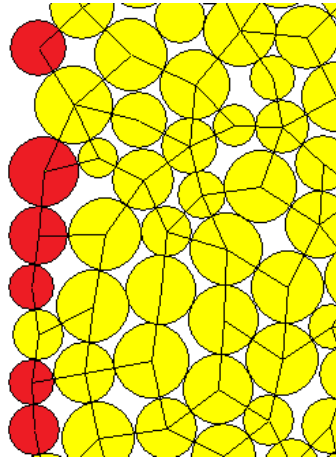


Figure 2.10: Stress boundary condition

Then, a force is applied on the boundary balls according to the radius of the ball.

$$F_b = P\pi r^2 \quad (2.15)$$

where F_b is the force applied on the boundary ball, P is the required pressure of the stress boundary conditions and r is the radius of the ball. In this way, pressures are applied to all the balls on the boundaries

Founding boundary balls and applying load is carried out in each step of the DEM simulation. Since the stress boundary is applied separately on each ball, large deformations are allowed.

With this boundary condition, the biaxial test simulation in section 2.2.1 is carried out again. The stress in horizontal direction is applied with the new method, while in the vertical

direction, wall elements are still used to apply the vertical strain. The results are shown in Figure 2.11.

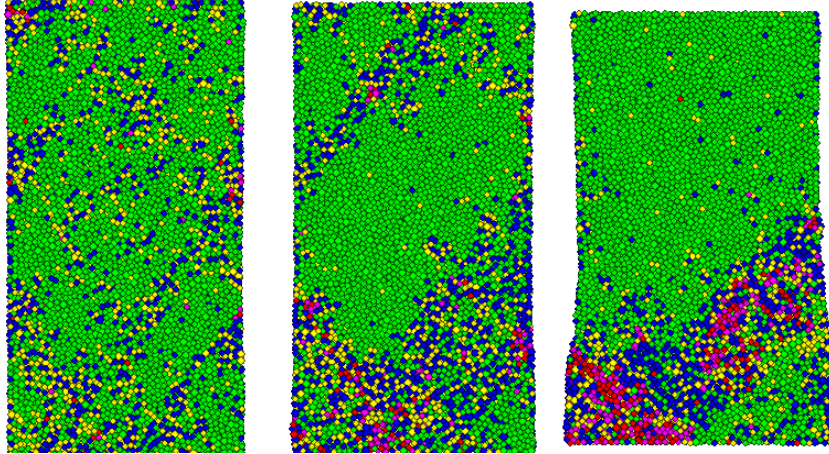


Figure 2.11: Biaxial test simulation with the new stress boundary condition, strain 0.01, 0.02 and 0.0565

It can be seen that the new method allows large deformation on the boundaries. Shear bands can start from the boundary without a conjugate shear band. The simulation result is different from the one using wall boundary conditions in Figure 2.4. Hence, the boundary conditions have a strong effect on the deformation and shear band location in DEM simulations. The result with new boundary condition will be compared with the continuum modeling in section 6.3.

2.2.3 Simple shear test

The simple shear test is an improvement of the direct shear test since the specimen undergoes homogeneous strain from the continuum point of view. The test is conducted by applying a normal stress in oedometeric conditions, then a shear stress is applied and distortions take place until the specimen fails.

Both 2D and 3D DEM simulations are carried out for simple shear test in PFC. The model generation and isotropic loading steps are similar as the simulation of biaxial test described in the section 2.2.1. The simple shear loading is carried out by applying a constant rotation on the two vertical walls, as shown in Figure 2.12.

In the simple shear test, the rotation of particles are shown with different colors in the same way as in biaxial test in section 2.2.1. The result of 2D DEM simulation is shown in Figure

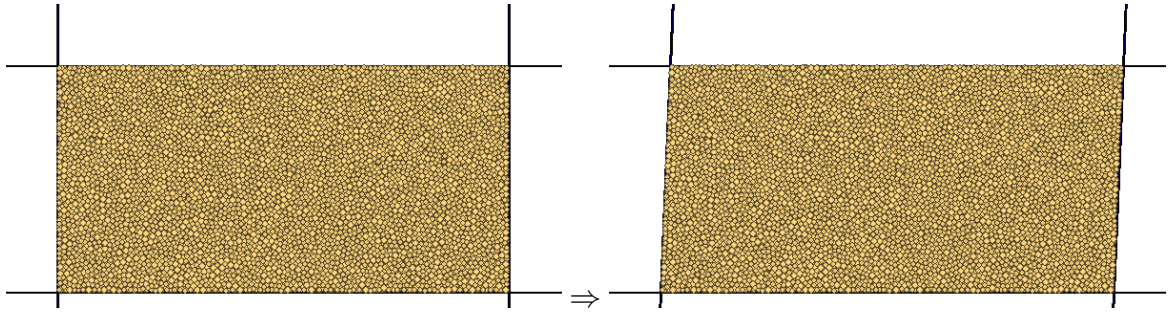


Figure 2.12: Simulation of simple shear test

2.13, 3D DEM simulation is shown in Figure 2.14.

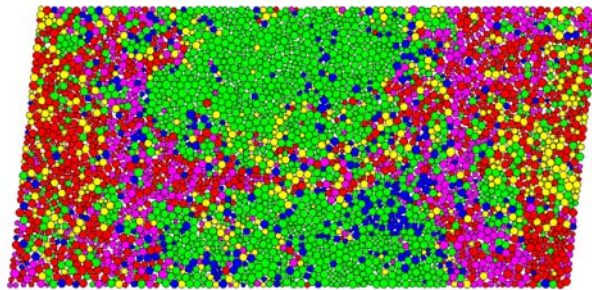


Figure 2.13: Simulation result of 2D simple shear test, shear strain 0.03

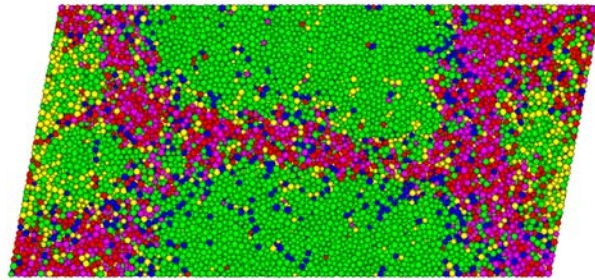


Figure 2.14: Simulation result of 3D simple shear test, shear strain 0.045

It can be seen from the Figures that both 2D and 3D DEM simulation predicted similar particle rotations. In the middle, a shear band with large particle rotations can be observed. Large rotations also occurs in all the corners. For the 3D simulation, the result of stress ratio against shear strain is shown in Figure 2.15, where σ_s is the shear stress, σ_{33} is the constant stress in vertical direction and ε_s is the shear strain.

From the stress-strain curve, it can be seen that during the simple shear process, the shear

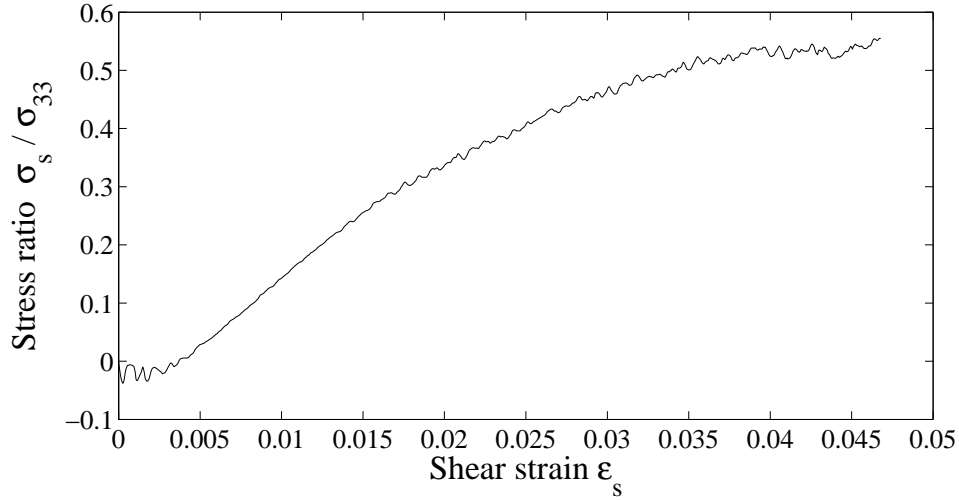


Figure 2.15: Stress-strain curve of DEM simulation of 3D simple shear test

stress keeps increasing until a limited value is reached. This is consistent with the observations in experiments. The result of DEM simulation are be compared with the numerical results of continuum model in section 6.5.

2.3 Averaging methods

Continuum models for particle system were originally derived empirically from experimental tests and are based on mechanical theoretical principles. Continuum models of granular materials are largely conceived out of a need to understand the internal structure of a granular assembly as it has a governing influence on deformation. Since granular materials are discrete in nature, continuum properties need to be obtained by homogenization/averaging methods. In this dissertation, only rate-independent materials are considered, which means the material behavior do not depend on time. Hence, time averaging is not discussed here. In the following sections, only volume averaging methods are considered.

2.3.1 Stress

The macro-micro relationship between the stress tensor and the contact forces has been well established for static conditions. Successive researchers have made advances [7, 4, 33]. Landmark achievements were the addition of body forces by Bagi [4], De Saxce et al.'s consideration of dynamic effects [44] and the derivation of a generalized expression for the

stress tensor based only on Newton's second law by Li et al. [36] in 2009. Here, we use the stress averaging methods to study the stress in the DEM simulations. Since the asymmetry of stress tensor is an important assumption of the micropolar continuum model, which is one of the focal point of this dissertation, the non-symmetry of stress is discussed in the following.

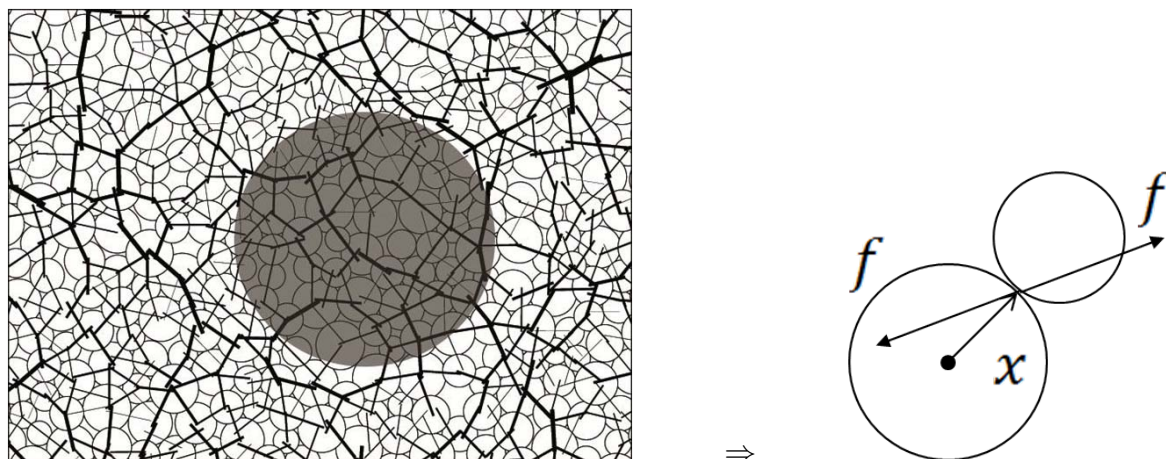


Figure 2.16: Stress averaging

Starting from the biaxial test simulation in the section 2.2.1, we use averaging method to get stresses inside and outside of the shear band with different averaging volumes. The averaging method used here is identical to the method used by Bardet and Vardoulakis in [7], in which:

$$\bar{\sigma}_{ij} = \frac{1}{V} \sum_{e \in E} x_i^{ae} f_j^e \quad (2.16)$$

We go through all the particles within the averaging volume, calculate the volume of these particles within the averaging volume, sum all these volumes to get V . Then, go through all the contacts e in the averaging volume E to get x_i^{ae} and f_j^e , dyadic product of these two vectors give $x_i^{ae} f_j^e$. The sum of $x_i^{ae} f_j^e$ divided by V is the averaged stress $\bar{\sigma}_{ij}$. This method is realized by a FISH program executed in PFC.

With this method, averaging inside and outside the shear band with different averaging lengths (diameter of the averaging volume) are carried out. For balls with shear stiffness, the stress tensors obtained by this averaging method are always asymmetric. Hence, the stress tensor can be separated into a symmetric part and a skew-symmetric part. For the skew-symmetric part, the maximum skew-symmetrical stress can be found. For the symmetrical part the maximum and the minimum principle stresses can be found. For different averaging volumes, the ratio between maximum skew symmetrical stress and maximum principle stress s/σ_1 , and between maximum skew symmetrical stress and minimum principle stress s/σ_3 , are shown in Table 2.1, where d_a is the diameter of the averaging volume and d_{50} is the mean ball diameter.

d_a/d_{50}	inside shear band		outside shear band	
	s/σ_1	s/σ_3	s/σ_1	s/σ_3
4.0	9.03×10^{-3}	2.42×10^{-2}	8.72×10^{-3}	1.74×10^{-2}
2.0	2.15×10^{-2}	1.19×10^{-1}	1.25×10^{-2}	3.99×10^{-2}
1.2	4.81×10^{-2}	8.24×10^{-1}	4.72×10^{-2}	5.99×10^{-1}

Table 2.1: Stresses obtained from different averaging volume inside and outside the shear band.

It is clear from the table that the skew symmetric stress decreases with increasing averaging volume. The larger the averaging volume, the more symmetric the stress tensor. For the same averaging volume, the stress asymmetry inside the shear band is larger, which means that the stress in the shear band is more asymmetric than the stress outside the shear band. Compared to the principle stresses, the asymmetric stress is negligible unless the averaging size approaching the particle size. Hence, from the macroscale point of view, the asymmetry of stress tensor can be neglected.

For granular material with regular shaped particles, i.e. the surface area is small, for an averaging volume, the ratio between volume and surface V/S [7] is proportional to the averaging length. Bardet and Vardoulakis proved that the stress asymmetry decrease with V/S , which is also shown in our DEM simulation and averaging results.

From DEM simulations, it has been proved that the stress asymmetry does exist in granular materials. Consider a continuum constitutive model for granular materials, whether to use a symmetric or asymmetric stress tensor has to be determined. Some researchers use asymmetric stress tensor [10, 12, 28], others suggest the stress asymmetry can be neglected for all practical purposes [13, 15].

Averaging method shows that the stress asymmetry depends on the averaging size, which can be linked to the characteristic length scale in generalized continuum models with size dependency. If the characteristic length is much larger than the mean particle diameter, the stress averaging volume is also very large in which case the stress asymmetry can be neglected. However, if a length scale equivalent to the particle scale is used, the stress asymmetry becomes significant comparing to other stress component. In this case, asymmetric stress tensors should be used to obtain a more precise continuum model.

2.3.2 Strain

The averaging of strain is not as simple as the averaging of stress tensors, since only particles can have stress but both particles and void can have strain. There are two main ways to obtain strain tensors from granular materials. One is the equivalent continua theories [4, 5, 6, 33, 36],

the other is least square best fit theories [37].

Bagi [4, 5, 6] used the Voronoi-Delaunay tessellation concept to describe the geometry of a two-dimensional granular assembly. This method has the advantage of being mathematically versatile, but the drawback of not directly representing the contacts between particles. This hinders the (essential) study of stress-strain relationships.

Significant work has been done by Li and Li [36] who constructed a new two-cell system where particle geometry is described using the Voronoi-Delaunay tessellation. The particle geometry is based on particle contacts, and the void space is split into void cells, whose boundaries form a statically determinant structure.

Durán, Kruyt and Luding [17] extend the equivalent continua method of Bagi to three dimensions and compared it with several best-fit methods. The comparison shows that the equivalent continua method of Bagi is the most accurate one, while the best-fit method based on particles has better performance than the best-fit methods based on contact or edges. In another paper [18], the 3D equivalent continua method of Bagi is studied in detail and the difference between the physical contact and visual Delaunay edges are discussed for isotropically and triaxially deformed granular packing with friction.

The equivalent continua method in three dimensions is realized by carrying out Voronoi-Delaunay tessellation for all selected balls, as shown in Figure 2.17.

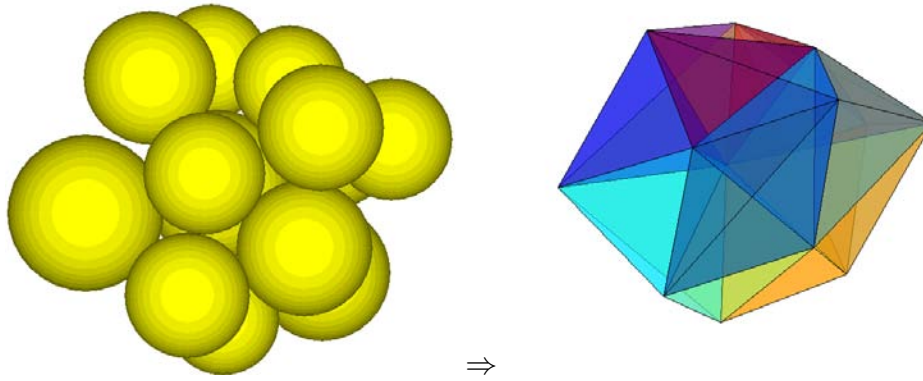


Figure 2.17: Voronoi-Delaunay tessellation in 3D, colors are used to distinguish different tetrahedrons

Then, for each tetrahedron of the Voronoi-Delaunay tessellation, the strain rate tensor D_{ij} can be calculated with the following equations:

$$D_{ij}^L = \frac{1}{V^L} \sum_{k=1}^4 v_i^k a_j^k \quad (2.17)$$

where V^L is the volume of the tetrahedron, v_i^k is the velocity of the k -th particle and a_j^k is a

vector perpendicular to the diagonal face, as shown in Figure 2.18.

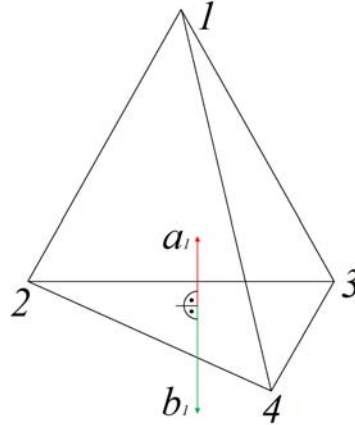


Figure 2.18: A tetrahedron of Voronoi-Delaunay tessellation

In the least square best fit theories, the strain rate tensors are obtained by minimize the error between the predicted average velocities and measured velocities of all balls. The error is given by:

$$z = \sum_N |V_i - v_i|^2 \quad (2.18)$$

where N is the particle number, V_i are the measured particle velocities, v_i is the predicted particle velocities given by:

$$v_i = D_{ij}x_j \quad (2.19)$$

where D_{ij} is the strain rate tensor and x_j is the coordinates of the balls.

In order to minimize the error, we have:

$$\frac{\partial z}{\partial D_{ij}} = 0 \quad (2.20)$$

Hence, D_{ij} can be solved.

The least square best fit theories are widely used due to its simplicity. However, this method is shown to be less accurate than the equivalent continua theories [6].

2.3.3 Micropolar terms

Homogenization methods can also be used to average continuum terms related to micropolar continuum. Details about micropolar continuum can be found in section 3.3.2. If granular materials are considered as micropolar continuum, the stress tensor does not have to be symmetric, and there are more continuum terms, namely the couple stress and the curvature

tensors.

The examples of micropolar homogenization of 2D granular material systems are given by Kruyt [32] and Ehlers et al. [19]. Kruyt presented a theoretical framework of discrete Cosserat (micropolar)-type granular materials for both static and kinematic cases. The homogenization method of Ehlers considers the particles on the boundary of the homogenization volume, the optimized averaging area is found to be five times of the mean grain diameter.

A more general averaging method is proposed for cohesionless particle systems by Zhu et al. [58]. The application of the method to the particle-fluid flow in a gas fluidized bed is studied. The density, velocity stress and couple stress of the flow are examined. A detailed discussion has been conducted to understand the dependence of the averaged variables on sample size.

An important assumption of micropolar theory is that the rotation of individual material point can be different from the continuum rotation. For granular materials, as can be seen from the DEM simulations, the particles in the shear band have larger rotational velocities than other particles. However, the particle rotations are not equal to the rotations of material points in continuum mechanics. Hence, averaging method need to be used.

A new method of rotation averaging for granular material is shown here. This averaging method is quite simple and works from single particle scale to mesoscale. The method is shown in 2D case with circle shaped elements. However, it can be easily extended to 3D or arbitrary shaped elements.

According to Stokes' theorem, the integral over the boundary of some orientable manifold is equal to the integral of its exterior derivative over the whole manifold. Similarly, in averaging method, it is equivalent to consider all the elements inside the averaging volume or to consider all the elements in the averaging boundary. Since rotation is consider here, it is natural to take a sphere or a circle as averaging volume. For other shapes of averaging volume, this method can still be used but becomes very complicated.

First an averaging circle needs to be defined (an averaging sphere in 3D case), the radius of the averaging circle can be chosen arbitrarily. All the particles which intersect with this circle can be found out. If the radius, position, velocity and rotational velocity of these particles are known, the rotational velocity of the averaging circle can be calculated with the following method:

The intersect points of the averaging circle and particles are found out. By knowing the particle velocity and rotation, the velocity of an intersect point can be calculated by:

$$\mathbf{v}_i = \mathbf{v}_p + \boldsymbol{\omega}_p \times \mathbf{r}_{pi} \quad (2.21)$$

where \mathbf{v}_i is the velocity of the intersect point, \mathbf{v}_p is the velocity of the particle center, $\boldsymbol{\omega}_p$ is the rotational velocity of the particle and \mathbf{r}_{pi} is the vector from the particle center to the intersect point.

The velocity \mathbf{v}_i leads to a rotational velocity $\boldsymbol{\omega}_i$ on the averaging circle, which can be given by:

$$\boldsymbol{\omega}_i = \frac{\mathbf{r}_a \times \mathbf{v}_i}{\|\mathbf{r}_a\|^2} \quad (2.22)$$

where \mathbf{r}_a is the vector connecting the center of the averaging circle and the intersect point.

By summing up all the $\boldsymbol{\omega}_i$, the rotational velocity of the averaging circle can be obtained:

$$\boldsymbol{\omega}_a = \sum \frac{\alpha_i}{2\pi} \boldsymbol{\omega}_i \quad (2.23)$$

where α_i is the angle of the intersecting arc of the averaging circle. In this way, the velocity of each intersect point is weighted by the arc length on the averaging circle.

In case of 3D averaging, the similar method can be used except equation (2.23) should be:

$$\boldsymbol{\omega}_a = \sum \frac{1}{2} \sin \frac{\alpha_i}{2} \boldsymbol{\omega}_i \quad (2.24)$$

since the area of the spherical cap equals to $2\pi\|\mathbf{r}_a\|^2 \sin(\alpha_i/2)$, while the area of the whole sphere is $4\pi\|\mathbf{r}_a\|^2$. For arbitrary shaped averaging volume, the determination of surface area is very complicated and will not be discussed here.

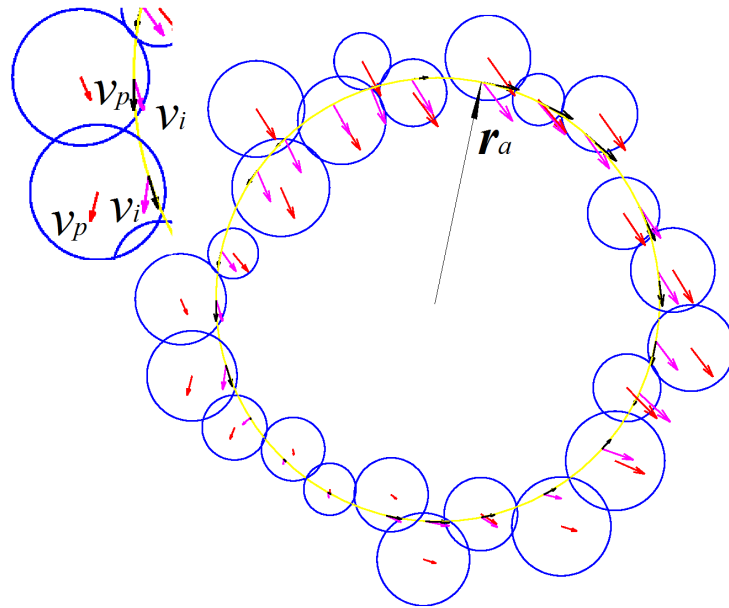


Figure 2.19: Rotation averaging in 2D case

Figure 2.19 shows an example of the averaging method, the small circles are particles and the large circle is the averaging circle. For each particle, there velocities are shown, the particle velocity in the particle center \mathbf{v}_p , the velocity at the intersect point \mathbf{v}_i and the tangential projection of \mathbf{v}_i on the averaging circle. By summing up all the tangential projection velocities,

the rotation of the averaging circle can be obtained.

In order to show the performance of the model, simple cases with different averaging volumes are shown. In Figure 2.20, there are five particles with no translational velocity. The center particle rotates counter-clockwisely and other particles rotate clockwise. The all particles have the same radius r .

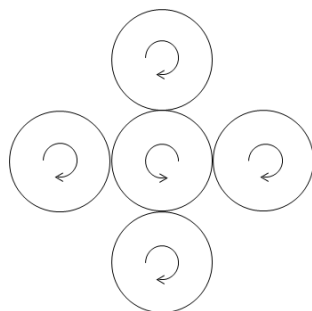


Figure 2.20: Example for rotation averaging

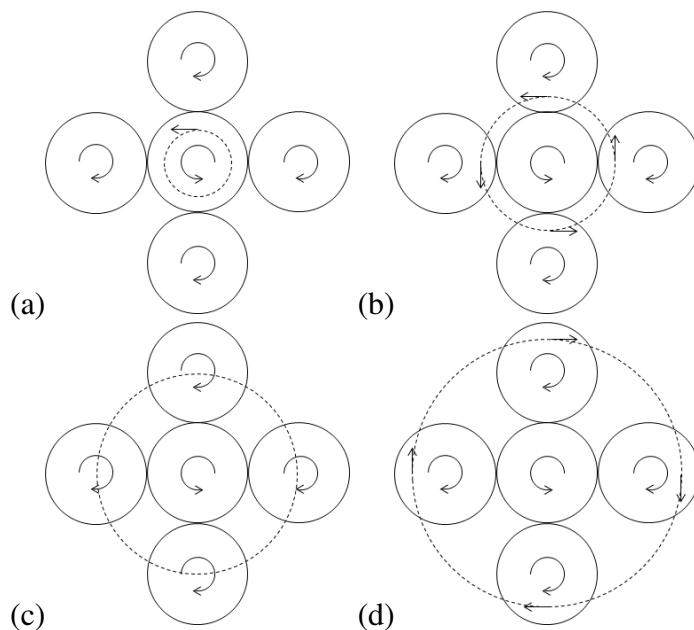


Figure 2.21: Different averaging volumes

Suppose the center of the averaging circle is the same as the center of the middle particle. If the averaging radius is R and $R \leq r$ as shown in Figure 2.21 (a), there is only one intersect point and the intersecting angle is 2π . Hence, the averaged rotation equals to the particle rotation. If $r < R < 2r$ (Figure 2.21 (b)), there are four intersect points. The averaged rotation is counter-clockwise. For the case $R = 2r$ (Figure 2.21 (c)), the intersect velocities are zero, so the averaged rotation is also zero, which means all the rotations within the averaging volume

canceled out. For $R > 2r$ in Figure 2.21(d), the averaged rotation is clockwise.

Using this averaging method, continuum rotation can be averaged from the discrete elements. Depending on the position and size of the averaging circle, the averaged rotation can be different.

Averaging methods bridge the micro and macro scale. It is proved by averaging methods that there are stress asymmetry (only negligible in large scales) and non-affine rotations in granular materials. However, the physical meanings of the couple stress and curvature tensors are not clearly defined. Even for simple granular material in 2D, there are no recognized averaging methods for couple stress and curvature. Choosing a proper averaging volume is also an open question. Hence, to obtain a constitutive relation between couple stress and curvature directly from homogenization method is not feasible.

Chapter 3

Continuum methods

3.1 Introduction

Continuum mechanics is a branch of mechanics that deals with the analysis of the kinematics and the mechanical behavior of materials modeled as a continuous mass rather than as discrete particles. The first and most important assumption in Continuum mechanics is continuity.

Continuity: A material is continuous if it completely fills the space that it occupies, leaving no pores or empty spaces, and if furthermore its properties are describable by continuous functions[41].

Since all materials have microstructures, the continuity assumption is not true as far as the microstructures are considered. However, the bulk behavior of materials shows continuity and can be described by continuous functions. Even though granular materials have a discrete microstructure, the assumption of continuity still holds for many macroscale modelings. Hence, continuum mechanics are still the main methods to model granular materials in most of the engineering problems.

There are two types of functions in continuum mechanics, general principles and constitutive equations. General principles are based on basic physic laws, hold for all kinds of materials. Constitutive equations describes the behavior of certain kind of materials, therefore it is different from one to another. Together with both sets of equations, solutions can be obtained for continuum modeling of material behavior.

3.2 General principles

In this section, general principles in continuum mechanics will be discussed, including kinematics, mechanics, strain and stress measures, conservation laws. Since micropolar continuum is concerned in this dissertation, general formulations (including independent rotations) are shown. Classical general principles can be considered as a special case by setting the independent rotations to zero.

Kinematics: A general material point has three translational degrees of freedom u_i and three rotational degrees of freedom ω_i . Hence, strain tensor and curvature tensor are given by:

$$\mathbf{E} = \begin{pmatrix} \frac{\partial u_1}{\partial x_1} & \frac{1}{2}(\frac{\partial u_1}{\partial x_2} + \frac{\partial u_2}{\partial x_1}) & \frac{1}{2}(\frac{\partial u_1}{\partial x_3} + \frac{\partial u_3}{\partial x_1}) \\ \frac{1}{2}(\frac{\partial u_2}{\partial x_1} + \frac{\partial u_1}{\partial x_2}) & \frac{\partial u_2}{\partial x_2} & \frac{1}{2}(\frac{\partial u_2}{\partial x_3} + \frac{\partial u_3}{\partial x_2}) \\ \frac{1}{2}(\frac{\partial u_3}{\partial x_1} + \frac{\partial u_1}{\partial x_3}) & \frac{1}{2}(\frac{\partial u_3}{\partial x_2} + \frac{\partial u_2}{\partial x_3}) & \frac{\partial u_3}{\partial x_3} \end{pmatrix} \quad (3.1)$$

$$\mathbf{C} = \begin{pmatrix} \frac{\partial \omega_1}{\partial x_1} & \frac{\partial \omega_1}{\partial x_2} & \frac{\partial \omega_1}{\partial x_3} \\ \frac{\partial \omega_2}{\partial x_1} & \frac{\partial \omega_2}{\partial x_2} & \frac{\partial \omega_2}{\partial x_3} \\ \frac{\partial \omega_3}{\partial x_1} & \frac{\partial \omega_3}{\partial x_2} & \frac{\partial \omega_3}{\partial x_3} \end{pmatrix} \quad (3.2)$$

Stain rate tensor, spin tensor and curvature rate tensor can be written as:

$$\mathbf{D} = \begin{pmatrix} \frac{\partial \dot{u}_1}{\partial x_1} & \frac{1}{2}(\frac{\partial \dot{u}_1}{\partial x_2} + \frac{\partial \dot{u}_2}{\partial x_1}) & \frac{1}{2}(\frac{\partial \dot{u}_1}{\partial x_3} + \frac{\partial \dot{u}_3}{\partial x_1}) \\ \frac{1}{2}(\frac{\partial \dot{u}_2}{\partial x_1} + \frac{\partial \dot{u}_1}{\partial x_2}) & \frac{\partial \dot{u}_2}{\partial x_2} & \frac{1}{2}(\frac{\partial \dot{u}_2}{\partial x_3} + \frac{\partial \dot{u}_3}{\partial x_2}) \\ \frac{1}{2}(\frac{\partial \dot{u}_3}{\partial x_1} + \frac{\partial \dot{u}_1}{\partial x_3}) & \frac{1}{2}(\frac{\partial \dot{u}_3}{\partial x_2} + \frac{\partial \dot{u}_2}{\partial x_3}) & \frac{\partial \dot{u}_3}{\partial x_3} \end{pmatrix} \quad (3.3)$$

$$\mathbf{W} = \begin{pmatrix} 0 & \frac{1}{2}(\frac{\partial \dot{u}_1}{\partial x_2} - \frac{\partial \dot{u}_2}{\partial x_1}) & \frac{1}{2}(\frac{\partial \dot{u}_1}{\partial x_3} - \frac{\partial \dot{u}_3}{\partial x_1}) \\ \frac{1}{2}(\frac{\partial \dot{u}_2}{\partial x_1} - \frac{\partial \dot{u}_1}{\partial x_2}) & 0 & \frac{1}{2}(\frac{\partial \dot{u}_2}{\partial x_3} - \frac{\partial \dot{u}_3}{\partial x_2}) \\ \frac{1}{2}(\frac{\partial \dot{u}_3}{\partial x_1} - \frac{\partial \dot{u}_1}{\partial x_3}) & \frac{1}{2}(\frac{\partial \dot{u}_3}{\partial x_2} - \frac{\partial \dot{u}_2}{\partial x_3}) & 0 \end{pmatrix} \quad (3.4)$$

$$\mathbf{K} = \begin{pmatrix} \frac{\partial \dot{\omega}_1}{\partial x_1} & \frac{\partial \dot{\omega}_1}{\partial x_2} & \frac{\partial \dot{\omega}_1}{\partial x_3} \\ \frac{\partial \dot{\omega}_2}{\partial x_1} & \frac{\partial \dot{\omega}_2}{\partial x_2} & \frac{\partial \dot{\omega}_2}{\partial x_3} \\ \frac{\partial \dot{\omega}_3}{\partial x_1} & \frac{\partial \dot{\omega}_3}{\partial x_2} & \frac{\partial \dot{\omega}_3}{\partial x_3} \end{pmatrix} \quad (3.5)$$

Mechanics: For each material point, a stress tensor associated with the translational degrees of freedom and a couple stress tensor associated with the rotational degrees of freedom can be defined. Stress measures the average internal force per unit area within a continuum body. Couple stress measures the average internal moment per unit area within a continuum body. An example of 2D stress and couple stress distribution is shown in Figure 3.1.

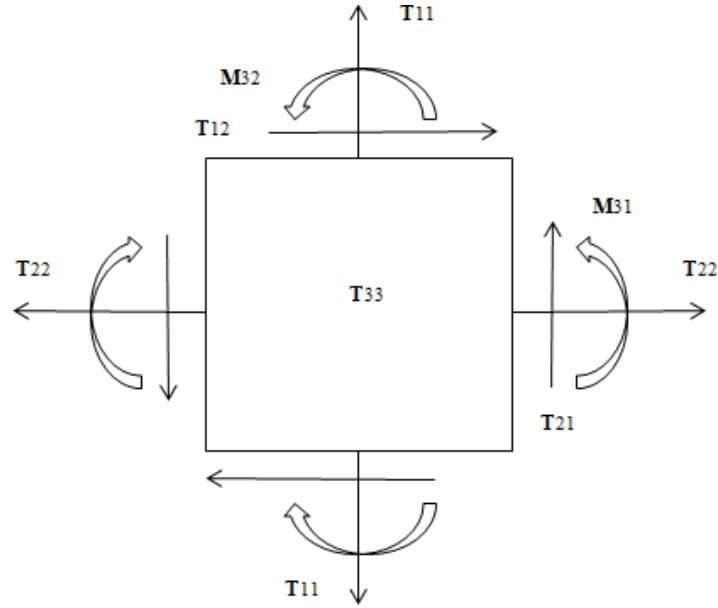


Figure 3.1: Stress and couple stress in a 2D continuum element

For equations given in rate form, stress rate needs to be used. However, the rate of Cauchy stress tensor is not frame independent (objective). Hence, the Jaumann stress rate tensor is normally used, which can be written as:

$$\dot{\mathbf{T}} = \dot{\mathbf{T}} + \mathbf{T}\mathbf{W} - \mathbf{W}\mathbf{T} \quad (3.6)$$

Similarly, the Jaumann couple stress tensor can be defined as:

$$\dot{\mathbf{M}} = \dot{\mathbf{M}} + \mathbf{M}\mathbf{W} - \mathbf{W}\mathbf{M} \quad (3.7)$$

Conservation laws:

Conservation of mass, continuity equation:

$$\frac{d\rho}{dt} + \rho \operatorname{div} \mathbf{v} = 0 \quad (3.8)$$

where ρ is the density and \mathbf{v} is the velocity.

Conservation of momentum:

$$\rho \frac{D\mathbf{v}}{Dt} - \operatorname{div}\mathbf{T} - \rho\mathbf{b} = 0 \quad (3.9)$$

where D/Dt is the material time derivative, \mathbf{T} is the stress tensor and \mathbf{b} is the body force.

Conservation of angular momentum:

$$\rho \frac{D(\mathbf{J}\boldsymbol{\omega})}{Dt} - \operatorname{div}\mathbf{M} - \rho\mathbf{J}\mathbf{c} - \varepsilon\mathbf{T} = 0 \quad (3.10)$$

where \mathbf{J} is the moment of inertia tensor, $\boldsymbol{\omega}$ is the angular velocity, \mathbf{M} is the couple stress tensor, \mathbf{c} is the body couple and ε is the permutation symbol.

For a static system without body force or body couple, from equation (3.9) and (3.10), the following balance equations can be deduced:

$$\mathbf{T}_{ji,j} = 0 \quad (3.11)$$

$$\mathbf{M}_{ji,j} + \varepsilon_{ijk}\mathbf{T}_{jk} = 0 \quad (3.12)$$

Virtual Work principle

If we have a domain Ω with the boundary $\partial\Omega$ and the outward normal vector \mathbf{n} . The domain has a stress of \mathbf{T} and a couple stress of \mathbf{M} . The body force and body couple are given by \mathbf{b} and \mathbf{c} . The force and moment applied on the boundary $\partial\Omega$ are \mathbf{t} and \mathbf{m} . Then, the virtual power can be written in the following form:

$$\begin{aligned} \wp(\mathbf{v}, \boldsymbol{\omega}) &= \int_{\Omega} (\operatorname{div}\mathbf{T} + \rho\mathbf{b} - \rho \frac{D\mathbf{v}}{Dt}) \mathbf{v} dV - \int_{\partial\Omega} (\mathbf{T} \cdot \mathbf{n} - \mathbf{t}) \mathbf{v} dA \\ &+ \int_{\Omega} (\operatorname{div}\mathbf{M} + \rho\mathbf{c} + \varepsilon\mathbf{T} - \rho \frac{D(\mathbf{J}\boldsymbol{\omega})}{Dt}) \boldsymbol{\omega} dV - \int_{\partial\Omega} (\mathbf{M} \cdot \mathbf{n} - \mathbf{m}) \boldsymbol{\omega} dA \end{aligned} \quad (3.13)$$

If the virtual displacement and rotation are assumed to be $\delta\mathbf{u}$ and $\delta\mathbf{r}$, the virtual work can be given by

$$\begin{aligned} \Pi(\delta\mathbf{u}, \delta\mathbf{r}) &= \int_{\Omega} (\operatorname{div}\mathbf{T} + \rho\mathbf{b} - \rho \frac{D\mathbf{v}}{Dt}) \delta\mathbf{u} dV - \int_{\partial\Omega} (\mathbf{T} \cdot \mathbf{n} - \mathbf{t}) \delta\mathbf{u} dA \\ &+ \int_{\Omega} (\operatorname{div}\mathbf{M} + \rho\mathbf{c} + \varepsilon\mathbf{T} - \rho \frac{D(\mathbf{J}\boldsymbol{\omega})}{Dt}) \delta\mathbf{r} dV - \int_{\partial\Omega} (\mathbf{M} \cdot \mathbf{n} - \mathbf{m}) \delta\mathbf{r} dA \end{aligned} \quad (3.14)$$

where the internal work of displacement and rotation are given by $\int_{\Omega} (\operatorname{div}\mathbf{T} + \rho\mathbf{b} - \rho D\mathbf{v}/Dt) \delta\mathbf{u} dV$ and $\int_{\Omega} (\operatorname{div}\mathbf{M} + \rho\mathbf{c} + \varepsilon\mathbf{T} - \rho D(\mathbf{J}\boldsymbol{\omega})/Dt) \delta\mathbf{r} dV$, the external work of displacement and rotation are given by $\int_{\partial\Omega} (\mathbf{T} \cdot \mathbf{n} - \mathbf{t}) \delta\mathbf{u} dA$ and $\int_{\partial\Omega} (\mathbf{M} \cdot \mathbf{n} - \mathbf{m}) \delta\mathbf{r} dA$.

General principles are based on physical laws hence valid for all materials. However, it is not enough to describe the material behavior only with general principles. In addition, constitutive equations are needed, which is the relationship between stress and strain (couple stress and curvature for the micropolar continuum). The main problem of continuum modeling of granular materials is to find proper constitutive models. In the next section, constitutive models are discussed. Hypoplastic model and micropolar theory are shown. In the next chapter, these two theories are combined to obtain a new constitutive model.

3.3 Constitutive models

Before starting with the discussion about constitutive models for granular materials, we need to distinguish the differences between elastic-plastic models and hypoplastic models, and between classical and generalized theories.

Conventional constitutive models such as Drucker-Prager model or Mohr-Coulomb model are based on elastic-plastic theories, which are still the main methods used in engineering problems. In elastic-plastic models, the elastic and plastic deformations need to be distinguished and different material parameters need to be used. Hypoplastic model is a new model developed for granular materials. Unlike elastic-plastic models, there is no clear boundary between elastic and plastic deformations in hypoplastic model. The behavior of material is described with a nonlinear tensor equation and a single set of parameters.

Classical theories assume the material point has only translational degrees of freedom, no internal length scale and not affected by the other material points. Hence, size dependent effects can not be modeled with classical constitutive theories. The most commonly used generalized continuum theories include nonlocal theory, strain gradient theory and micropolar theory.

In this thesis, we take the advantages of both hypoplasticity and micropolar theory by linking them together. In the following sections, hypoplastic model and micropolar theory are introduced separately.

3.3.1 Hypoplastic model

The basic idea of hypoplasticity is developed by Kolymbas in 1985 [30]. He formulated the behavior of an elastic material by using nonlinear tensorial function of the rate-type. Hypoplasticity aims to describe the anelastic phenomena without using the additional notions introduced by elastoplasticity (such as yield surface, plastic potential etc.). Hypoplasticity recognizes that anelastic deformations may set on from the very beginning of the loading process. It does not

presumptively distinguish between elastic and plastic deformations. The outstanding feature of hypoplasticity is its simplicity: it uses only a unique equation (contrary to elastoplasticity) which holds equally for loading and unloading. As with every constitutive equation, there are several versions of hypoplastic equations, early ones and more advanced ones. The original hypoplastic equation given by Kolymbas in 1977 [29] is too complex (at those days the name of hypoplasticity is not introduced). Later some improved versions have been presented ([54, 53, 9, 52]). The general hypoplastic constitutive equation is presented by Wu and Kolymbas in 1990 [54]. Based on the general hypoplastic constitutive equation, a simple hypoplastic constitutive model is proposed by Wu and Bauer in 1994 [53]. This model shows excessive contraction (volume reduction) in triaxial extension. In order to remedy this, the constitutive model is updated by including a new term into the constitutive model.

The formal definition of hypoplasticity is provided by Wu and Kolymbas in 1990 [54] as following:

$$\dot{\mathbf{T}} = \mathbf{H}(\mathbf{T}, \mathbf{D}) \quad (3.15)$$

where \mathbf{T} is the Cauchy stress tensor, \mathbf{D} is the strain rate tensor, $\dot{\mathbf{T}}$ is the Jaumann stress rate defined as

$$\dot{\mathbf{T}} = \dot{\mathbf{T}} + \mathbf{T}\mathbf{W} - \mathbf{W}\mathbf{T} \quad (3.16)$$

where $\dot{\mathbf{T}}$ is the time derivative of the Cauchy stress \mathbf{T} , and \mathbf{W} is the rotation rate (spin vector). Furthermore, the function \mathbf{H} in equation (3.15) is required to be not differentiable in and only in $\mathbf{D} = 0$.

To obtain a concrete formulation, some restrictions are imposed on constitutive equation (3.15). Some of the restrictions are based on the general principles of continuum mechanics, while others are based on experimental observations. The behavior to be described is assumed to be rate-independent. These restrictions are described as following:

1. The function \mathbf{H} should be positively homogeneous of the first order in

$$\mathbf{H}(\mathbf{T}, \lambda\mathbf{D}) = \lambda\mathbf{H}(\mathbf{T}, \mathbf{D}) \quad (3.17)$$

where λ is a positive but otherwise arbitrary scalar.

2. The function \mathbf{H} should fulfill the following condition of objectivity

$$\mathbf{H}(\mathbf{Q}\mathbf{T}\mathbf{Q}^T, \mathbf{Q}\mathbf{D}\mathbf{Q}^T) = \mathbf{Q}\mathbf{H}(\mathbf{T}, \mathbf{D})\mathbf{Q}^T \quad (3.18)$$

where \mathbf{Q} is an orthogonal tensor. The representation theorem for a tensorial function of

two symmetric tensors can be written as follows([45, 48, 49])

$$\begin{aligned} \dot{\mathbf{T}} = & \alpha_0 \mathbf{I} + \alpha_1 \mathbf{T} + \alpha_2 \mathbf{D} + \alpha_3 \mathbf{T}^2 + \alpha_4 \mathbf{D}^2 + \alpha_5 (\mathbf{T}\mathbf{D} + \mathbf{D}\mathbf{T}) \\ & + \alpha_6 (\mathbf{T}^2 \mathbf{D} + \mathbf{D}\mathbf{T}^2) + \alpha_7 (\mathbf{T}\mathbf{D}^2 + \mathbf{D}^2 \mathbf{T}) + \alpha_8 (\mathbf{T}^2 \mathbf{D}^2 + \mathbf{D}^2 \mathbf{T}^2) \end{aligned} \quad (3.19)$$

where \mathbf{I} is the unit tensor. The coefficient α_i ($i = 0, \dots, 8$) are the function of the invariants and joint invariants of \mathbf{T} and \mathbf{D} :

$$\alpha_i = \alpha_i(\text{tr}\mathbf{T}, \text{tr}\mathbf{T}^2, \text{tr}\mathbf{T}^3, \text{tr}\mathbf{D}, \text{tr}\mathbf{D}^2, \text{tr}\mathbf{D}^3, \text{tr}\mathbf{T}\mathbf{D}, \text{tr}\mathbf{T}^2 \mathbf{D}, \text{tr}\mathbf{T}\mathbf{D}^2, \text{tr}\mathbf{T}^2 \mathbf{D}^2) \quad (3.20)$$

where tr represents the trace of a tensor. Note that the isotropy of the tensorial function does not necessarily mean that the response is also isotropic.

3. The function \mathbf{H} should be homogeneous in \mathbf{T} , i.e.

$$\mathbf{H}(\lambda \mathbf{T}, \mathbf{D}) = \lambda^n \mathbf{H}(\mathbf{T}, \mathbf{D}) \quad (3.21)$$

where λ an arbitrary scalar and n denotes the order of homogeneity. This restriction implies that the tangential stiffness is proportional to the n th power of the stress level $(\text{tr}\mathbf{T})^n$, so so that experiments conducted under different stress levels can be normalized by $(\text{tr}\mathbf{T})^n$.

Without loss in generality, it is assumed that the constitutive equation can be decomposed into two parts representing reversible and irreversible behavior of the material:

$$\dot{\mathbf{T}} = \mathbf{L}(\mathbf{T}, \mathbf{D}) - \mathbf{N}(\mathbf{T}, \mathbf{D}) \quad (3.22)$$

where \mathbf{L} is assumed to be linear in \mathbf{D} and \mathbf{N} is non-linear in \mathbf{D} . $\mathbf{L}(\mathbf{T}, \mathbf{D})$ in equation (3.22) can be specified by invoking the representation theorem for isotropic tensorial functions, and the non-linear dependence of \mathbf{N} on \mathbf{D} should also satisfy the restriction of rate-independence. Furthermore, the following generalized hypoplastic equation could be assumed ([55]):

$$\dot{\mathbf{T}} = \mathbf{L}(\mathbf{T}) : \mathbf{D} - \mathbf{N}(\mathbf{T}) \|\mathbf{D}\| \quad (3.23)$$

where $\mathbf{L} = \partial \mathbf{L} / \partial \mathbf{D}$ is, in analogy to the elastic stiffness matrix, a fourth-order tensor. $\|\mathbf{D}\| = \sqrt{\text{tr}\mathbf{D}^2}$ stands for the Euclidean norm. The colon $:$ denotes an inner product between two tensors. It should be noticed that equation (3.23) can describe the relationship of stress rates and strain rates without any predefined yield surface and plastic potential. Another advantage of this hypoplastic model is the decomposition of elastic and plastic parts is not used in developing the constitutive equation. Moreover, there is even no need to define loading and unloading explicitly, since they are implied by the constitutive equation.

The following constitutive equation is proposed by Wu (1992)[51]:

$$\dot{\mathbf{T}} = C_1 \text{tr}(\mathbf{T}) \mathbf{D} + C_2 \frac{\text{tr}\mathbf{T}\mathbf{D}}{\text{tr}\mathbf{T}} \mathbf{T} + C_3 \frac{\mathbf{T}^2}{\text{tr}\mathbf{T}} \|\mathbf{D}\| + C_4 \frac{\mathbf{T}^{*2}}{\text{tr}\mathbf{T}} \|\mathbf{D}\| \quad (3.24)$$

where C_i ($i = 1, 2, 3, 4$) are dimensionless parameters. The deviatoric stress tensor \mathbf{T}^* in the above equation is given by $\mathbf{T}^* = \mathbf{T} - 1/3(\text{tr}\mathbf{T})\mathbf{I}$ with \mathbf{I} being the unit tensor. The four parameters can be identified with a single triaxial compression test. The performance of the model is shown in great detail by Wu and Bauer (1994)[53].

Some studies show that the parameters calibrated for triaxial compression test do not necessarily lead to critical states for other stress paths, e.g. triaxial extension. It is found out that critical state is reached for all paths if the two nonlinear terms are merged into one term by letting (Bauer, 1996[9]):

$$C_3 = -C_4 \quad (3.25)$$

As a consequence, the number of parameters in equation (3.24) reduces from four to three.

$$\dot{\mathbf{T}} = C_1 \text{tr}(\mathbf{T})\mathbf{D} + C_2 \frac{\text{tr}\mathbf{T}\mathbf{D}}{\text{tr}\mathbf{T}}\mathbf{T} + C_3 \|\mathbf{D}\|(\mathbf{T} + \mathbf{T}^*) \quad (3.26)$$

This severely restricts the adaptability of the model. For instance, the initial Poisson ratio cannot be varied. To resolve this problem, a new term $\text{tr}(\mathbf{D})\mathbf{T}$ is added to the above equation so that the number of parameters regains four:

$$\dot{\mathbf{T}} = C_1 \text{tr}(\mathbf{T})\mathbf{D} + C_2 \text{tr}(\mathbf{D})\mathbf{T} + C_3 \frac{\text{tr}\mathbf{T}\mathbf{D}}{\text{tr}\mathbf{T}}\mathbf{T} + C_4 \|\mathbf{D}\|(\mathbf{T} + \mathbf{T}^*) \quad (3.27)$$

Note that the same notations for the four parameters are retained in the above equation. Obviously this new term vanishes in critical state with $\text{tr}(\mathbf{D}) = 0$. The new term is motivated by a similar term proposed by Wu in 1999 [52]. This model is studied in the PHD thesis of Wang [50] and applied to numerical modeling of tunneling.

The four parameters in constitutive equation (3.27) can be identified with a single triaxial compression test under constant confining pressure. The stress rate, stress and strain rate tensors at the starting point $(\dot{\mathbf{T}}_i, \mathbf{T}_i, \mathbf{D}_i)$ and failure point $(\dot{\mathbf{T}}_f, \mathbf{T}_f, \mathbf{D}_f)$ of a triaxial test are:

$$\dot{\mathbf{T}}_i = \begin{pmatrix} \dot{\sigma}_i & 0 & 0 \\ 0 & 0 & 0 \\ 0 & 0 & 0 \end{pmatrix}, \mathbf{T}_i = \begin{pmatrix} \sigma_c & 0 & 0 \\ 0 & \sigma_c & 0 \\ 0 & 0 & \sigma_c \end{pmatrix}, \mathbf{D}_i = \begin{pmatrix} \dot{\epsilon}_{1i} & 0 & 0 \\ 0 & \dot{\epsilon}_{3i} & 0 \\ 0 & 0 & \dot{\epsilon}_{3i} \end{pmatrix} \quad (3.28)$$

$$\dot{\mathbf{T}}_f = \begin{pmatrix} 0 & 0 & 0 \\ 0 & 0 & 0 \\ 0 & 0 & 0 \end{pmatrix}, \mathbf{T}_f = \begin{pmatrix} \sigma_f & 0 & 0 \\ 0 & \sigma_c & 0 \\ 0 & 0 & \sigma_c \end{pmatrix}, \mathbf{D}_f = \begin{pmatrix} \dot{\epsilon}_{1f} & 0 & 0 \\ 0 & \dot{\epsilon}_{3f} & 0 \\ 0 & 0 & \dot{\epsilon}_{3f} \end{pmatrix} \quad (3.29)$$

With equation (3.27), four independent equations can be obtained:

$$\dot{\sigma}_i = C_1 3\sigma_c \dot{\varepsilon}_{1i} + C_2 (\dot{\varepsilon}_{1i} + 2\dot{\varepsilon}_{3i}) \sigma_c + C_3 \frac{\sigma_c (\dot{\varepsilon}_{1i} + 2\dot{\varepsilon}_{3i})}{3\sigma_c} \sigma_c + C_4 \sqrt{\dot{\varepsilon}_{1i}^2 + 2\dot{\varepsilon}_{3i}^2} \sigma_c \quad (3.30)$$

$$0 = C_1 3\sigma_c \dot{\varepsilon}_{3i} + C_2 (\dot{\varepsilon}_{1i} + 2\dot{\varepsilon}_{3i}) \sigma_c + C_3 \frac{\sigma_c (\dot{\varepsilon}_{1i} + 2\dot{\varepsilon}_{3i})}{3\sigma_c} \sigma_c + C_4 \sqrt{\dot{\varepsilon}_{1i}^2 + 2\dot{\varepsilon}_{3i}^2} \sigma_c \quad (3.31)$$

$$0 = C_1 (\sigma_f + 2\sigma_c) \dot{\varepsilon}_{1f} + C_2 (\dot{\varepsilon}_{1f} + 2\dot{\varepsilon}_{3f}) \sigma_f + C_3 \frac{(\sigma_f \dot{\varepsilon}_{1f} + 2\sigma_c \dot{\varepsilon}_{3f})}{\sigma_f + 2\sigma_c} \sigma_f \quad (3.32)$$

$$+ C_4 \sqrt{\dot{\varepsilon}_{1f}^2 + 2\dot{\varepsilon}_{3f}^2} (\sigma_f + \sigma_c - \frac{\sigma_f + 2\sigma_c}{3})$$

$$0 = C_1 (\sigma_f + 2\sigma_c) \dot{\varepsilon}_{3f} + C_2 (\dot{\varepsilon}_{1f} + 2\dot{\varepsilon}_{3f}) \sigma_c + C_3 \frac{(\sigma_f \dot{\varepsilon}_{1f} + 2\sigma_c \dot{\varepsilon}_{3f})}{\sigma_f + 2\sigma_c} \sigma_c \quad (3.33)$$

$$+ C_4 \sqrt{\dot{\varepsilon}_{1f}^2 + 2\dot{\varepsilon}_{3f}^2} (\sigma_c + \sigma_c - \frac{\sigma_f + 2\sigma_c}{3})$$

The material parameters measured in a triaxial test can be given by:

$$E_i = \frac{\dot{\sigma}_i}{\dot{\varepsilon}_{1i}} \quad (3.34)$$

$$\nu_i = \frac{\dot{\varepsilon}_{3i}}{\dot{\varepsilon}_{1i}} \quad (3.35)$$

$$\phi = \arcsin\left(\frac{\sigma_f - \sigma_c}{\sigma_f + \sigma_c}\right) \quad (3.36)$$

$$\nu_f = \frac{\dot{\varepsilon}_{3f}}{\dot{\varepsilon}_{1f}} = \frac{1 + \tan \psi}{2} \quad (3.37)$$

where E_i is the initial Young's modulus, ν_i is the initial Poisson ratio, ϕ is the friction angle, ν_f is the failure Poisson ratio, ψ is the dilatancy angle. In addition, a stress ratio R_f is assumed, which is given by:

$$R_f = \frac{\sigma_f}{\sigma_c} = \frac{1 + \sin \phi}{1 - \sin \phi} \quad (3.38)$$

Hence, equation array 3.30 can be simplified to:

$$\frac{E_i}{\sigma_c} = 3C_1 + C_2(1 + 2\nu_i) + C_3 \frac{1 + 2\nu_i}{3} - C_4 \sqrt{1 + 2\nu_i^2} \quad (3.39)$$

$$0 = 3C_1 \nu_i + C_2(1 + 2\nu_i) + C_3 \frac{1 + 2\nu_i}{3} - C_4 \sqrt{1 + 2\nu_i^2} \quad (3.40)$$

$$0 = C_1(R_f + 2) + C_2(1 + 2\nu_f)R_f + C_3 \frac{R_f + 2\nu_f}{R_f + 2} R_f - C_4 \sqrt{1 + 2\nu_f^2} \frac{5R_f - 2}{3} \quad (3.41)$$

$$0 = C_1(R_f + 2)\nu_f + C_2(1 + 2\nu_f) + C_3 \frac{R_f + 2\nu_f}{R_f + 2} + C_4 \sqrt{1 + 2\nu_f^2} \frac{R_f - 4}{3} \quad (3.42)$$

If $E_i, \nu_i, \phi(R_f), \nu_f(\psi)$ are known, parameters $C_1 - C_4$ can be obtained by solving the following equation system:

$$\begin{pmatrix} \frac{E_i}{\sigma_c} \\ 0 \\ 0 \\ 0 \end{pmatrix} = \begin{pmatrix} 3 & (1 + 2\nu_i) & \frac{1 + 2\nu_i}{3} & -\sqrt{1 + 2\nu_i^2} \\ 3\nu_i & (1 + 2\nu_i) & \frac{1 + 2\nu_i}{3} & -\sqrt{1 + 2\nu_i^2} \\ (R_f + 2) & (1 + 2\nu_f)R_f & \frac{R_f + 2\nu_f}{R_f + 2}R_f & -\sqrt{1 + 2\nu_f^2}\frac{5R_f + 2}{3} \\ (R_f + 2)\nu_f & (1 + 2\nu_f) & \frac{R_f - 2\nu_f}{R_f + 2} & \sqrt{1 + 2\nu_f^2}\frac{R_f - 4}{3} \end{pmatrix} \begin{pmatrix} C_1 \\ C_2 \\ C_3 \\ C_4 \end{pmatrix} \quad (3.43)$$

For example, material parameters of the DEM simulation of biaxial test in the subsection 2.2.1 Figure 2.5 can be calibrated, the results are shown in Table 3.1.

$E(\text{MPa})/\sigma_c$	R_f	$\psi(^{\circ})$	ν_i
90	4.25	56.14	0

Table 3.1: Material parameters for the DEM simulation of biaxial test

With equation (3.43), the hypoplastic material parameters can be determined as shown in Table 3.2.

C_1	C_2	C_3	C_4
-30.00	62.65	-446.07	-86.04

Table 3.2: Hypoplastic material parameters for the DEM simulation of biaxial test

Hence, an analytical calculation of biaxial test can be carried out. The resulting stress-strain and volume strain curves are compared with the result of DEM simulations as shown in Figure 3.2.

From the comparison, it can be seen that with proper material parameters, the result of DEM simulation can be fairly well reproduced by hypoplastic model.

Further more, for $\sigma_c = 100$ KPa, different material parameters can be calibrated as shown in Table 3.3.

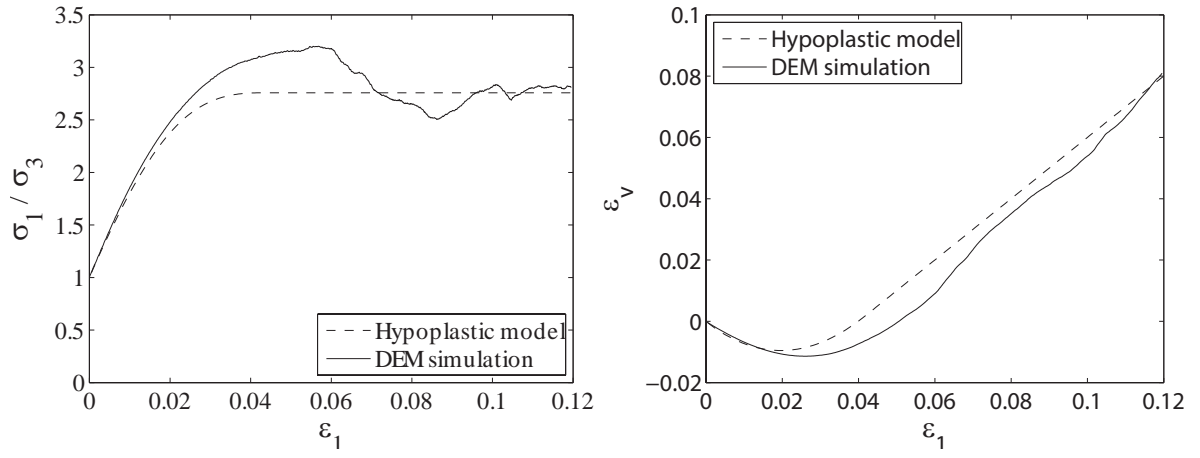


Figure 3.2: Stress-strain and volume strain curves of the DEM simulation and hypoplastic model of biaxial test

$E(\text{MPa})/\sigma_c$	$\phi(^{\circ})$	$\psi(^{\circ})$	ν_i	C_1	C_2	C_3	C_4
170	30	0	0	-56.67	3.58	-531.25	-173.51
			0.1	-51.52	-57.46	-482.95	-157.73
			0.2	-47.22	-150.09	-442.71	-144.59
			0.3	-43.59	-324.31	-408.65	-133.47
		10	0	-56.67	37.23	-653.65	-180.66
			0.1	-51.52	-19.91	-620.22	-164.23
			0.2	-47.22	-104.56	-610.25	-150.55
			0.3	-43.59	-261.16	-642.91	-138.97
		20	0	-56.67	71.79	-774.44	-186.35
			0.1	-51.52	18.74	-755.79	-169.41
			0.2	-47.22	-57.56	-775.94	-155.30
			0.3	-43.59	-195.74	-874.89	-143.35
		30	0	-56.67	108.88	-899.62	-191.00
			0.1	-51.52	60.27	-896.37	-173.63
			0.2	-47.22	-6.94	-947.87	-159.16
			0.3	-43.59	-125.12	-1115.84	-146.92

Table 3.3: Material parameters for hypoplastic model.

Several Numerical simulations of triaxial compression and extension tests with different dilatancy angles are carried out. The results of stress-strain curves and different volume strain curves are shown in Figure 3.3 and 3.4.

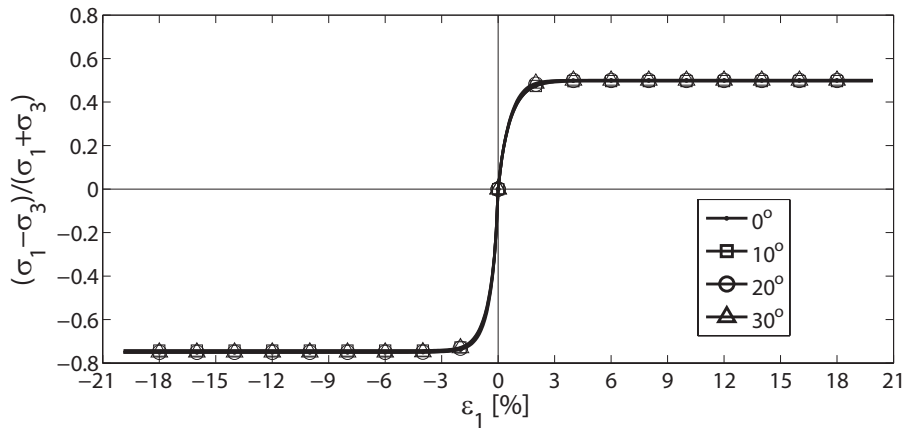


Figure 3.3: Stress-strain curves for triaxial compression and extension

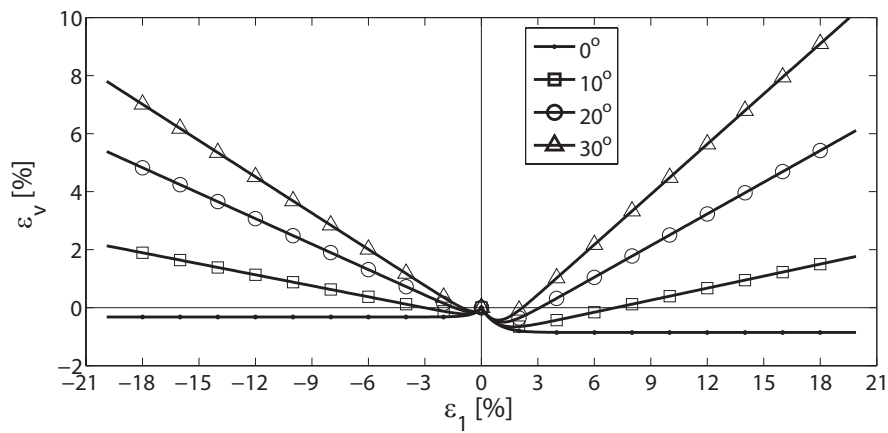


Figure 3.4: Volumetric strain vs. axial strain with different dilatancy angles

In Case of vanishing initial Poisson ratio ($\nu_i = 0$), the contour plot of relationship between different parameters are shown in Figures 3.5.

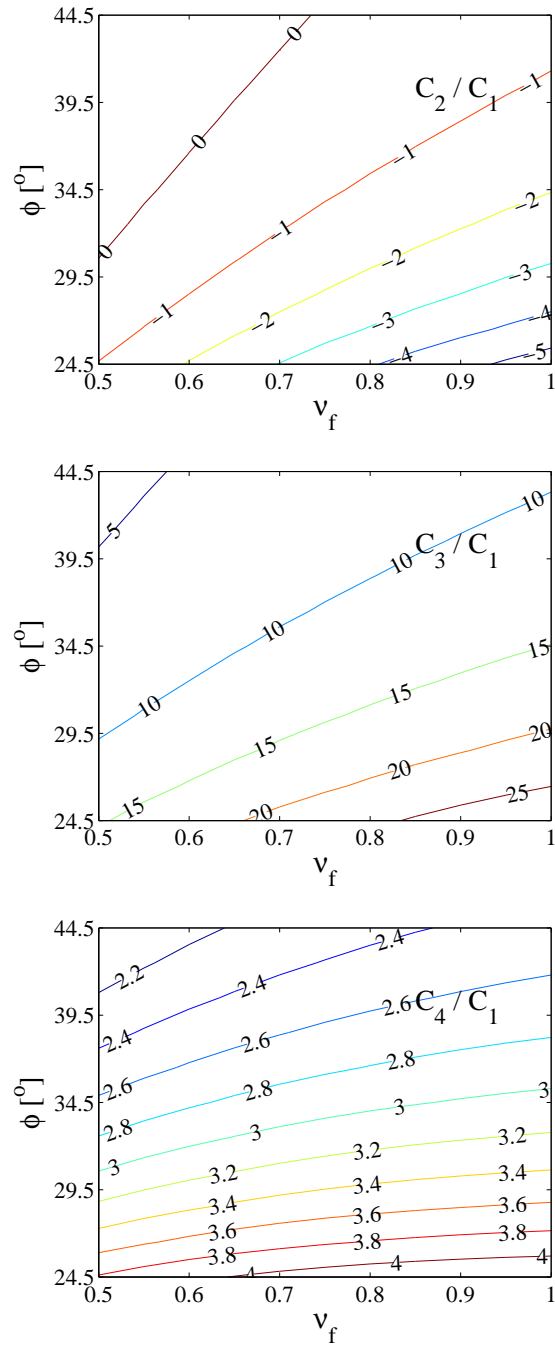


Figure 3.5: Contours for parameter identification

3.3.2 Micropolar theory

Generalized continuum theories have characteristic lengths in the constitutive model and can be used to solve size dependent problems. The most commonly used generalized continuum theories include nonlocal theory, strain gradient theory and micropolar theory. Micropolar theory is also known as Cosserat theory since it is first developed by the Cosserat brothers [14] in 1909. However, their work is very general and does not use tensor notations, and they did not give any constitutive relations. Later the Cosserat theory is presented by Ericksen and Truesdell in [21]. The importance of Cosserat theory is widely noticed in the 1968 Freudenstadt-IUTAM-Symposium on the Mechanics of Generalized Continua edited by Kröner [31]. An extensive presentation of the Cosserat theory is given by Eringen [22, 23], and he named Cosserat theory as micropolar theory.

Classical continuum methods consider a continuous material to be made up of an assemblage of points that can displace linearly in any direction when a force is applied. The response of the material to an applied surface stress is to move in a straight line in the direction of the stress. This behavior is described by the Cauchy stress tensor and assumes that a force's movement through the material can be described completely as a vector. It neglects couple stresses and does not consider the moments that are induced from locally varying strain conditions. Such a model may be insufficient for the description of certain physical phenomena. Particle rotations and the associated frictional work have been shown to dominate a granular material's behavior. Therefore, if granular materials need to be accurately described, a model that can deal with the discrete rotation of each point as well as its translation will be needed.

In a micropolar continuum, the micro rotations of material points needs to be considered. Hence, an internal length and other material parameters linked to the microstructure of the material needs to be determined. However, unlike macro scale material parameters, the micro scale material parameter cannot be easily determined with experiments. Lakes [35, 34] showed some experimental methods for elastic micropolar continuum. These experiments are quite complicate and only works for materials such as metal. For granular materials, there is no standard experiment for micropolar theory, and no recognized definition of the length scale. As discussed in section 2.3.3, obtaining a micropolar constitutive model from DEM and averaging method is also not feasible. Hence, in this stage, setting up a constitutive model based on experimental data or discrete methods is not possible, mathematical approaches need to be followed.

Regarding the existing constitutive models of micropolar theory, there are micropolar elasticity, micropolar plasticity and micropolar hypoplasticity.

Micropolar elasticity: The micropolar elasticity is well defined, which has the following

form:

$$\mathbf{T}_{ij} = \lambda \mathbf{E}_{kk} \delta_{ij} + 2\mu \mathbf{E}_{(i,j)} + 2\mu_c \mathbf{E}_{\{i,j\}} \quad (3.44)$$

$$\mathbf{M}_{ij} = \alpha \mathbf{C}_{kk} \delta_{ij} + 2\beta \mathbf{C}_{(i,j)} + 2\gamma \mathbf{C}_{\{i,j\}} \quad (3.45)$$

where \mathbf{T} , \mathbf{E} , \mathbf{M} and \mathbf{C} are stress, strain, couple stress and curvature tensors. \mathbf{E}_{kk} is the spherical part of tensor \mathbf{E} . $\mathbf{E}_{(i,j)}$ and $\mathbf{E}_{\{i,j\}}$ respectively denote the symmetric and skew-symmetric part of \mathbf{E}_{ij} . λ and μ are classical Lamé constants. μ_c , α , β and γ are additional material parameters for micropolar elasticity. Several length scales can be defined, such as:

$$l_1^2 = \frac{(\mu + \mu_c)(\beta + \gamma)}{4\mu\mu_c} \quad (3.46)$$

$$l_2^2 = \frac{\alpha + 2\beta}{4\mu_c} \quad (3.47)$$

Micropolar plasticity: There are still many unsolved questions in micropolar plasticity. Due to the micro rotation of material, the classical yield criteria and flow rules cannot be applied directly. The yield condition depends on both stress and couple stress:

$$F = \sqrt{a_1 \mathbf{S}_{ij} \mathbf{S}_{ij} + a_2 \mathbf{S}_{ij} \mathbf{S}_{ji} + b_1 \mathbf{M}_{ij} \mathbf{M}_{ij} + b_2 \mathbf{M}_{ij} \mathbf{M}_{ji}} - Y \quad (3.48)$$

where \mathbf{S} is the deviatoric stress tensor. a_1 , a_2 , b_1 and b_2 are material parameters and Y is the isotropic hardening variable, which can be a function of mean stress. In [42], Y is given by:

$$Y = \mu |p| = \sin \phi_m |p| \quad (3.49)$$

where p is the mean stress, μ is the friction coefficient and ϕ_m is the friction angle.

From the equations above, it can be seen that there are many additional parameters for micropolar elasticity and plasticity. The physical meaning of these parameters is not clear yet and there is no simple experiment to achieve all these parameters.

Micropolar hypoplasticity: A different approach is to link micropolar theory with hypoplasticity. Based on the hypoplastic model given by Gudehus [25] and Bauer [9], a micropolar hypoplastic model is given by Tejchmann and Bauer [46]:

$$\dot{\mathbf{T}} = f_s[\mathbf{L}(\hat{\mathbf{T}}, \hat{\mathbf{m}}, \mathbf{D}_c, \mathbf{k}d_{50}) + f_d \mathbf{N}(\hat{\mathbf{T}}) \|\mathbf{D}_c + \mathbf{k}d_{50}\|] \quad (3.50)$$

$$\dot{\hat{\mathbf{m}}}/d_{50} = f_s[\mathbf{L}_m(\hat{\mathbf{T}}, \hat{\mathbf{m}}, \mathbf{D}_c, \mathbf{k}d_{50}) + f_d \mathbf{N}_m(\hat{\mathbf{m}}) \|\mathbf{D}_c + \mathbf{k}d_{50}\|] \quad (3.51)$$

Where $\hat{\mathbf{m}}$ is the couple stress vector, \mathbf{D}_c is the non-symmetric rate-of-deformation tensor, \mathbf{k} is the rate-of-curvature vector, d_{50} is mean grain diameter. The normalized granular stress tensor

$\hat{\mathbf{T}}$ and the normalized couple stress vector $\hat{\mathbf{m}}$ are defined by:

$$\hat{\mathbf{T}} = \frac{\mathbf{T}}{\text{tr}\mathbf{T}} \quad (3.52)$$

$$\hat{\mathbf{m}} = \frac{\mathbf{m}}{d_{50}\text{tr}\mathbf{T}} \quad (3.53)$$

Equations f_s and f_d are defined by:

$$f_s = \frac{h_s}{nh_i} \left(\frac{e_i}{e}\right)^\beta \frac{1+e_i}{e_i} \left(\frac{-\text{tr}\mathbf{T}}{h_s}\right)^{1-n} \quad (3.54)$$

$$f_d = \left(\frac{e-e_d}{e_c-e_d}\right)^\alpha \quad (3.55)$$

with

$$h_i = \frac{1}{c^2} + \frac{1}{3} - \left(\frac{e_{i0}-e_{d0}}{e_{c0}-e_{d0}}\right)^\alpha \frac{1}{c_1\sqrt{3}} \quad (3.56)$$

where h_s the granular hardness [25], e is the current void ratio, e_c the critical void ratio, e_d denotes the void ratio of maximum densification and e_i is the void ratio of maximum loosening, h_s denotes the granular hardness and α , β and n are constants. The values of e_i , e_d , e_c are assumed to decrease with the pressure level $-\text{tr}\mathbf{T}$ in the following way:

$$e_i = e_{i0}\exp[-(-\text{tr}\mathbf{T}/h_s)^n] \quad (3.57)$$

$$e_d = e_{d0}\exp[-(-\text{tr}\mathbf{T}/h_s)^n] \quad (3.58)$$

$$e_c = e_{c0}\exp[-(-\text{tr}\mathbf{T}/h_s)^n] \quad (3.59)$$

where e_{i0} , e_{d0} , e_{c0} are the values of e_i , e_d , e_c for the granular pressure equal to zero, respectively.

The tensor-valued functions \mathbf{L} , \mathbf{L}_m , \mathbf{N} , \mathbf{N}_m are given by:

$$\mathbf{L} = a_1^2 \mathbf{D}_c + \hat{\mathbf{T}}\text{tr}(\hat{\mathbf{T}}\mathbf{D}_c + \hat{\mathbf{m}}\mathbf{k}d_{50}), \mathbf{N} = a_1(\hat{\mathbf{T}} + \hat{\mathbf{T}}^*) \quad (3.60)$$

$$\mathbf{L}_m = a_1^2 \mathbf{k}d_{50} + \hat{\mathbf{m}}\text{tr}(\hat{\mathbf{T}}\mathbf{D}_c + \hat{\mathbf{m}}\mathbf{k}d_{50}), \mathbf{N}_m = a_m \hat{\mathbf{m}} \quad (3.61)$$

where

$$a_1^{-1} = c_1 + c_2 \sqrt{\text{tr}(\hat{\mathbf{T}}^{*2})} [1 + 3 \cos(\theta)], 3 \cos(\theta) = \frac{\sqrt{6}\text{tr}(\hat{\mathbf{T}}^{*3})}{[\text{tr}(\hat{\mathbf{T}}^{*2})]^{1.5}} \quad (3.62)$$

$$c_1 = \sqrt{\frac{3}{8}} \frac{(3 - \sin \phi_c)}{\sin \phi_c}, c_2 = \frac{3}{8} \frac{(3 + \sin \phi_c)}{\sin \phi_c} \quad (3.63)$$

where ϕ_c is the critical angle of internal friction from a triaxial compression test and θ is the Lode angle. The dimensionless constant a_m controls the influence of Cosserat quantities on

the material behavior. $\hat{\mathbf{T}}^*$ denotes the deviatoric part of $\hat{\mathbf{T}}$.

This model extends hypoplastic model with micropolar theory. Numerical simulations show that the behavior of granular material, including size dependent effects, can be very well predicted. However, this model is very complicated. The additional material parameter related to micropolar theory d_{50} and a_m cannot be easily determined. The couple-curvature equation (3.51) is obtained by simple analogy of stress-strain equation (3.50).

In this dissertation, a different approach is given, which links the hypoplasticity with micropolar theory with the help of complex tensor formulations. The mathematical details of this approach are shown in the next chapter.

Chapter 4

Complex micropolar hypoplastic model

4.1 Mathematical background

4.1.1 Tensor functions

Tensors are geometric objects that describe linear relations between vectors, scalars, and other tensors. Elementary examples of such relations include the dot product, the cross product, and linear maps. Vectors and scalars themselves are also tensors. A tensor can be represented as a multi-dimensional array of numerical values. The order (also degree or rank) of a tensor is the dimensionality of the array needed to represent it. A vector can be represented as a one-dimensional array and is a first-order tensor. Scalars are single numbers and are thus zeroth-order tensors.

The stresses inside a solid body or fluid are described by second order tensors. In detail, the tensor quantifying stress in a three-dimensional solid object has components that can be conveniently represented as a three times three array. The three faces of a cube-shaped infinitesimal volume segment of the solid are each subject to some given force. The force's vector components are also three in number. Thus, three times three, or nine components are required to describe the stress at this cube-shaped infinitesimal segment. Within the bounds of this solid is a whole mass of varying stress quantities, each requiring nine quantities to describe. Thus, a second order tensor is needed. Similarly stain, couple stress and curvature can also be described by a second order tensor with nine components.

Consider a tensor-valued function with n variable tensors:

$$\mathbf{T} = \mathbf{F}(\mathbf{G}_1, \mathbf{G}_2, \dots, \mathbf{G}_n) \quad (4.1)$$

For any orthogonal tensor \mathbf{Q} such that

$$\mathbf{Q}\mathbf{Q}^T = \mathbf{Q}^T\mathbf{Q} = \mathbf{I}, \det\mathbf{Q} = \pm 1 \quad (4.2)$$

if we have:

$$\mathbf{Q}\mathbf{T}\mathbf{Q}^T = \mathbf{F}(\mathbf{Q}\mathbf{G}_1\mathbf{Q}^T, \mathbf{Q}\mathbf{G}_2\mathbf{Q}^T, \dots, \mathbf{Q}\mathbf{G}_n\mathbf{Q}^T) \quad (4.3)$$

Then function \mathbf{F} is an isotropic tensor-valued tensor function.

Isotropic tensor-valued functions must be objective, which means they are independent of coordinate systems. If a tensor function holds in one coordinate system, it must hold for any other coordinate systems as well. Physic laws should be independent of coordinate systems, which means a physic law must be true for observers in different positions and orientations. Hence, physic laws often are written in the form of tensor functions.

4.1.2 Representation theorem

A theorem which defines a irreducible representation of a tensor-valued function on all variable tensors is the representation theorem. The representation formulas for tensor-valued isotropic functions of an arbitrary number of symmetric tensors and skew-symmetric tensors [45, 48, 49] are:

$$\mathbf{H}(\mathbf{A}_i, \mathbf{W}_p) = \sum_{r_1=1}^{s_1} \alpha_{r_1} \mathbf{H}_{r_1}(\mathbf{A}_i, \mathbf{W}_p) \quad (4.4)$$

$$\mathbf{Z}(\mathbf{A}_i, \mathbf{W}_p) = \sum_{r_2=1}^{s_2} \alpha_{r_2} \mathbf{Z}_{r_2}(\mathbf{A}_i, \mathbf{W}_p) \quad (4.5)$$

\mathbf{H} is the symmetric part of the tensor-valued function, and \mathbf{Z} is the skew-symmetric part of the tensor-valued function. \mathbf{A}_i are symmetric tensors and \mathbf{W}_p are skew-symmetric tensors. α_{r_1} or α_{r_2} are scalar-valued isotropic functions of \mathbf{A}_i and \mathbf{W}_p , which are given by:

$$\begin{aligned} \alpha_r = \alpha_r(\text{tr}\mathbf{A}_i, \text{tr}\mathbf{A}_i^3, \text{tr}\mathbf{A}_i^3, \text{tr}\mathbf{A}_i\mathbf{A}_j, \text{tr}\mathbf{A}_i^2\mathbf{A}_j, \text{tr}\mathbf{A}_i\mathbf{A}_j^2, \text{tr}\mathbf{A}_i^2\mathbf{A}_j^2, \text{tr}\mathbf{A}_i\mathbf{A}_j\mathbf{A}_k, \text{tr}\mathbf{W}_p^2, \text{tr}\mathbf{W}_p\mathbf{W}_q, \\ \text{tr}\mathbf{W}_p\mathbf{W}_q\mathbf{W}_r, \text{tr}\mathbf{A}_i\mathbf{W}_p^2, \text{tr}\mathbf{A}_i^2\mathbf{W}_p^2, \text{tr}\mathbf{A}_i^2\mathbf{W}_p^2\mathbf{A}_i\mathbf{W}_p, \text{tr}\mathbf{A}_i\mathbf{W}_p\mathbf{W}_q, \text{tr}\mathbf{A}_i\mathbf{W}_p\mathbf{W}_q^2, \\ \text{tr}\mathbf{A}_i\mathbf{W}_p^2\mathbf{W}_q, \text{tr}\mathbf{A}_i\mathbf{A}_j\mathbf{W}_p, \text{tr}\mathbf{A}_i\mathbf{A}_j\mathbf{W}_p^2, \text{tr}\mathbf{A}_i\mathbf{W}_p^2\mathbf{A}_j\mathbf{W}_p, \text{tr}\mathbf{A}_i\mathbf{A}_j^2\mathbf{W}_p, \text{tr}\mathbf{A}_i^2\mathbf{A}_j\mathbf{W}_p) \end{aligned}$$

where $i, j, k = 1 \dots N; i < j < k$, where $p, q, r = 1 \dots M; p < q < r$.

\mathbf{H}_{r_1} are given by:

$$\begin{aligned} \mathbf{A}_i, \mathbf{A}_i^2, \mathbf{A}_i\mathbf{A}_j + \mathbf{A}_j\mathbf{A}_i, \mathbf{A}_i^2\mathbf{A}_j + \mathbf{A}_j\mathbf{A}_i^2, \mathbf{A}_i\mathbf{A}_j^2 + \mathbf{A}_j^2\mathbf{A}_i, \mathbf{W}_p^2, \mathbf{W}_p\mathbf{W}_q + \mathbf{W}_q\mathbf{W}_p, \\ \mathbf{W}_p\mathbf{W}_q^2 - \mathbf{W}_q^2\mathbf{W}_p, \mathbf{W}_p^2\mathbf{W}_q - \mathbf{W}_q\mathbf{W}_p^2, \mathbf{A}_i\mathbf{W}_p - \mathbf{W}_p\mathbf{A}_i, \mathbf{W}_p\mathbf{A}_i\mathbf{W}_p, \\ \mathbf{A}_i^2\mathbf{W}_p - \mathbf{W}_p\mathbf{A}_i^2, \mathbf{W}_p\mathbf{A}_1\mathbf{W}_p^2 - \mathbf{W}_p^2\mathbf{A}_i\mathbf{W}_p \end{aligned}$$

where $i, j, k = 1 \dots N; i < j < k$, where $p, q, r = 1 \dots M; p < q < r$.

\mathbf{Z}_{r_2} are given by:

$$\begin{aligned} & \mathbf{W}_p, \mathbf{W}_p \mathbf{W}_q - \mathbf{W}_q \mathbf{W}_p, \mathbf{A}_i \mathbf{A}_j - \mathbf{A}_j \mathbf{A}_i, \mathbf{A}_i^2 \mathbf{A}_j - \mathbf{A}_j \mathbf{A}_i^2, \mathbf{A}_i \mathbf{A}_j^2 - \mathbf{A}_j^2 \mathbf{A}_i, \mathbf{A}_i \mathbf{A}_j \mathbf{A}_i^2 - \mathbf{A}_i^2 \mathbf{A}_j \mathbf{A}_i, \\ & \mathbf{A}_j \mathbf{A}_i \mathbf{A}_j^2 - \mathbf{A}_j^2 \mathbf{A}_i \mathbf{A}_j, \mathbf{A}_i \mathbf{A}_j \mathbf{A}_k + \mathbf{A}_j \mathbf{A}_k \mathbf{A}_i + \mathbf{A}_k \mathbf{A}_i \mathbf{A}_j - \mathbf{A}_j \mathbf{A}_i \mathbf{A}_k - \mathbf{A}_i \mathbf{A}_k \mathbf{A}_j - \mathbf{A}_k \mathbf{A}_j \mathbf{A}_i, \\ & \mathbf{A}_i \mathbf{W}_p + \mathbf{W}_p \mathbf{A}_i, \mathbf{A}_i \mathbf{W}_p^2 - \mathbf{W}_p^2 \mathbf{A}_i \end{aligned}$$

where $i, j, k = 1 \dots N; i < j < k$, where $p, q, r = 1 \dots M; p < q < r$.

The representation theorem defines irreducible representations of tensor functions. For a simple problem, such as linear elastic constitutive problem, the tensor-valued equation can be directly obtained from the corresponding representation. However, for problems such as hypoplasticity or micropolar model, the representation formulas is too complicated to be used directly. Hence, some mathematical derivations and assumptions need to be made, which will be shown in the following sections.

4.1.3 Complex tensor

Analog to complex numbers, tensors can also be put into a complex form $\mathbf{A} + i\mathbf{B}$, where \mathbf{A} and \mathbf{B} are tensors and i is called the imaginary unit, where $i^2 = -1$. In this expression, \mathbf{A} is called the real part and \mathbf{B} is called the imaginary part of the complex tensor. If both \mathbf{A} and \mathbf{B} are n th order tensors, $\mathbf{A} + i\mathbf{B}$ is a n th order complex tensor. In this way the complex tensors contain the ordinary real tensors while extending them in order to solve problems which have imaginary parts.

The operation rules of complex tensors are shown in the paper of Xiao [56]. For any complex tensors $\mathbf{S}' = \mathbf{U} + i\mathbf{V}$, $\mathbf{T}' = \mathbf{X} + i\mathbf{Y}$ and complex number $\lambda = \alpha + i\beta$, we have:

$$\lambda \mathbf{S}' = (\alpha \mathbf{U} - \beta \mathbf{V}) + i(\alpha \mathbf{V} + \beta \mathbf{U}) \quad (4.6)$$

$$\mathbf{S}' + \mathbf{T}' = (\mathbf{U} + \mathbf{X}) + i(\mathbf{V} + \mathbf{Y}) \quad (4.7)$$

$$\mathbf{S}' : \mathbf{T}' = (\mathbf{U} : \mathbf{X} + \mathbf{V} : \mathbf{Y}) + i(\mathbf{V} : \mathbf{X} - \mathbf{U} : \mathbf{Y}) \quad (4.8)$$

$$\mathbf{S}' \otimes \mathbf{T}' = (\mathbf{U} \otimes \mathbf{X} - \mathbf{V} \otimes \mathbf{Y}) + i(\mathbf{U} \otimes \mathbf{Y} + \mathbf{V} \otimes \mathbf{X}) \quad (4.9)$$

where $:$ is inner product and \otimes is tensor product.

Complex tensors are widely used in theoretical physics and continuum mechanics [24, 56]. Goddard showed an idea to implement micropolar theory into hypoplastic model by using complex formulations [24]. However, he did not get any constitutive equations out of this formulation.

4.2 Complex micropolar hypoplastic model

In this section, micropolar theory and hypoplasticity are combined with the help of complex tensor formulations. Two equations are obtained by derivations and separating the real and imaginary part. These two equations define the new micropolar hypoplastic model. By assuming the the symmetry of each tensor, the model is greatly simplified. The new model is discussed and compared to the existing micropolar hypoplastic model.

4.2.1 Formulation

Starting from the updated hypoplastic equation (3.27), which has the following form:

$$\dot{\mathbf{T}} = C_1 \text{tr}(\mathbf{T})\mathbf{D} + C_2 \text{tr}(\mathbf{D})\mathbf{T} + C_3 \frac{\text{tr}\mathbf{T}\mathbf{D}}{\text{tr}\mathbf{T}}\mathbf{T} + C_4 \|\mathbf{D}\|(\mathbf{T} + \mathbf{T}^*) \quad (4.10)$$

The stress rate tensor $\dot{\mathbf{T}}$, stress tensor \mathbf{T} and strain rate tensor \mathbf{D} can be extended with micropolar terms. Hence, the following complex tensors are formulated:

$$\dot{\mathbf{T}}' = \dot{\mathbf{T}} + i \frac{\dot{\mathbf{M}}}{l} \quad (4.11)$$

$$\mathbf{T}' = \mathbf{T} + i \frac{\mathbf{M}}{l} \quad (4.12)$$

$$\mathbf{D}' = \mathbf{D} + i l \mathbf{K} \quad (4.13)$$

A characteristic length l is added to balance the dimensions of the real and imaginary part of the complex formulation. \mathbf{M}/l has the same dimension as \mathbf{T} and $l\mathbf{K}$ has the same dimension as \mathbf{D} . l has an unit of length, unlike d_{50} used in equations (3.50) and (3.51), l does not have to be the mean particle diameter.

Substituting these complex tensors into equation (3.27) gives:

$$\dot{\mathbf{T}}' = C_1 \text{tr}(\mathbf{T}')\mathbf{D}' + C_2 \text{tr}(\mathbf{D}')\mathbf{T}' + C_3 \frac{\text{tr}\mathbf{T}'\mathbf{D}'}{\text{tr}\mathbf{T}'}\mathbf{T}' + C_4 \|\mathbf{D}'\|(\mathbf{T}' + \mathbf{T}'^*) \quad (4.14)$$

According to the operation rules 4.6-4.9, each term of equation (4.14) can be expanded. The real part and imaginary part of each term can be calculated and separated as shown in the following:

The first term:

$$\begin{aligned} C_1 \text{tr}(\mathbf{T}')\mathbf{D}' &= C_1 \text{tr}\left(\mathbf{T} + i \frac{\mathbf{M}}{l}\right)(\mathbf{D} + i l \mathbf{K}) = C_1 \left(\text{tr}(\mathbf{T}) + i \frac{\text{tr}(\mathbf{M})}{l}\right)(\mathbf{D} + i l \mathbf{K}) \quad (4.15) \\ &= C_1 (\text{tr}(\mathbf{T})\mathbf{D} - \text{tr}(\mathbf{M})\mathbf{K}) + i C_1 \left(l \text{tr}(\mathbf{T})\mathbf{K} + \frac{\text{tr}(\mathbf{M})}{l} \mathbf{D}\right) \end{aligned}$$

The second term:

$$\begin{aligned}
C_2 \text{tr}(\mathbf{D}') \mathbf{T}' &= C_2 \text{tr}(\mathbf{D} + i l \mathbf{K})(\mathbf{T} + i \frac{\mathbf{M}}{l}) = C_2 (\text{tr} \mathbf{D} + i l \text{tr} \mathbf{K})(\mathbf{T} + i \frac{\mathbf{M}}{l}) \quad (4.16) \\
&= C_2 (\text{tr}(\mathbf{D}) \mathbf{T} - \text{tr}(\mathbf{K}) \mathbf{M}) + i C_2 (\frac{\text{tr}(\mathbf{D})}{l} \mathbf{M} + l \text{tr}(\mathbf{K}) \mathbf{T})
\end{aligned}$$

The third term:

$$\begin{aligned}
C_3 \frac{\text{tr} \mathbf{T}' \mathbf{D}'}{\text{tr} \mathbf{T}'} \mathbf{T}' &= C_3 \frac{\text{tr}(\mathbf{T} + i \frac{\mathbf{M}}{l})(\mathbf{D} + i l \mathbf{K})}{\text{tr}(\mathbf{T} + i \frac{\mathbf{M}}{l})} (\mathbf{T} + i \frac{\mathbf{M}}{l}) \quad (4.17) \\
&= C_3 \frac{\text{tr}(\mathbf{T} \mathbf{D} - \mathbf{M} \mathbf{K}) + i \text{tr}(\mathbf{T} \mathbf{K} l + \frac{\mathbf{D} \mathbf{M}}{l})}{\text{tr} \mathbf{T} + i \frac{\text{tr} \mathbf{M}}{l}} (\mathbf{T} + i \frac{\mathbf{M}}{l}) \\
&= C_3 \frac{[\text{tr}(\mathbf{T} \mathbf{D} - \mathbf{M} \mathbf{K}) + i \text{tr}(\mathbf{T} \mathbf{K} l + \frac{\mathbf{D} \mathbf{M}}{l})] (\text{tr} \mathbf{T} - i \frac{\text{tr} \mathbf{M}}{l})}{(\text{tr} \mathbf{T})^2 + \frac{(\text{tr} \mathbf{M})^2}{l^2}} (\mathbf{T} + i \frac{\mathbf{M}}{l}) \\
&= C_3 \left\{ \frac{\text{tr} \mathbf{T} [\text{tr}(\mathbf{T} \mathbf{D}) - \text{tr}(\mathbf{M} \mathbf{K})] + \frac{\text{tr} \mathbf{M}}{l} [\frac{\text{tr}(\mathbf{M} \mathbf{D})}{l} + l \text{tr}(\mathbf{T} \mathbf{K})]}{(\text{tr} \mathbf{T})^2 + \frac{(\text{tr} \mathbf{M})^2}{l^2}} \mathbf{T} \right. \\
&\quad \left. - \frac{\frac{\text{tr} \mathbf{M}}{l} [\text{tr}(\mathbf{M} \mathbf{K}) - \text{tr}(\mathbf{T} \mathbf{D})] + \text{tr} \mathbf{T} [\frac{\text{tr}(\mathbf{M} \mathbf{D})}{l} - l \text{tr}(\mathbf{T} \mathbf{K})]}{[(\text{tr} \mathbf{T})^2 + \frac{(\text{tr} \mathbf{M})^2}{l^2}] l} \mathbf{M} \right\} \\
&\quad + i C_3 \left\{ \frac{\text{tr} \mathbf{T} [\text{tr}(\mathbf{T} \mathbf{D}) - \text{tr}(\mathbf{M} \mathbf{K})] + \frac{\text{tr} \mathbf{M}}{l} [\frac{\text{tr}(\mathbf{M} \mathbf{D})}{l} + l \text{tr}(\mathbf{T} \mathbf{K})]}{[(\text{tr} \mathbf{T})^2 + \frac{(\text{tr} \mathbf{M})^2}{l^2}] l} \mathbf{M} \right. \\
&\quad \left. + \frac{\frac{\text{tr} \mathbf{M}}{l} [\text{tr}(\mathbf{M} \mathbf{K}) - \text{tr}(\mathbf{T} \mathbf{D})] + \text{tr} \mathbf{T} [\frac{\text{tr}(\mathbf{M} \mathbf{D})}{l} - l \text{tr}(\mathbf{T} \mathbf{K})]}{(\text{tr} \mathbf{T})^2 + \frac{(\text{tr} \mathbf{M})^2}{l^2}} \mathbf{T} \right\}
\end{aligned}$$

The fourth term:

$$\begin{aligned}
C_4 \|\mathbf{D}'\| (\mathbf{T}' + \mathbf{T}'^*) &= C_4 \sqrt{\|\mathbf{D}\|^2 + l^2 \|\mathbf{K}\|^2} [(\mathbf{T} + i \frac{\mathbf{M}}{l}) + (\mathbf{T}^* + i \frac{\mathbf{M}^*}{l})] \quad (4.18) \\
&= C_4 \sqrt{\|\mathbf{D}\|^2 + l^2 \|\mathbf{K}\|^2} [(\mathbf{T} + \mathbf{T}^*) + i \frac{\mathbf{M} + \mathbf{M}^*}{l}] \\
&= C_4 \sqrt{\|\mathbf{D}\|^2 + l^2 \|\mathbf{K}\|^2} (\mathbf{T} + \mathbf{T}^*) + i C_4 \sqrt{\|\mathbf{D}\|^2 + l^2 \|\mathbf{K}\|^2} \frac{\mathbf{M} + \mathbf{M}^*}{l}
\end{aligned}$$

Since $\mathring{\mathbf{T}}' = \mathring{\mathbf{T}} + i\mathring{\mathbf{M}}/l$, the real part and imaginary part of equation (4.14) can be separated into the following two equations:

$$\begin{aligned} \mathring{\mathbf{T}} = & C_1(\text{tr}(\mathbf{T})\mathbf{D} - \text{tr}(\mathbf{M})\mathbf{K}) + C_2(\text{tr}(\mathbf{D})\mathbf{T} - \text{tr}(\mathbf{K})\mathbf{M}) \\ & + C_3\left\{\frac{\text{tr}\mathbf{T}[\text{tr}(\mathbf{T}\mathbf{D}) - \text{tr}(\mathbf{M}\mathbf{K})] + \frac{\text{tr}\mathbf{M}}{l}\left[\frac{\text{tr}(\mathbf{M}\mathbf{D})}{l} + l\text{tr}(\mathbf{T}\mathbf{K})\right]}{(\text{tr}\mathbf{T})^2 + \frac{(\text{tr}\mathbf{M})^2}{l^2}}\mathbf{T}\right. \\ & \left. - \frac{\frac{\text{tr}\mathbf{M}}{l}[\text{tr}(\mathbf{M}\mathbf{K}) - \text{tr}(\mathbf{T}\mathbf{D})] + \text{tr}\mathbf{T}\left[\frac{\text{tr}(\mathbf{M}\mathbf{D})}{l} - l\text{tr}(\mathbf{T}\mathbf{K})\right]}{[(\text{tr}\mathbf{T})^2 + \frac{(\text{tr}\mathbf{M})^2}{l^2}]l}\mathbf{M}\right\} \\ & + C_4\sqrt{\|\mathbf{D}\|^2 + l^2\|\mathbf{K}\|^2}(\mathbf{T} + \mathbf{T}^*) \end{aligned} \quad (4.19)$$

$$\begin{aligned} \frac{\mathring{\mathbf{M}}}{l} = & C_1(l\text{tr}(\mathbf{T})\mathbf{K} + \frac{\text{tr}(\mathbf{M})}{l}\mathbf{D}) + C_2\left(\frac{\text{tr}(\mathbf{D})}{l}\mathbf{M} + l\text{tr}(\mathbf{K})\mathbf{T}\right) \\ & + C_3\left\{\frac{\text{tr}\mathbf{T}[\text{tr}(\mathbf{T}\mathbf{D}) - \text{tr}(\mathbf{M}\mathbf{K})] + \frac{\text{tr}\mathbf{M}}{l}\left[\frac{\text{tr}(\mathbf{M}\mathbf{D})}{l} + l\text{tr}(\mathbf{T}\mathbf{K})\right]}{[(\text{tr}\mathbf{T})^2 + \frac{(\text{tr}\mathbf{M})^2}{l^2}]l}\mathbf{M}\right. \\ & \left. + \frac{\frac{\text{tr}\mathbf{M}}{l}[\text{tr}(\mathbf{M}\mathbf{K}) - \text{tr}(\mathbf{T}\mathbf{D})] + \text{tr}\mathbf{T}\left[\frac{\text{tr}(\mathbf{M}\mathbf{D})}{l} - l\text{tr}(\mathbf{T}\mathbf{K})\right]}{(\text{tr}\mathbf{T})^2 + \frac{(\text{tr}\mathbf{M})^2}{l^2}}\mathbf{T}\right\} \\ & + C_4\sqrt{\|\mathbf{D}\|^2 + l^2\|\mathbf{K}\|^2}\frac{\mathbf{M} + \mathbf{M}^*}{l} \end{aligned} \quad (4.20)$$

By multiplying l on both side, equation (4.20) becomes:

$$\begin{aligned} \mathring{\mathbf{M}} = & C_1(l^2\text{tr}(\mathbf{T})\mathbf{K} + \text{tr}(\mathbf{M})\mathbf{D}) + C_2(\text{tr}(\mathbf{D})\mathbf{M} + l^2\text{tr}(\mathbf{K})\mathbf{T}) \\ & + C_3\left\{\frac{\text{tr}\mathbf{T}[\text{tr}(\mathbf{T}\mathbf{D}) - \text{tr}(\mathbf{M}\mathbf{K})] + \frac{\text{tr}\mathbf{M}}{l}\left[\frac{\text{tr}(\mathbf{M}\mathbf{D})}{l} + l\text{tr}(\mathbf{T}\mathbf{K})\right]}{(\text{tr}\mathbf{T})^2 + \frac{(\text{tr}\mathbf{M})^2}{l^2}}\mathbf{M}\right. \\ & \left. + \frac{\text{tr}\mathbf{M}[\text{tr}(\mathbf{M}\mathbf{K}) - \text{tr}(\mathbf{T}\mathbf{D})] + \text{tr}\mathbf{T}[\text{tr}(\mathbf{M}\mathbf{D}) - l^2\text{tr}(\mathbf{T}\mathbf{K})]}{(\text{tr}\mathbf{T})^2 + \frac{(\text{tr}\mathbf{M})^2}{l^2}}\mathbf{T}\right\} \\ & + C_4\sqrt{\|\mathbf{D}\|^2 + l^2\|\mathbf{K}\|^2}(\mathbf{M} + \mathbf{M}^*) \end{aligned} \quad (4.21)$$

4.2.2 Assumptions and simplification

Equations 4.19 and 4.21 define the micropolar hypoplastic constitutive model obtained by complex formulations. However, they are too complicated for practical use. Without any assumptions, all of the tensors $\mathring{\mathbf{T}}$, $\mathring{\mathbf{M}}$, \mathbf{T} , \mathbf{D} , \mathbf{M} and \mathbf{K} have nine independent components.

However, by assuming the symmetry or skew-symmetry of the tensors, the constitutive equations can be greatly simplified. Several assumptions are shown in the following.

In micropolar continuum, the stress tensor and strain rate tensor are normally asymmetric. However, the skew-symmetric part of stress and strain rate tensor is linked to couple stress and curvature tensor by balance equations.

$$\mathbf{M}_{j,i,j} + \varepsilon_{ijk} \mathbf{T}_{jk} = 0 \quad (4.22)$$

Only the symmetric part of stress and strain rate tensor are independent and need to be determined by constitutive equations. Hence, we can use the symmetric stress and strain rate tensor in the constitutive equation, which means in equations (4.19) and (4.21), symmetric stress (\mathbf{T}) and strain rate (\mathbf{D}) tensors can be used.

Regarding the symmetry of couple stress and curvature tensors, different assumptions have been used by different researchers. Yang [57] studied elastic couple stress theory and concluded that the couple stress and curvature tensors are symmetric. His constitutive model has been used by Akgöz[1, 2]. If this assumption is true, the equations (4.19) and (4.21) cannot be simplified since none of the components in the equations equals to zero.

In another hand, Hadjefandiari [26, 26] assumed that the couple stress and curvature tensor are skew-symmetric. In some previous micropolar hypoplastic models [46], vectors, which are equivalent to skew-symmetric tensors, are used to describe couple stress and curvature rate. Hence, in these models, couple stress (\mathbf{M}) and curvature rate (\mathbf{K}) tensor are assumed to be skew-symmetric.

With the assumptions of skew-symmetry of couple stress and curvature, we have:

$$\text{tr}(\mathbf{M}) = 0 \quad (4.23)$$

$$\text{tr}(\mathbf{K}) = 0 \quad (4.24)$$

$$\text{tr}(\mathbf{MD}) = 0 \quad (4.25)$$

$$\text{tr}(\mathbf{TK}) = 0 \quad (4.26)$$

$$\mathbf{M}^* = \mathbf{M} \quad (4.27)$$

Hence, equations (4.19) and (4.21) become

$$\begin{aligned} \dot{\mathbf{T}} = & C_1 \text{tr}(\mathbf{T})\mathbf{D} + C_2 \text{tr}(\mathbf{D})\mathbf{T} + C_3 \frac{\text{tr}\mathbf{TD} - \text{tr}\mathbf{MK}}{\text{tr}\mathbf{T}} \mathbf{T} \\ & + C_4 \sqrt{|\mathbf{D}|^2 + l^2 |\mathbf{K}|^2} (\mathbf{T} + \mathbf{T}^*) \end{aligned} \quad (4.28)$$

$$\begin{aligned} \dot{\mathbf{M}} = & C_1 l^2 \text{tr}(\mathbf{T})\mathbf{K} + C_2 \text{tr}(\mathbf{D})\mathbf{M} + C_3 \frac{\text{tr}\mathbf{TD} - \text{tr}\mathbf{MK}}{\text{tr}\mathbf{T}} \mathbf{M} \\ & + 2C_4 \sqrt{|\mathbf{D}|^2 + l^2 |\mathbf{K}|^2} \mathbf{M} \end{aligned} \quad (4.29)$$

By using symmetric stress and strain rate tensors, and assuming the skew-symmetry of the couple stress and strain rate tensors, the constitutive model is greatly simplified. This model

is implemented into a finite-element code. The simulation results are shown in the following chapters.

4.2.3 Discussion of the new model

The new micropolar hypoplastic constitutive model are developed by complex tensor formulations. With the assumptions of symmetric stress, strain rate tensors and skew-symmetric couple stress, curvature rate tensors, the model can be simplified to equations (4.28) and (4.29). It is similar to the existing micropolar hypoplastic model (equations (3.50) and (3.51)), yet there are several differences.

- Equations 3.50 and 3.51 are based on the reduced form of hypoplastic model with only has three material parameters which restricts the adaptability. Equations 4.28 and 4.29 have additional terms $\text{tr}(\mathbf{D})\mathbf{T}$ and $\text{tr}(\mathbf{D})\mathbf{M}$, so that the number of parameters retains four. Hence, more material parameters such as the initial Poisson ratio can be included.
- Equations 4.28 and 4.29 have only one additional micropolar material parameter, which is the internal length l . This length can be determined from the width of the shear band, detailed discussions can be found in section 6.2. Equations 3.50 and 3.51 use both a_m and d_{50} , where d_{50} is the internal length assumed to be the mean particle diameter. The meaning of a_m is not clearly defined. The shear band width depends on both a_m and d_{50} .
- Unlike equations (3.50) and (3.51), The new model do not have dependence on pore ratio. However, it can be added by introducing a factor on the nonlinear term. For example:

$$\begin{aligned} \mathring{\mathbf{T}} = & C_1 \text{tr}(\mathbf{T})\mathbf{D} + C_2 \text{tr}(\mathbf{D})\mathbf{T} + C_3 \frac{\text{tr}\mathbf{T}\mathbf{D} - \text{tr}\mathbf{M}\mathbf{K}}{\text{tr}\mathbf{T}}\mathbf{T} \\ & + C_4 \left[(1-a) \frac{e - e_{min}}{e_c - e_{min}} + a \right] \sqrt{|\mathbf{D}|^2 + l^2 |\mathbf{K}|^2} (\mathbf{T} + \mathbf{T}^*) \end{aligned} \quad (4.30)$$

$$\begin{aligned} \mathring{\mathbf{M}} = & C_1 l^2 \text{tr}(\mathbf{T})\mathbf{K} + C_2 \text{tr}(\mathbf{D})\mathbf{M} + C_3 \frac{\text{tr}\mathbf{T}\mathbf{D} - \text{tr}\mathbf{M}\mathbf{K}}{\text{tr}\mathbf{T}}\mathbf{M} \\ & + 2C_4 \left[(1-a) \frac{e - e_{min}}{e_c - e_{min}} + a \right] \sqrt{|\mathbf{D}|^2 + l^2 |\mathbf{K}|^2} \mathbf{M} \end{aligned} \quad (4.31)$$

where e is the current pore ratio, e_c is the critical pore ratio, e_{min} is the minimum pore ratio and a is a constant less than 1. The evolution of the pore ratio is determined by :

$$\dot{e} = (1 + e)\text{tr}\mathbf{D} \quad (4.32)$$

The additional factor becomes 1 for $e = e_c$ and becomes a for $e = e_{min}$.

4.3 Expansion of complex formulation method

The method of using complex formulations to obtain micropolar constitutive equations is not limited to the hypoplastic model presented above. Principally, for any classical constitutive equations in tensor form, we can use complex formulation method to generate micropolar constitutive equations. Some examples are shown in the following.

For a linear elastic constitutive equation with the following form:

$$\mathbf{T}_{ij} = \lambda \mathbf{E}_{kk} \delta_{ij} + 2\mu \mathbf{E}_{(i,j)} + 2\mu_c \mathbf{E}_{\{i,j\}} \quad (4.33)$$

By assuming general stress and strain tensors with the following complex form:

$$\mathbf{T}' = \mathbf{T} + i \frac{\mathbf{M}}{l}, \mathbf{E}' = \mathbf{E} + il\mathbf{C} \quad (4.34)$$

we have:

$$\begin{aligned} \mathbf{T}'_{ij} &= \mathbf{T} + i \frac{\mathbf{M}}{l} = \lambda \mathbf{E}'_{kk} \delta_{ij} + 2\mu \mathbf{E}'_{(i,j)} + 2\mu_c \mathbf{E}'_{\{i,j\}} \\ &= (\lambda \mathbf{E}_{kk} \delta_{ij} + 2\mu \mathbf{E}_{(i,j)} + 2\mu_c \mathbf{E}_{\{i,j\}}) + i(l\lambda \mathbf{C}_{kk} \delta_{ij} + 2l\mu \mathbf{C}_{(i,j)} + 2l\mu_c \mathbf{C}_{\{i,j\}}) \end{aligned} \quad (4.35)$$

Hence:

$$\mathbf{T}_{ij} = \lambda \mathbf{E}_{kk} \delta_{ij} + 2\mu \mathbf{E}_{(i,j)} + 2\mu_c \mathbf{E}_{\{i,j\}} \quad (4.36)$$

$$\mathbf{M}_{ij} = l^2 \lambda \mathbf{C}_{kk} \delta_{ij} + 2l^2 \mu \mathbf{C}_{(i,j)} + 2l^2 \mu_c \mathbf{C}_{\{i,j\}} \quad (4.37)$$

These equations are identical to the micropolar elastic constitutive equations (3.44) and (3.45).

For the original hypoplastic model (equation (3.24)), which has the following form:

$$\mathring{\mathbf{T}} = C_1 \text{tr}(\mathbf{T}) \mathbf{D} + C_2 \frac{\text{tr} \mathbf{T} \mathbf{D}}{\text{tr} \mathbf{T}} \mathbf{T} + C_3 \frac{\mathbf{T}^2}{\text{tr} \mathbf{T}} \|\mathbf{D}\| + C_4 \frac{\mathbf{T}^{*2}}{\text{tr} \mathbf{T}} \|\mathbf{D}\| \quad (4.38)$$

Using the same complex formulations and the assumptions of equation (4.28) and (4.29). A micropolar constitutive model can be obtained:

$$\begin{aligned} \mathring{\mathbf{T}} &= C_1 \text{tr}(\mathbf{T}) \mathbf{D} + C_2 \frac{\text{tr} \mathbf{T} \mathbf{D} - \text{tr} \mathbf{M} \mathbf{K}}{\text{tr} \mathbf{T}} \mathbf{T} \\ &\quad + (C_3 \frac{\mathbf{T}^2 - \mathbf{M}^2/l^2}{\text{tr} \mathbf{T}} + C_4 \frac{\mathbf{T}^{*2} - \mathbf{M}^2/l^2}{\text{tr} \mathbf{T}}) \sqrt{\|\mathbf{D}\|^2 + l^2 \|\mathbf{K}\|^2} \end{aligned} \quad (4.39)$$

$$\begin{aligned} \mathring{\mathbf{M}} &= C_1 l^2 \text{tr}(\mathbf{T}) \mathbf{K} + C_2 \frac{\text{tr} \mathbf{T} \mathbf{D} - \text{tr} \mathbf{M} \mathbf{K}}{\text{tr} \mathbf{T}} \mathbf{M} \\ &\quad + (C_3 \frac{\mathbf{T} \mathbf{M} + \mathbf{M} \mathbf{T}}{\text{tr} \mathbf{T}} + C_4 \frac{\mathbf{T}^* \mathbf{M} + \mathbf{M} \mathbf{T}^*}{\text{tr} \mathbf{T}}) \sqrt{\|\mathbf{D}\|^2 + l^2 \|\mathbf{K}\|^2} \end{aligned} \quad (4.40)$$

Detailed derivation processes are not shown here. Note that \mathbf{M}^2/l^2 is symmetric and $\mathbf{T} \mathbf{M} + \mathbf{M} \mathbf{T}$, $\mathbf{T}^* \mathbf{M} + \mathbf{M} \mathbf{T}^*$ are skew-symmetric. Hence, the stress rate tensor $\mathring{\mathbf{T}}$ is always symmetric and the couple stress rate tensor $\mathring{\mathbf{M}}$ is always skew-symmetric.

Chapter 5

Finite element implementation

5.1 Finite element method

The finite element method (FEM) is a numerical method for solving partial differential equations (PDE) by discretization and integration in time and space. It is a method of approximation to continuum problems such that the continuum is divided into a finite number of parts (elements), the behavior of which is specified by a finite number of parameters, and the solution of the complete system as an assembly of its elements. Although many problems cannot be solved precisely, by using finite element method, approximate solutions can be obtained. However, if proper element type and size are used, the FEM solutions have a high accuracy. Also, FEM can be applied for problems with complex geometries.

The FEM is one of the most frequently used theory in researching and engineering, due to its low restrictions on the applicability. It can be used to solve problems including static/dynamic structural analysis, heat transfer, fluid problems, acoustic and electromagnetic problems.

The basic FEM calculation procedures are discretization, element analysis, system analysis and solution. The general schema of a FEM software include preprocessor, solver and post-processor, as shown in Figure 5.1.

The most commonly used FEM softwares include commercial softwares Abaqus, ADINA, MSC, Ansys and many open source FEM codes, such as Dimer, CalculiX, Code_Aster, Impact and OOFEM. In this dissertation, Abaqus is used to implement the hypoplastic micropolar constitutive model.

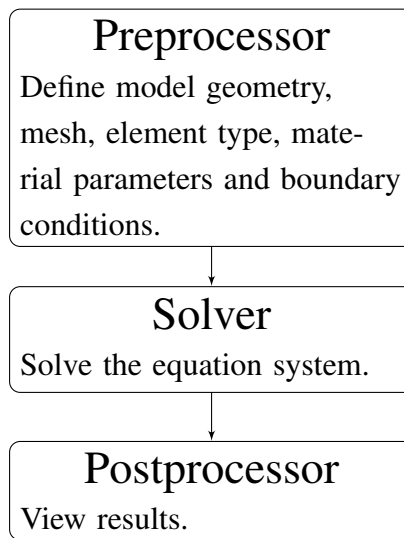


Figure 5.1: General schema of finite element method

5.2 Background of Abaqus

Abaqus is a commercial software package of finite element method, which can be used to solve a variety of linear or nonlinear problems. There are several analysis programs in Abaqus including Abaqus/Standard, Abaqus/Explicit and Abaqus/CFD, which can be used to solve implicit, explicit and fluid dynamic problems. Pre-processing and post-processing tools are also available in the software package of Abaqus.

The element library of Abaqus includes many types of elements for different applications. However, sometimes these elements are not enough for special purposes. Hence, user-defined elements have to be used. An user defined element:

- can be finite elements in the usual sense of representing a geometric part of the model;
- can be feedback links, supplying forces at some points as functions of values of displacement, velocity, etc. at other points in the model;
- can be used to solve equations in terms of nonstandard degrees of freedom;
- can be linear or nonlinear; and
- can access selected materials from the Abaqus material library.

For micropolar continuum model, in addition to the translational degrees of freedom, the rotational degrees of freedom must be included. Rotational degrees of freedom are nonstandard degrees of freedom. Hence, user defined element is used here to implement the micropolar hypoplastic model.

5.3 Implementation

Based on the virtual work principle for micropolar continuum (equation (3.14)), the weak form of a micropolar boundary value problem can be given by:

$$\int_{\Omega} (\text{div} \mathbf{T} + \rho \mathbf{b} - \rho \frac{D\mathbf{v}}{Dt}) \delta \mathbf{u} dV + \int_{\Omega} (\text{div} \mathbf{M} + \rho \mathbf{c} + \varepsilon \mathbf{T} - \rho \frac{D(\mathbf{J}\boldsymbol{\omega})}{Dt}) \delta \mathbf{r} dV \quad (5.1)$$

$$- \int_{\partial\Omega} (\mathbf{T} \cdot \mathbf{n} - \mathbf{t}) \delta \mathbf{u} dA - \int_{\partial\Omega} (\mathbf{M} \cdot \mathbf{n} - \mathbf{m}) \delta \mathbf{r} dA = 0$$

In our case, the accelerations, body forces and body couples are neglected. Hence, the weak formulation can be simplified to:

$$\int_{\Omega} \text{div} \mathbf{T} \delta \mathbf{u} dV + \int_{\Omega} (\text{div} \mathbf{M} + \varepsilon \mathbf{T}) \delta \mathbf{r} dV - \int_{\partial\Omega} (\mathbf{T} \cdot \mathbf{n} - \mathbf{t}) \delta \mathbf{u} dA \quad (5.2)$$

$$- \int_{\partial\Omega} (\mathbf{M} \cdot \mathbf{n} - \mathbf{m}) \delta \mathbf{r} dA = 0$$

This equation is solved by discretization and approximation with finite element method. The micropolar hypoplastic constitutive models in the last chapter are used.

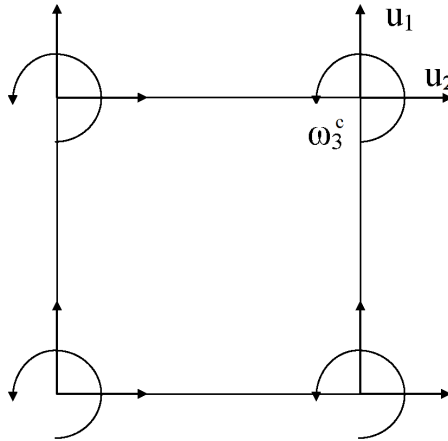


Figure 5.2: A 2D element for micropolar continuum in Abaqus

For the finite element implementation, a 2D four node element is used. Each node has both translational and rotational degrees of freedom. For the micropolar continuum, the generalized displacement \mathbf{u} , generalized velocity $\dot{\mathbf{u}}$, generalized stress \mathbf{T}_g and generalized Strain rate \mathbf{D}_g

can be represented as:

$$\mathbf{u} = \begin{pmatrix} u_1 \\ u_2 \\ \omega_3^c \end{pmatrix}, \dot{\mathbf{u}} = \begin{pmatrix} \dot{u}_1 \\ \dot{u}_2 \\ \dot{\omega}_3^c \end{pmatrix}, \mathbf{T}_g = \begin{pmatrix} \mathbf{T}_{11} \\ \mathbf{T}_{22} \\ \mathbf{T}_{33} \\ \mathbf{T}_{12} \\ \mathbf{T}_{21} \\ \mathbf{M}_{31} \\ \mathbf{M}_{32} \end{pmatrix}, \mathbf{D}_g = \begin{pmatrix} \mathbf{D}_{11} \\ \mathbf{D}_{22} \\ \mathbf{D}_{33} \\ \mathbf{D}_{12} \\ \mathbf{D}_{21} \\ \mathbf{K}_{31} \\ \mathbf{K}_{32} \end{pmatrix} \quad (5.3)$$

By applying a standard discretization procedure, a continuum domain can be partitioned into an assembly of elements. Within a four node element, the interpolation for generalized kinematic quantities is given by

$$\mathbf{u} = \sum_{K=1}^4 N_K \mathbf{u}^K, \dot{\mathbf{u}} = \sum_{K=1}^4 N_K \dot{\mathbf{u}}^K, \mathbf{D}_g = \sum_{K=1}^4 \boldsymbol{\beta}_K \dot{\mathbf{u}}^K \quad (5.4)$$

Where $\mathbf{N}_k = N_k \mathbf{I}$ and N_k are the standard bilinear shape functions with respect to node $K = 1, 2, 3, 4$. Matrix $\boldsymbol{\beta}_K$ has the form of:

$$\boldsymbol{\beta}_K = \begin{pmatrix} \frac{\partial N_K}{\partial x_1} & 0 & 0 \\ 0 & \frac{\partial N_K}{\partial x_2} & 0 \\ 0 & 0 & 0 \\ \frac{\partial N_K}{\partial x_2} & 0 & N_k \\ 0 & \frac{\partial N_K}{\partial x_1} & -N_k \\ 0 & 0 & l \frac{\partial N_K}{\partial x_1} \\ 0 & 0 & l \frac{\partial N_K}{\partial x_2} \end{pmatrix} \quad (5.5)$$

In order to avoid volume locking of a full element integration, a selective reduced integration

technique is used. This is applied by modifying the kinematical matrix β_K :

$$\bar{\beta}_K = \begin{pmatrix} \frac{1}{2} \left(\frac{\partial \bar{N}_K}{\partial x_1} + \frac{\partial N_K}{\partial x_1} \right) & \frac{1}{2} \left(\frac{\partial \bar{N}_K}{\partial x_2} - \frac{\partial N_K}{\partial x_2} \right) & 0 \\ \frac{1}{2} \left(\frac{\partial \bar{N}_K}{\partial x_1} - \frac{\partial N_K}{\partial x_1} \right) & \frac{1}{2} \left(\frac{\partial \bar{N}_K}{\partial x_2} + \frac{\partial N_K}{\partial x_2} \right) & 0 \\ 0 & 0 & 0 \\ \frac{\partial N_K}{\partial x_2} & 0 & N_k \\ 0 & \frac{\partial N_K}{\partial x_1} & -N_k \\ 0 & 0 & l \frac{\partial N_K}{\partial x_1} \\ 0 & 0 & l \frac{\partial N_K}{\partial x_2} \end{pmatrix} \quad (5.6)$$

where

$$\frac{\partial \bar{N}_K}{\partial x_i} = \frac{1}{V_{el}} \int_{V_{el}} \frac{\partial N_K}{\partial x_i} dV \quad (5.7)$$

With the modified matrix, the relation between the rate of curvature and the rate of micropolar rotation remains unchanged.

In order to get the element stiffness matrix, partial differentiations of the constitutive model (equations (4.28) and (4.29)) are carried out. The element stiffness matrix for $m \neq n$ is

$$\frac{\partial \dot{\mathbf{T}}_{ij}}{\partial \mathbf{D}_{mn}} = C_1 \text{tr} \mathbf{T} + C_3 \frac{\mathbf{T}_{mn} \mathbf{T}_{ij}}{\text{tr} \mathbf{T}} + C_4 (\mathbf{T}_{ij} + \mathbf{T}_{ij}^*) \frac{\mathbf{D}_{mn}}{\sqrt{\|\mathbf{D}\|^2 + l^2 \|\mathbf{K}\|^2}} \quad (5.8)$$

$$\frac{\partial \dot{\mathbf{M}}_{ij}}{\partial \mathbf{D}_{mn}} = C_3 \frac{\mathbf{T}_{mn} \mathbf{M}_{ij}}{\text{tr} \mathbf{T}} + 2C_4 \mathbf{M}_{ij} \frac{\mathbf{D}_{mn}}{\sqrt{\|\mathbf{D}\|^2 + l^2 \|\mathbf{K}\|^2}} \quad (5.9)$$

$$\frac{\partial \dot{\mathbf{T}}_{ij}}{\partial \mathbf{K}_{mn}} = -C_3 \frac{\mathbf{M}_{mn} \mathbf{T}_{ij}}{\text{tr} \mathbf{T}} + C_4 (\mathbf{T}_{ij} + \mathbf{T}_{ij}^*) \frac{l^2 \mathbf{K}_{mn}}{\sqrt{\|\mathbf{D}\|^2 + l^2 \|\mathbf{K}\|^2}} \quad (5.10)$$

$$\frac{\partial \dot{\mathbf{M}}_{ij}}{\partial \mathbf{K}_{mn}} = C_1 l^2 \text{tr} \mathbf{T} - C_3 \frac{\mathbf{M}_{mn} \mathbf{M}_{ij}}{\text{tr} \mathbf{T}} + 2C_4 \mathbf{M}_{ij} \frac{l^2 \mathbf{K}_{mn}}{\sqrt{\|\mathbf{D}\|^2 + l^2 \|\mathbf{K}\|^2}} \quad (5.11)$$

For $m = n$, the second term must be added, so equations (5.8) and (5.9) become:

$$\frac{\partial \dot{\mathbf{T}}_{ij}}{\partial \mathbf{D}_{mn}} = C_1 \text{tr} \mathbf{T} + C_2 \mathbf{T}_{ij} + C_3 \frac{\mathbf{T}_{mn} \mathbf{T}_{ij}}{\text{tr} \mathbf{T}} + C_4 (\mathbf{T}_{ij} + \mathbf{T}_{ij}^*) \frac{\mathbf{D}_{mn}}{\sqrt{\|\mathbf{D}\|^2 + l^2 \|\mathbf{K}\|^2}} \quad (5.12)$$

$$\frac{\partial \dot{\mathbf{M}}_{ij}}{\partial \mathbf{D}_{mn}} = C_2 \mathbf{M}_{ij} + C_3 \frac{\mathbf{T}_{mn} \mathbf{M}_{ij}}{\text{tr} \mathbf{T}} + 2C_4 \mathbf{M}_{ij} \frac{\mathbf{D}_{mn}}{\sqrt{\|\mathbf{D}\|^2 + l^2 \|\mathbf{K}\|^2}} \quad (5.13)$$

while equations (5.10) and (5.11) remain the same.

In case of 2D elements, equations (5.8) (5.12), (5.9) (5.13), (5.10) and (5.11) are (5×5) , (5×2) , (2×5) and (2×2) matrixes, which result in a system matrix $\mathbf{H}(\mathbf{T}, \mathbf{D}, \mathbf{M}, \mathbf{K})$ as shown in Table 5.1

$\frac{\partial \dot{\mathbf{T}}_{ij}}{\partial \mathbf{D}_{mn} (5 \times 5)}$	$\frac{\partial \dot{\mathbf{T}}_{ij}}{\partial \mathbf{K}_{mn} (2 \times 5)}$
$\frac{\partial \dot{\mathbf{M}}_{ij}}{\partial \mathbf{D}_{mn} (5 \times 2)}$	$\frac{\partial \dot{\mathbf{M}}_{ij}}{\partial \mathbf{K}_{mn} (2 \times 2)}$

Table 5.1: Stiffness matrix of micropolar hypoplastic model

The system is integrated by assuming a virtual time step Δt :

$$\mathbf{T}_{t_{n+1}} = \mathbf{T}_{t_n} + \dot{\mathbf{T}}\Delta t = \mathbf{T}_{t_n} + \mathbf{H}(\mathbf{T}, \mathbf{D}, \mathbf{M}, \mathbf{K})\mathbf{D}\Delta t \quad (5.14)$$

In order to carry out this integration, an initial stress state \mathbf{T}_{t_0} need to be assumed. An isotropic stress state with a proper mean stress is normally used.

The simulation results with this finite element implementation will be shown in the next chapter.

Chapter 6

Result and discussion

6.1 Single element simulation

First, a single element simulation with the implemented model is carried out, as shown in Figure 6.1. Boundary conditions are defined similar as a biaxial test. Starting from an isotropically loaded case, the element is first loaded and then unloaded with constant vertical deformations. The results obtained from single element simulation (stress and volume strain) are compared with analytical simulation with the same constitutive model, see Figure 6.2.

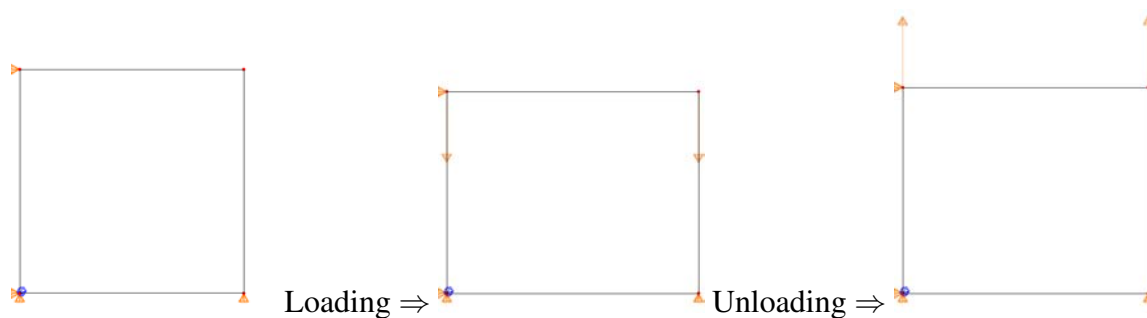


Figure 6.1: Single element simulation in Abaqus

It can be seen that the same stress-strain and volume strain curves are given by FEM element simulation and analytical solution. Hence, the model is properly implemented into Abaqus element. However, the micropolar effect cannot be seen in single element test. Hence, some other simulations are carried out and the results are shown in the following.

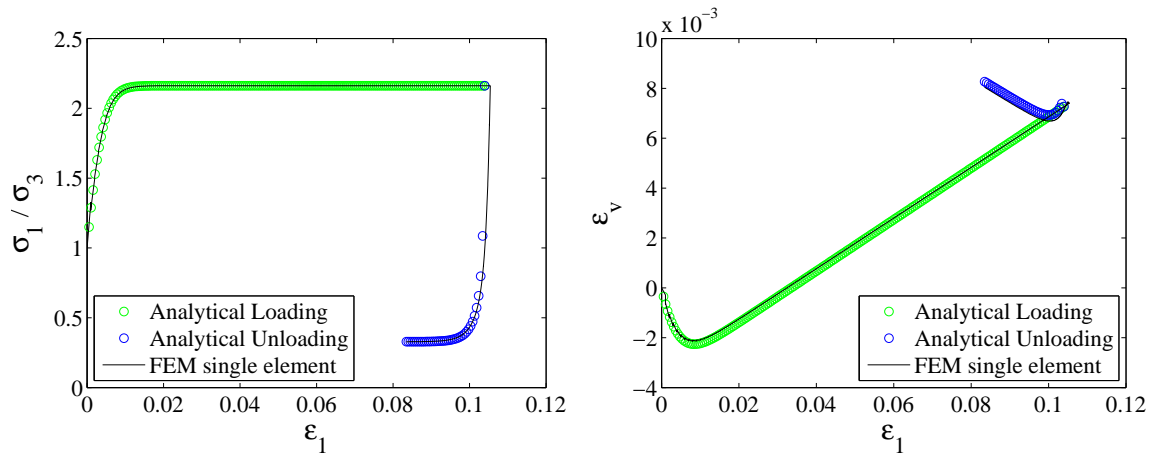


Figure 6.2: Stress-strain and volume strain curves

6.2 Biaxial test

In this section, biaxial tests are simulated with the micropolar hypoplastic model in FEM. From the simulation result, shear bands with certain width can be obtained. The internal length can be determined by analyzing the width of shear bands, such that the result matches the real experimental width.

Model: The model has a height of 100 mm and a width of 25 mm. It is known that strain localization cannot be modeled in a perfectly homogeneous FEM model. Hence, inhomogeneity must be added to the model. This is realized by defining some "soft elements" in the model, as shown in Figure 6.3. The "soft elements" have a size of $12.5 \text{ mm} \times 12.5 \text{ mm}$ and are 10 mm away to the bottom of the model.

Normal elements have a friction angle of 35° and a Young's module of 200 times the isotropic stress, the "soft elements" have a friction angle of 30° and a Young's module of 180 times the isotropic stress. The material parameters of both elements are calculated with equation (3.43), and details are shown in Table 6.1.

In order to obtain shear bands with different width, internal lengths between 0.1 – 1.0 mm are used in the model. The mesh size is $0.1 \times 0.1 \text{ mm}$. However, it will be shown that the mesh size do not have big effects on the simulation results.

Boundary conditions: There are two steps in the biaxial test simulation: isotropic loading and biaxial loading, for both steps appropriate boundary conditions need to be applied. The first step is isotropic loading. The boundary conditions for the bottom nodes are given by

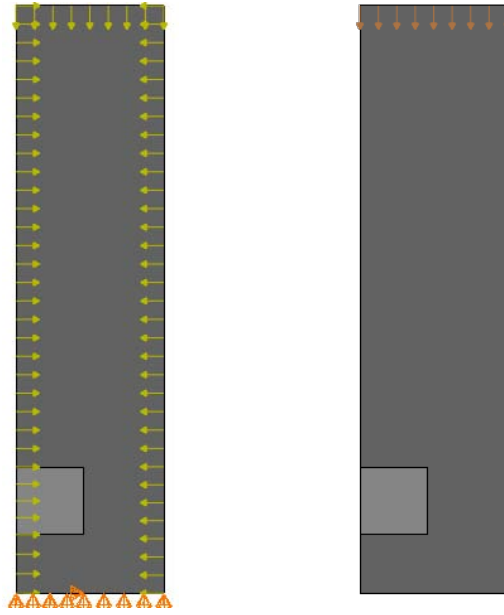


Figure 6.3: FEM model of the biaxial test, normal and soft elements are dark and light gray

Normal elements			
$E(\text{MPa})/\sigma_c$	$\phi(^{\circ})$	$\psi(^{\circ})$	ν_i
200	35	10	0.2
C_1	C_2	C_3	C_4
-55.56	-142.55	-523.67	-151.01
Soft elements			
$E(\text{MPa})/\sigma_c$	$\phi(^{\circ})$	$\psi(^{\circ})$	ν_i
180	30	10	0.2
C_1	C_2	C_3	C_4
-50.00	-110.71	-646.15	-159.40

Table 6.1: Material parameters for the FEM simulation of biaxial test

fixing the vertical displacements and the horizontal displacement in the middle point of the bottom, therefore the model is symmetric. The other three sides of the model is isotropically loaded with a pressure of 100 kPa, as shown in the left of Figure 6.3. The moment on the all the boundary nodes are set to be zero. In the biaxial loading step, the rotations in left and right sides of the sample are set to be free, and all other boundary conditions above remains the same. In addition, a constant displacement is applied on the nodes on the top of model, as shown in the right of Figure 6.3.

Results: The results of simulations with different internal lengths are shown in Figure 6.4 and 6.5, in which colors show the counter-clockwise rotation of nodes.

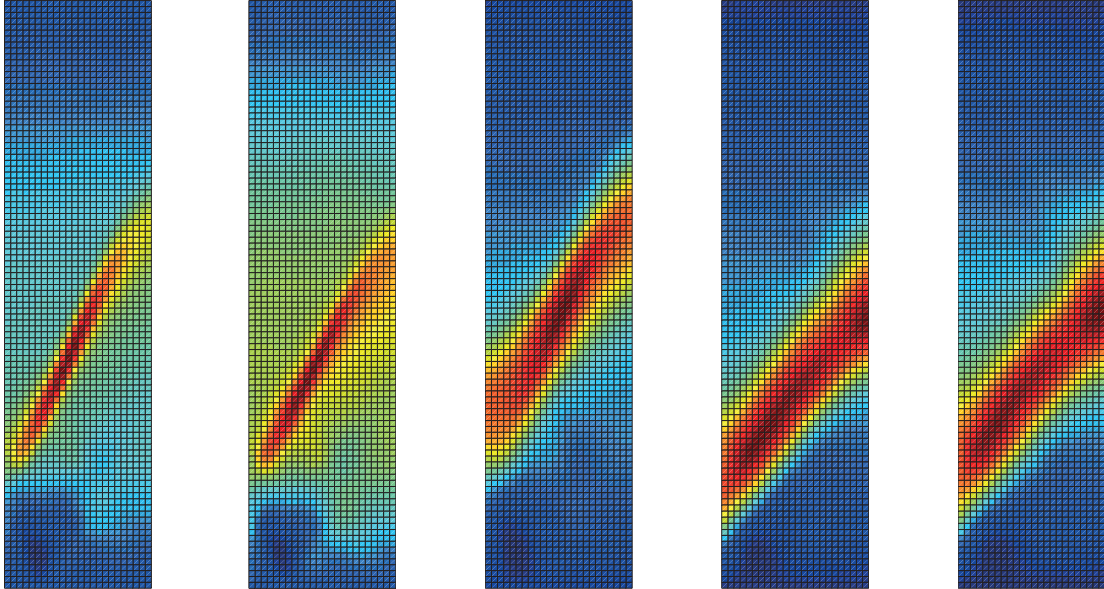


Figure 6.4: FEM simulation results of the biaxial test on undeformed mesh, internal lengths 0.1, 0.25, 0.5, 0.75 and 1.0 mm

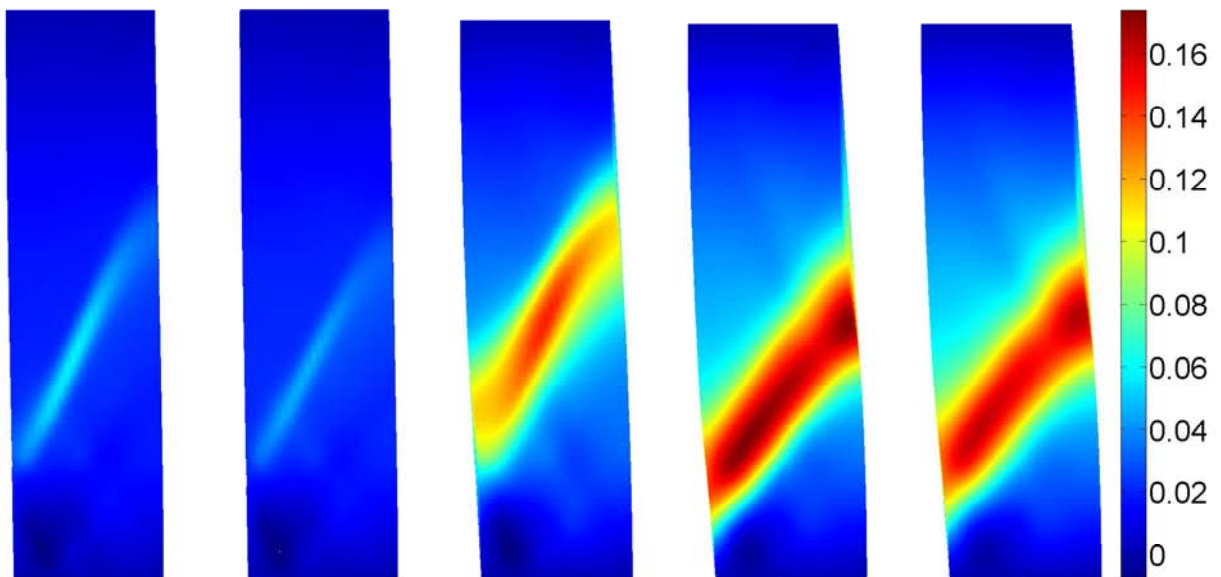


Figure 6.5: FEM simulation results of the biaxial test on deformed shape, internal lengths 0.1, 0.25, 0.5, 0.75 and 1.0 mm, unified deformation and color bar (in radian)

The stress-strain curves of the biaxial tests are shown in Figure 6.6

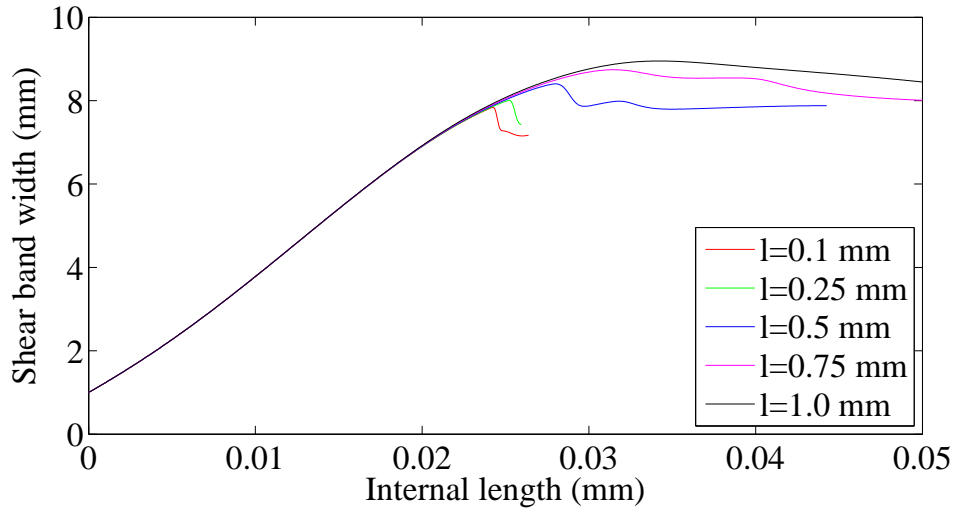


Figure 6.6: Stress strain curve of the FEM simulation

Since the same material parameters C_1-C_4 are used for all simulations, it can be expected that all stress-strain curves coincide at the beginning. However, for different internal lengths, the bifurcation points are different. The smaller the internal length the earlier the bifurcation. For small internal lengths (0.1 and 0.25 mm), the softening effect is so large that the solutions do not converge shortly after the bifurcation point. For large internal lengths, the softening continues until a critical state is reached. In classical mechanics, the post-bifurcation behavior cannot be modeled correctly due to the lack of internal length.

Shear band width: It can be seen from the Figures that the width of the shear band shows a dependency on the internal length. Larger internal length gives larger shear band width, which can be expected. It is known that in a FEM simulation using micropolar constitutive model, the width of the shear band should be mesh independent, which means that different mesh size should predict the same shear band width with the same set of material parameters. This is verified by carrying out simulations with finer mesh. For internal length 0.5 and 1.5 mm, the same biaxial test is modeled with mesh size 0.1 and 0.05 mm. For both fine mesh and coarse mesh the moment on the boundary nodes are set to be zero, the same material parameters are used. The results are shown in Figure 6.7.

It can be seen that the same shear band width is predicted by both fine mesh and coarse mesh. Hence, there is no mesh dependency for the FEM simulation using the micropolar hypoplastic constitutive model.

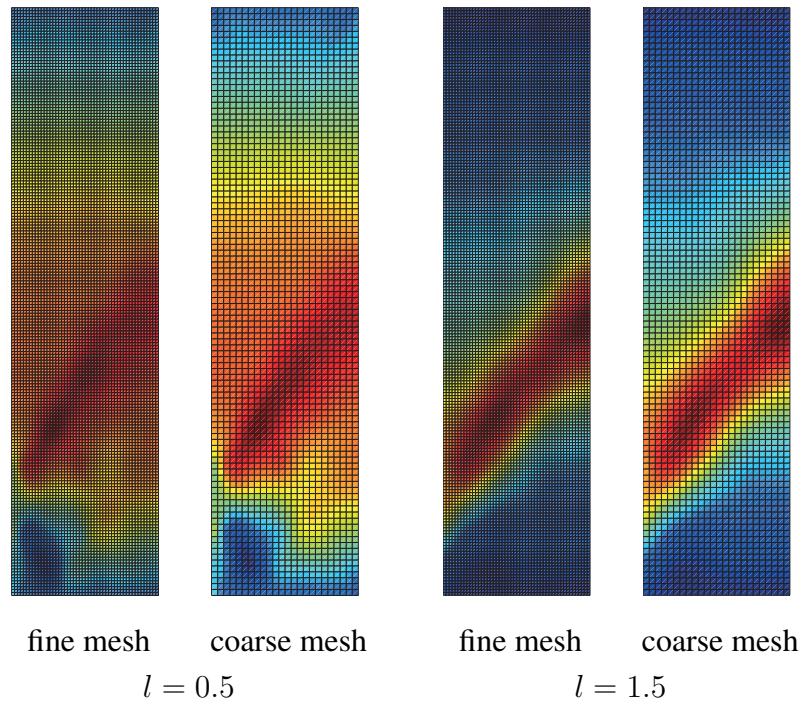


Figure 6.7: FEM simulation results of the biaxial test with different mesh size

Therefore, a relationship between the shear band width and the internal length should be determined. This can be used for back analysis to obtain the internal length. The relationship between the shear band width and the internal length is plotted in Figure 6.8.

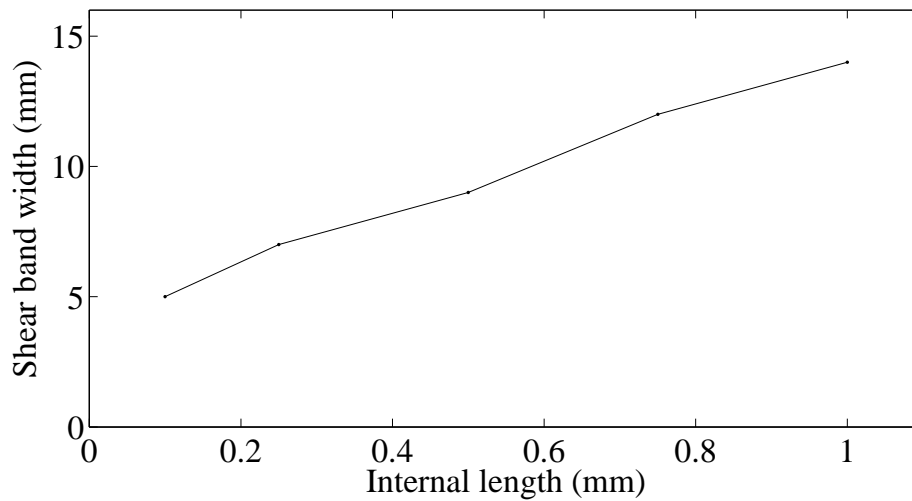


Figure 6.8: Relationship between shear band width and internal length

It can be seen that the relationship between the shear band width and the internal length is linear. Theoretically, the shear band width should be zero if the internal length is zero. However

this cannot be realized either in numerical calculations or in physical experiments. Hence, according to the simulations, the shear band width has a starting value (about 4 mm). Taking away the starting value, the shear band width is about ten times the internal length. Hence, the internal length can be determined by $l = (l_s - 4 \text{ mm})/10$, where l_s is the shear band width.

6.3 Pore ratio dependent behavior

The pore ratio dependency can be added to the new model as shown in equations (4.31) and (4.32) in section 4.2.3. Hence, simulations of pore ratio dependent behavior can be carried out. Here, the biaxial test is taken as an example to reproduce the experiments of Rechenmacher in [11]. In the experiment, the sand specimen is 137 mm tall by 39.5 mm wide by 79.7 mm deep (out-of plane). It is prepared by dry pluviation. By using different dropping heights for different parts of the specimen, a dense sand specimen with a layer of loose sand is obtained, as shown in the CT image in Figure 6.9(a).

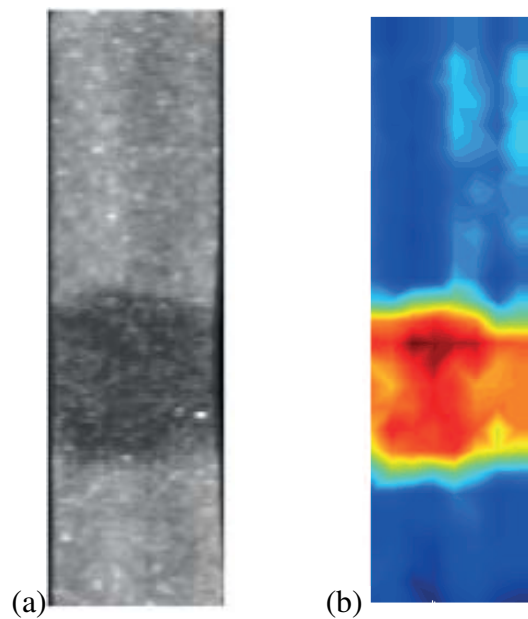


Figure 6.9: Pore ratio distribution: (a) CT image (b) FEM simulation

In the FEM simulation, the same pore ratio distribution is used as shown in Figure 6.9(b). The material parameters are inferred according to the elastic-plastic material parameters used in [11]. The internal length is assumed to be 0.42 mm, which equals to the mean grain diameter of the sand sample.

The simulation procedure is the same as the biaxial test simulations in the last section, expect

the constitutive model defined by equations (4.31) and (4.32) is used and the pore ratios are updated according to equation (4.32). The results are shown in Figure 6.10, in which colors show the counter-clockwise rotation of nodes.

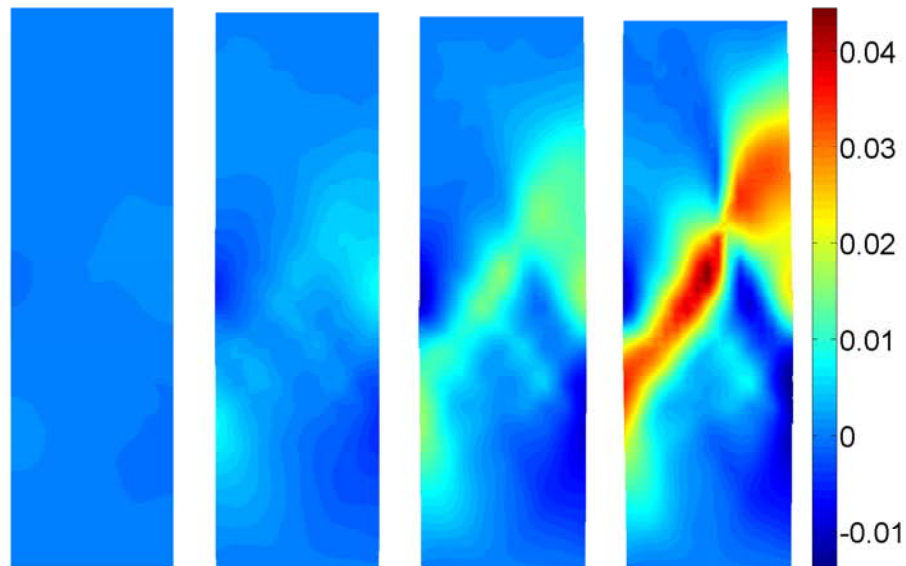


Figure 6.10: FEM simulation results of the biaxial test, vertical strain 0.0073, 0.0146, 0.0219 and 0.0292, colorbar in radian

It can be seen that the pore ratio has a clear effect on the behavior of the material. At the beginning, several small shear bands can be observed. Later, these shear bands localized to one main shear band. Comparing to the experimental results in Figure 6.11, the shear band predicted by simulation has the same inclination and appears in the same position. Hence, the pore ratio dependent behavior of the sand specimen in experiment can be reproduced by the micropolar hypoplastic model.

As specified in the last section, the shear band width only depends on the internal length. This also holds for the simulations with pore ratio dependency. By using different internal length, the results are shown in Figure 6.12.

As a result, an inhomogeneous distribution of the pore ratio acts as imperfection in the model and triggers the shear band. The position of the shear band depends on the pore ratio distribution, but the width of the shear band only depends on the internal length, which can be determined by the grain diameters.

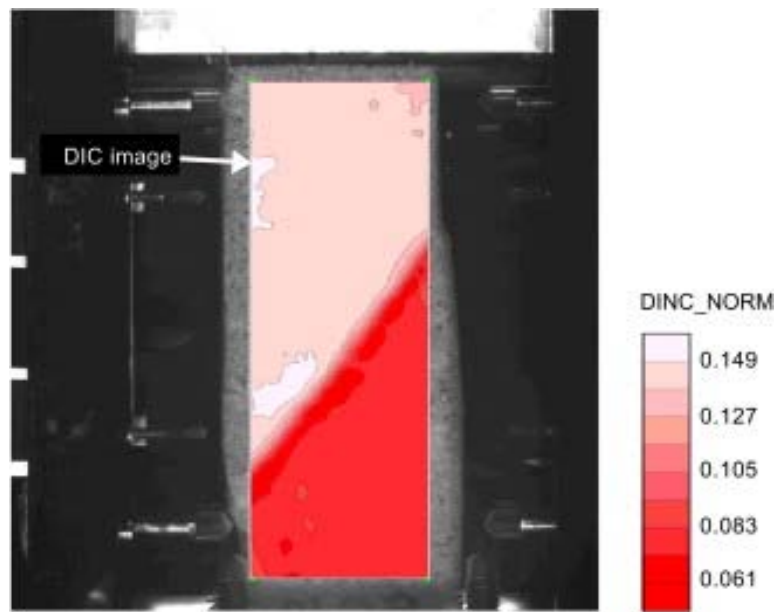


Figure 6.11: Contour of norm of incremental displacement ($\sqrt{u^2 + v^2}$) from Digital Image Correlation (DIC). Color bar in mm, vertical strain 0.06

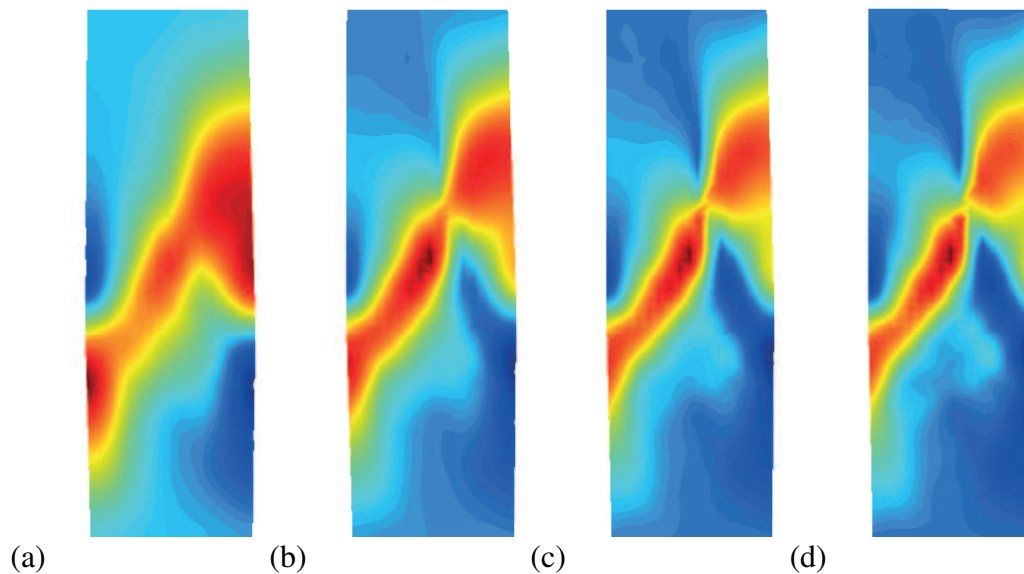


Figure 6.12: FEM simulation results of the biaxial test with different internal length: (a) 4.2 mm (b) 2.1 mm (c) 1.05 mm (d) 0.42 mm

With the same model, the DEM simulation in section 2.2.2 can be modeled with FEM. The initial pore ratio distribution of the DEM simulation is assigned to the FEM model. The material parameters in Table 6.2 are used. The internal length is set to be 0.05 mm.

The biaxial test simulation is carried out the same way as the examples above. The results for

$E(\text{MPa})/\sigma_c$	$\phi(^{\circ})$	$\psi(^{\circ})$	ν_i
200	20	10	0.2
C_1	C_2	C_3	C_4
-55.56	31.52	-1669.95	-271.11

Table 6.2: Material parameters for the FEM simulation of biaxial test with pore ratio dependency

different strains are plotted in Table 6.3(b), while the DEM results of section 2.2.2 are shown in Table 6.3(a). In both plots the momentary rotations are plotted.

From the comparison, it can be seen that by using the pore ratio dependent micropolar hypoplastic model, the result of DEM simulation can be fairly well reproduced with the continuum model. Both methods predict the same shear band location, inclination and width. In the early stage of loading, several small shear bands can be observed in the upper left corner, these shear bands disappear when the main shear bands are formed. In the lower right corner, there are two shear bands parallel to each other at the beginning. Later, these two shear bands merge into one. All these details in DEM simulations can also be predicted by FEM simulation with the micropolar hypoplastic model.

It is known that the particle rotations are different from continuum rotations in micropolar theory. The averaging of discrete rotation depends highly on averaging methods and lengths, which are not consistent. Hence, a quantitative comparison of continuum and discrete rotations are not feasible. However, from Table 6.3, the width of shear band can be quantitatively compared. The width of both small and big shear bands are well predicted by the continuum method.

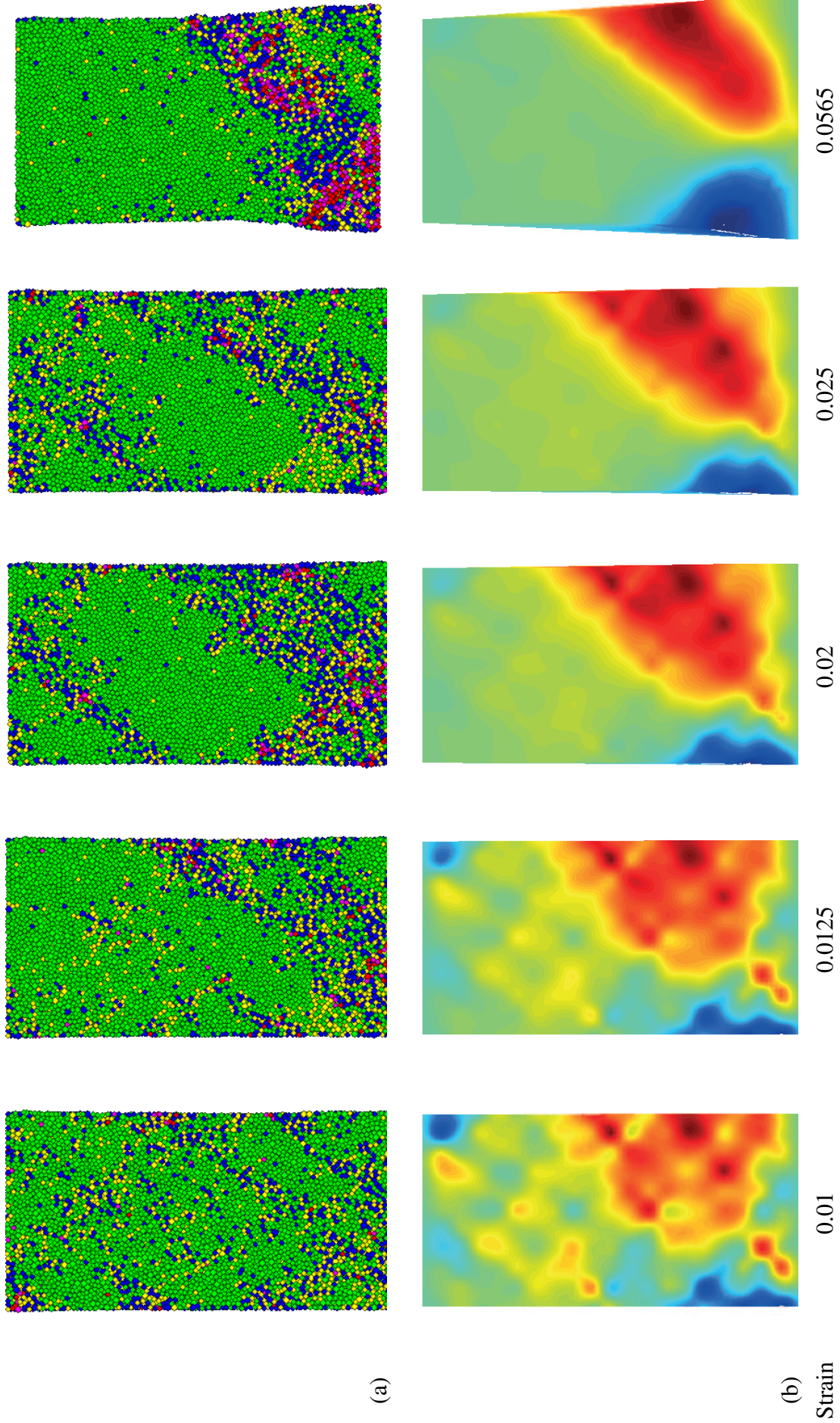


Table 6.3: Simulation of biaxial test (a) DEM (b) FEM

6.4 Periodic shear test

The periodic shear test is the shearing of a infinite long sample. The top surface is moving with a constant speed while the bottom surface is fixed. The model is free in dilation with a constant vertical pressure applied on the top. Since the model is infinite long, periodic boundary conditions are used, in which the left and right sides of the sample are constrained to have the same displacement and rotation. With this boundary condition, it is enough to use only one row of elements, since all the rows in periodic shear are just repetitions of one row, see Figure 6.13.

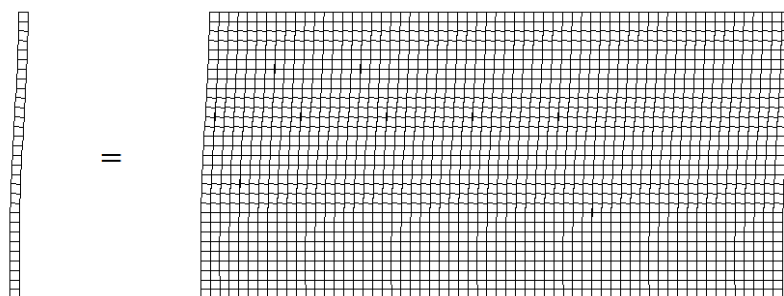


Figure 6.13: Periodic boundary conditions in periodic shear test

The material parameter used for periodic shear modeling is shown in Table 6.4.

$E(\text{MPa})/\sigma_c$	$\phi(^{\circ})$	$\psi(^{\circ})$	ν_i
200	35	0	0.2
C_1	C_2	C_3	C_4
-55.56	-180.56	-372.83	-143.92

Table 6.4: Material parameters for the FEM simulation of periodic shear test

Using different internal lengths, the periodic shear test is modeled, the total rotation of nodes are shown in Figure 6.14. It can be seen that the shear band width depends on the internal length. The smaller the internal length, the thinner the shear band, which is also shown in the simulation of biaxial tests. For very small internal length, several shear bands can occur, the adjacent shear bands have opposite rotations. This can be compared to the rolling of particles, where the adjacent particles rotate oppositely. The magnitudes of rotations according to the vertical axes are plotted in Figure 6.15.

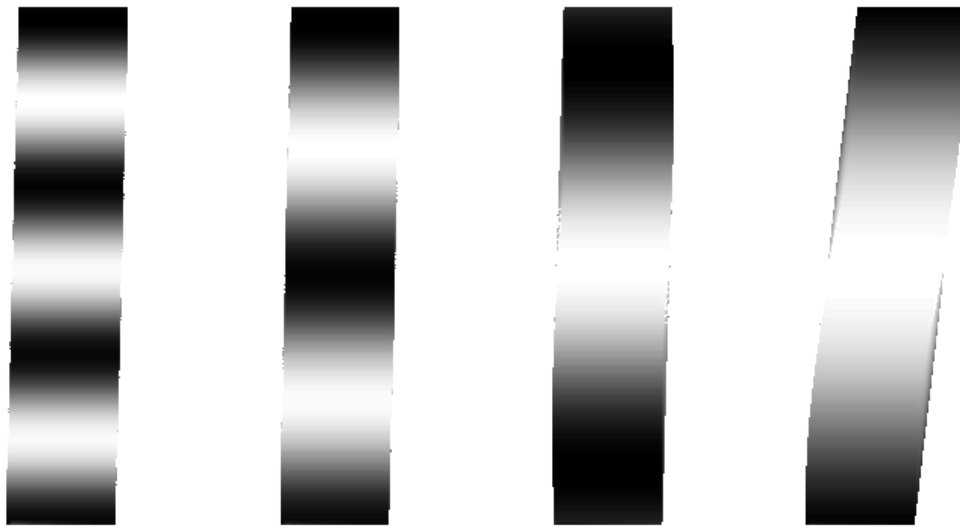


Figure 6.14: FEM simulation results of periodic shear, internal lengths 0.2, 0.5, 1.0 and 2.0 mm, rotations are shown by colors

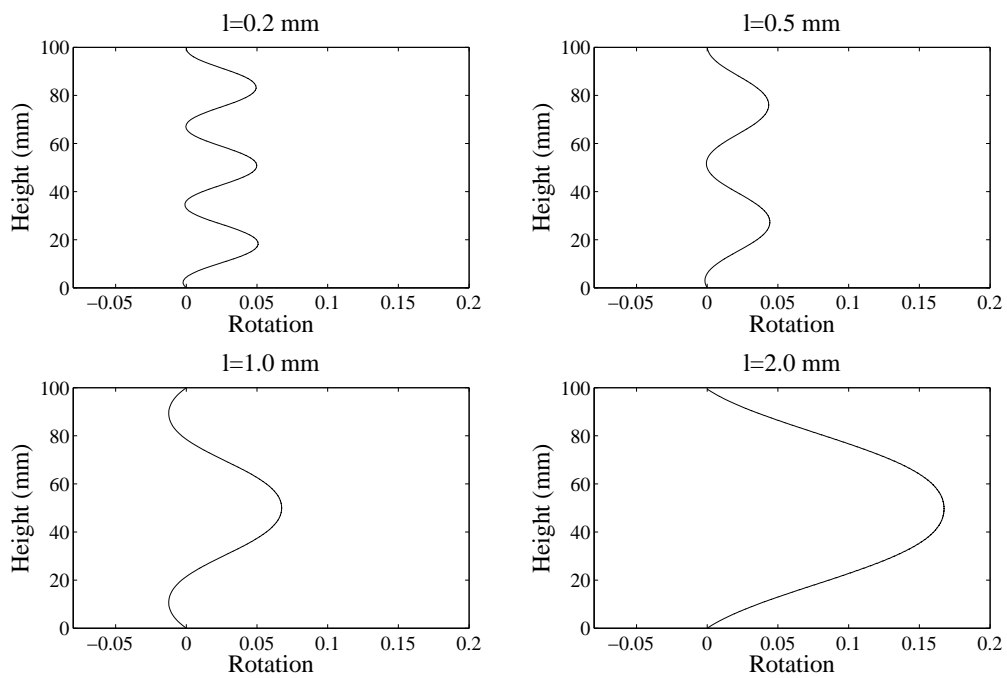


Figure 6.15: FEM simulation results of periodic shear, internal lengths 0.2, 0.5, 1.0 and 2.0 mm, magnitude of rotations are shown

Periodic shear is just a theoretical experiment and cannot be realized in physical experiments. However, a long shear band far from the material boundary can be considered as a periodic shear. With the new micropolar hypoplastic model, microscopic properties of the shear band

can be observed.

6.5 Simple shear test

A DEM simulation of simple shear test is shown in section 2.2.3. Although the simple shear test has a homogeneous strain, the displacements and rotations of individual particles are quite non-uniform. The particles in each corner show different behavior. In the middle, a shear band can be observed, see Figure 6.16.

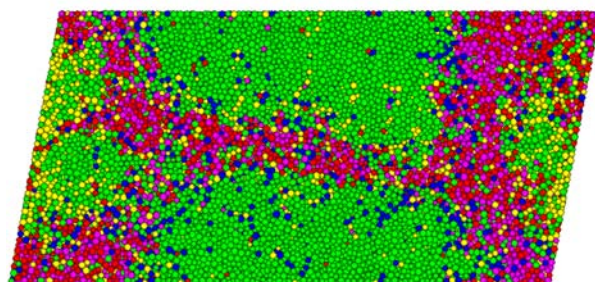


Figure 6.16: DEM simulation of simple shear test

Due to the lack of internal length in classical mechanics, the behavior of simple shear test cannot be modeled. Here, the micropolar hypoplastic model is used to reproduce the simple shear test with FEM simulation.

For the simulation of simple shear test, the material parameters in Table 6.5 are used.

$E(\text{MPa})/\sigma_c$	$\phi(^{\circ})$	$\psi(^{\circ})$	ν_i
200	35	0	0.2
C_1	C_2	C_3	C_4
-55.56	-180.56	-372.83	-143.92

Table 6.5: Material parameters for the FEM simulation of simple shear test

The FEM model of the simple shear test is shown in Figure 6.17. The sample has a height of 40 mm and length of 80 mm. The bottom of the sample ($x = 0$) is fixed in all directions. Initially, an isotropic compressive stress 100 kPa is applied on the model, the couple stress on the boundaries are set to be zero. The shearing process is simulated by applying a constant velocity on the upper surface and constant rotations of two sides, which is realized by different node velocities according to the height of the node (y coordinate). During the shearing

process, the compressive load on the upper surface kept constant, and all the nodes on the upper surface are constraint to have the same displacement in y direction. Hence, a constant normal stress applied by a rigid plate can be simulated. The simulation results are shown in Figure 6.18.

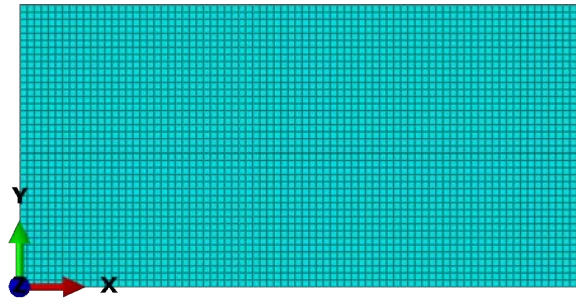


Figure 6.17: FEM model of simple shear test



Figure 6.18: FEM simulation of simple shear test, colorbar in radian

Colors are used to show the node rotations in clockwise direction. Comparing to Figure 6.16, in both DEM and FEM model, large rotations in both sides and in the middle can be observed. It can be seen from the DEM simulation that the shear band in the middle has a small inclination, this is also shown in the FEM simulation. Also, both models show symmetry according to the diagonal axes.

The shear force and shear stress according to the shear strain are plotted in Figure 6.19 and 6.20.

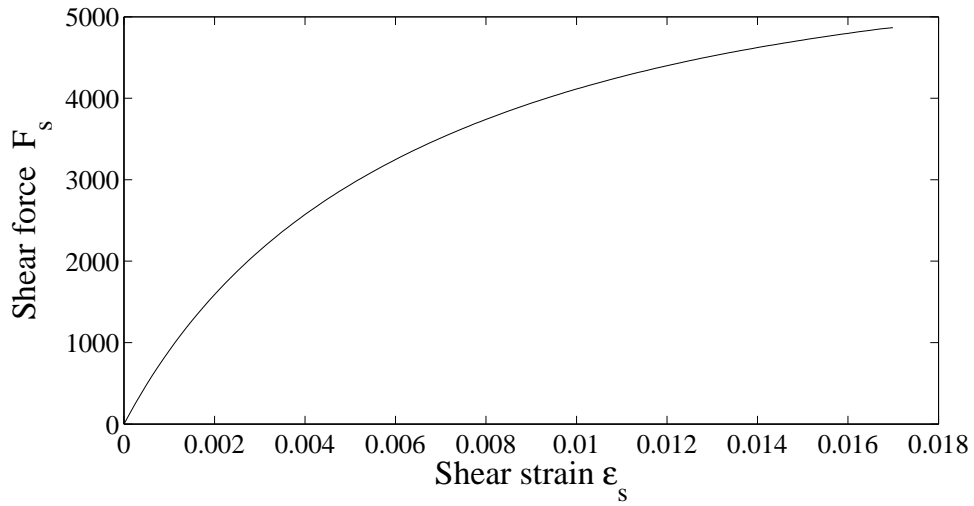


Figure 6.19: Shear force of simple shear test

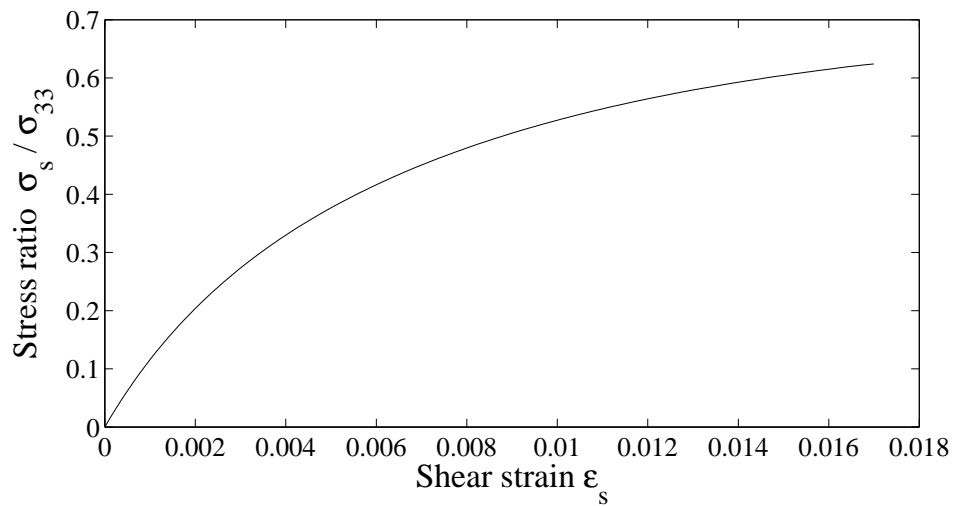


Figure 6.20: Shear stress of simple shear test

6.6 Discussion

All the FEM simulations in this chapter use the new micropolar hypoplastic model (equations 4.28 4.29 and equations (4.31) 4.32) developed in this dissertation, which is obtained by using complex tensor formulations to add micropolar effect into the hypoplastic model. The new micropolar hypoplastic model is so simple that it can be easily implemented into FEM code. Several element tests are simulated. With only one additional material parameter: the internal length, great changes are introduced to the hypoplastic model. Many material behavior, such as rotation, shear localization and size dependent effects, can be modeled with the new model, which is impossible using classical continuum models.

It is shown in the simulations that the shear band width depends on the internal length and is not influenced by the mesh size. By just changing the internal length, different mechanical behavior can be obtained. For all the simulation results, the continuum rotations are plotted, so that the shear bands in these simulations can be easily identified. A relationship between the shear band width and the internal length is set up, which can be used in back analysis to determine the internal length from experiments. By adding pore ratio dependent behavior into the model, it has been shown that the detailed shear band evolution process can be modeled in a biaxial test simulation, the width of shear band in each step can be quantitatively predicted. Comparison with DEM simulations shows that the new model can predict the same rotation profiles as the DEM simulations. However, the FEM simulation is much faster than the DEM simulation. For example, for simulation of simple shear test, the DEM simulation in Figure 6.16 takes about half an hour, while the FEM simulation in 6.18 takes only a few minutes. If smaller particles are modeled, several times more particles have to be used in DEM simulation and the simulation time increases exponentially. In FEM, only the internal length needs to be changed and the simulation time stays more or less the same. Hence, the continuum model has advantage dealing with large systems, and the new model is also able to describe the micro rotations of material due to the internal length and micropolar part, which means this model bridges the micro and macro scales. Same material behavior can be predicted by this model as by DEM simulations, yet much lower computational efforts are required.

Although it has been shown that the FEM simulation with this model is mesh independent, the mesh size should not exceed the width of the shear band. Another limitation of this model is that the micropolar rotation can only be qualitatively compared with discrete rotations, further development in averaging methods and better understanding of micropolar rotation are needed.

Chapter 7

Conclusion and outlook

7.1 Conclusion

Modeling of granular material is a challenging topic. It has been studied in many different disciplines by many researchers, but there are still many open questions. The modeling methods can be divided into two main groups, discrete methods and continuum methods. Both methods have their advantages and limitations, hence, both methods are widely used and links between these two methods are searched by many researchers.

In this dissertation, both discrete and continuum method are studied. Discrete element method is taken as an example of discrete method. For the continuum method, some advanced continuum models are shown, including hypoplastic model and micropolar theory.

The DEM method was invented by Cundall [15] in 1979. With the development of computer technology, this method become more and more functional. The advantage of DEM is that it can precisely model the microstructure of granular materials and obtain highly detailed information in microscale. Several examples are shown in this dissertation. However, this method is limited by computational power and modeling of a real sized problem is still unrealistic.

The hypoplastic model is a constitutive model developed for granular materials. The original idea was given by Kolymbas [29] in 1977. The model is improved and named as hypoplastic model by Wu and Kolymbas [54] in 1990 . Hypoplastic model are nonlinear tensorial functions of the rate-type.

Micropolar theory is first developed by the Cosserat brothers [14] in 1909, and widely noticed since 1968 [31]. Classical continuum theories do not have any internal length scale and therefore cannot account for problems with scale dependence. The micropolar theory considers the independent rotational degrees of freedom of each material point. As a result, in addition to the stress-strain relationship, the relationship between couple stress and curvature

needs to be considered. The micropolar theory can be used for scale dependent problems, since an internal length scale is included in this model. Due to the lack of experimental data at the microscale, micropolar constitutive models cannot be set up directly. Hence, micropolar constitutive models are normally developed through mathematical approaches. However, calibration of material parameters for these micropolar constitutive models cannot be easily done.

In this dissertation, a new model is developed which combines the hypoplastic model and micropolar theory. This is realized by using complex tensor formulations. General complex tensors are assumed, in which the real parts are classical continuum terms (stress, strain, etc.) and the imaginary parts are micropolar terms (couple stress, curvature, etc.). A characteristic length is added in the complex tensors to balance the dimensions. By substituting these complex tensors into the hypoplastic equations and separating the real and imaginary parts, a new constitutive model based on the hypoplastic model and micropolar theory is obtained. The model is largely simplified by assuming that the tensors of stress, strain and their rates are symmetric, the tensors of moment stress, curvature and their rates are antisymmetric. The resulting model shows coupling between the stress-strain variables and the moment-curvature variables to some extent and is much simpler than any existing micropolar hypoplastic model. The only additional material parameter is the characteristic length, which can be determined from the width of the shear band.

Using complex tensor formulations is a novel method to develop micropolar constitutive models. Complex tensors have been widely used in theoretical physics. It is shown in this thesis that it works fairly well for developing micropolar constitutive models. This method is not limited to hypoplastic models. It can be used for any constitutive model in tensor form.

This new model is implemented to a 2D FEM element in ABAQUS, each node has three degrees of freedom (two translations and one rotation). Biaxial tests, periodic shear tests and simple shear tests are simulated with this model. By using different internal lengths, size dependent material behavior is shown with the new model. The relationship between the shear band width and the internal length is discussed. The results of the biaxial test simulation are compared to the experiments and DEM simulations. The result of the simple shear test is compared with DEM simulation. These comparisons show that the microstructure of the material can be fairly well predicted with the micropolar hypoplastic model. The width of the shear band can be well predicted. With a pore ratio dependent model, the same evolution process of the shear bands can be observed in both DEM and FEM simulations. However, the continuum modeling requires much lower computational efforts.

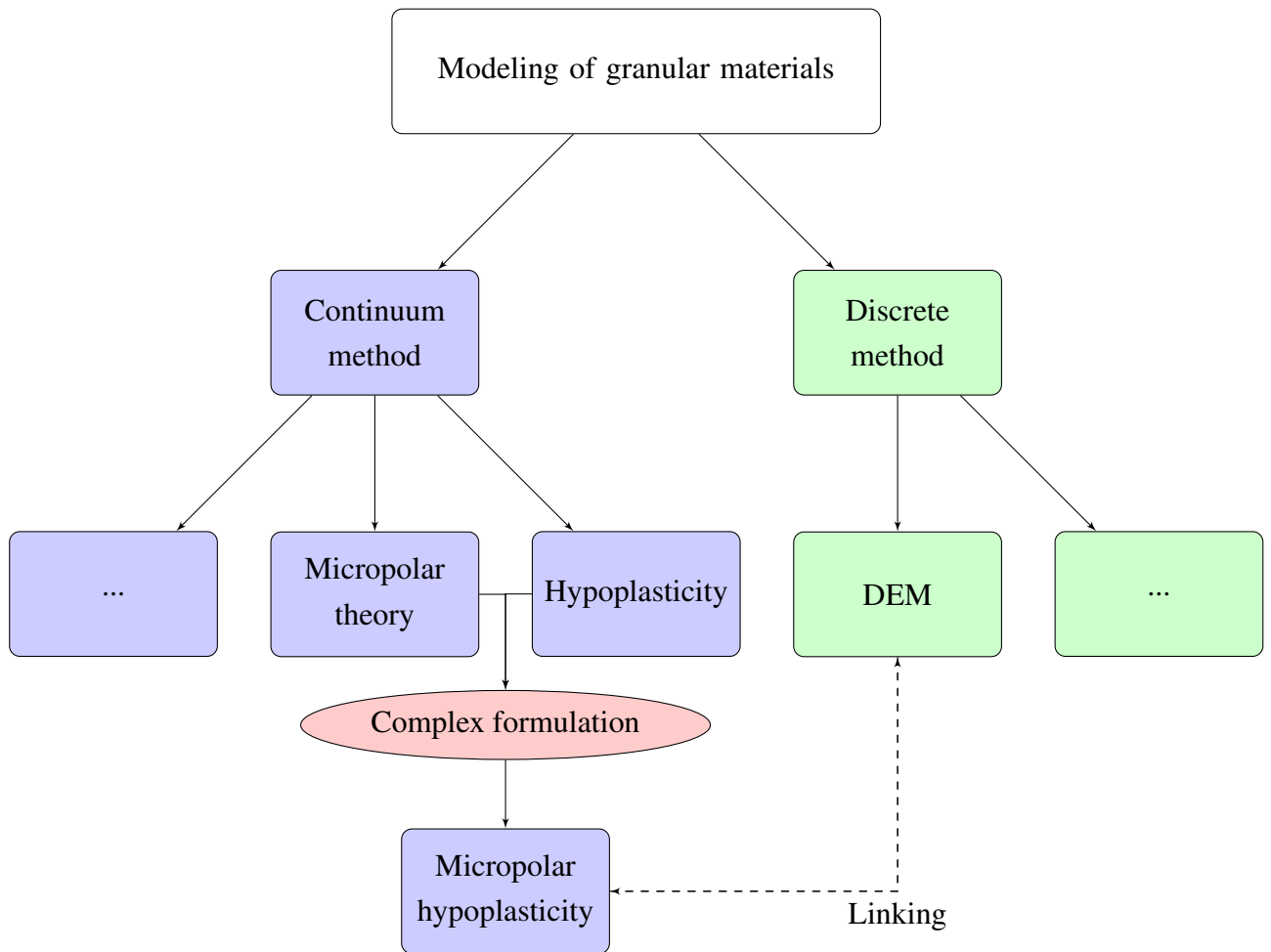


Figure 7.1: Linking DEM with micropolar continuum

7.2 Outlook

In this dissertation, a new micropolar hypoplastic constitutive model is developed with the help of complex tensor formulations. The model is implemented into FEM and compared with DEM simulations. Based on the results of this dissertation, several problems can be further studied.

Using complex tensor formulation for micropolar continuum is shown to be applicable. As shown in section 4.3, this method is not limited to the hypoplastic model. This method offers a simple mathematical way to obtain micropolar models. It should be further applied to other classical constitutive models. The physical meaning of the complex part should be discussed, which leads to a better understanding of the micropolar constitutive model.

More DEM simulations should be carried out and compared with the micropolar hypoplastic model. The relation between the microscale material parameter and the continuum material parameters should be studied, which promotes further development of both DEM and continuum methods.

Several simulations with the new micropolar hypoplastic model are carried out in this dissertation. It is shown that the model has a well performance with relatively low computational power. This model should be used to simulated more complicated problems and should be implemented into 3D numerical methods. Due to the simplicity of the model and the capability of modeling large scale models, it is also possible to apply it to industrial designs.

The model should be further developed. It is shown that the void ratio dependency can be added into the model. Similarly the model can be extended with cohesion, anisotropy, viscosity and thermal effects. All these extensions have already been applied to the classical hypoplastic model and work fairly well. Using micropolar hypoplastic model will bring these constitutive models into a new level. Many unprecedented problems will be solved.

Bibliography

- [1] B. Akgöz and Ö. Civalek. Buckling analysis of cantilever carbon nanotubes using the strain gradient elasticity and modified couple stress theories. *Journal of Computational and Theoretical Nanoscience*, 8(9):1821–1827, 2011.
- [2] B. Akgöz and Ö. Civalek. Strain gradient elasticity and modified couple stress models for buckling analysis of axially loaded micro-scaled beams. *International Journal of Engineering Science*, 49(11):1268–1280, 2011.
- [3] M.P. Allen and D.J. Tildesley. *Computer simulation of liquids*. Oxford science publications. Clarendon Press, 1989.
- [4] K. Bagi. Stress and strain in granular assemblies. *Mechanics of Materials*, 22(3):165–177, 1996.
- [5] K. Bagi. Microstructural stress tensor of granular assemblies with volume forces. *Journal of Applied Mechanics, Transactions ASME*, 66(4):934–936, 1999.
- [6] K. Bagi. Analysis of microstructural strain tensors for granular assemblies. *International Journal of Solids and Structures*, 43(10):3166–3184, 2006.
- [7] J.P. Bardet and I. Vardoulakis. Asymmetry of stress in granular media. *International Journal of Solids and Structures*, 38(2):353–367, 2001.
- [8] G. Bartels, T. Unger, D. Kadau, D.E. Wolf, and J. Kertész. The effect of contact torques on porosity of cohesive powders. *Granular Matter*, 7(2-3):139–143, 2005.
- [9] E. Bauer. Calibration of a comprehensive hypoplastic model for granular materials. *Soils and Foundations*, 36(1):13–26, 1996.
- [10] N. Bogdanova-Bontcheva and H. Lippmann. Rotationally symmetric plane flow of a granular material [Rotationssymmetrisches ebenes Fliessen eines granularen Modellmaterials]. *Acta Mechanica*, 21(1-2):93–113, 1975.

- [11] R.I. Borja, X. Song, A.L. Rechenmacher, S. Abedi, and W. Wu. Shear band in sand with spatially varying density. *Journal of the Mechanics and Physics of Solids*, 61(1):219–234, 2013. cited By (since 1996) 0.
- [12] C.S. Chang and L. Ma. A micromechanical-based micropolar theory for deformation of granular solids. *International Journal of Solids and Structures*, 28(1):67–86, 1991.
- [13] J. Christoffersen, M.M. Mehrabadi, and S. Nemat-Nasser. Micromechanical description of granular material behavior. *Journal of Applied Mechanics, Transactions ASME*, 48(2):339–344, 1981.
- [14] E. Cosserat and F. Cosserat. *Théorie des corps déformables*. Cornell University Library historical math monographs. A. Hermann et fils, 1909.
- [15] P.A. Cundall and O.D.L. Strack. Discrete numerical model for granular assemblies. *Geotechnique*, 29(1):47–65, 1979.
- [16] E. Dintwa, M. Van Zeebroeck, E. Tjjskens, and H. Ramon. Torsion of viscoelastic spheres in contact. *Granular Matter*, 7(2-3):169–179, 2005.
- [17] O. Durán, N.P. Kruyt, and S. Luding. Analysis of three-dimensional micro-mechanical strain formulations for granular materials: Evaluation of accuracy. *International Journal of Solids and Structures*, 47(2):251–260, 2010.
- [18] O. Durán, N.P. Kruyt, and S. Luding. Micro-mechanical analysis of deformation characteristics of three-dimensional granular materials. *International Journal of Solids and Structures*, 47(17):2234–2245, 2010.
- [19] W. Ehlers, E. Ramm, S. Diebels, and G.A. D’Addetta. From particle ensembles to cosserat continua: Homogenization of contact forces towards stresses and couple stresses. *International Journal of Solids and Structures*, 40(24):6681–6702, 2003.
- [20] D. Els. Definition of roll velocity for spherical particles. 2006.
- [21] J.L. Ericksen and C. Truesdell. Exact theory of stress and strain in rods and shells. *Archive for Rational Mechanics and Analysis*, 1(1):295–323, 1957.
- [22] A.C. Eringen. *Continuum Physics: Polar and non-local field theories*. Continuum Physics. Academic Press, 1976.
- [23] A.C. Eringen. *Microcontinuum field theories*. Number Bd. 2 in Microcontinuum Field Theories. Springer, 2001.

- [24] J.D. Goddard. Granular hypoplasticity with cosserat effects. volume 1227, pages 323–332, 2010.
- [25] G. Gudehus. Comprehensive constitutive equation for granular materials. *Soils and Foundations*, 36(1):1–12, 1996.
- [26] A.R. Hadjesfandiari and G.F. Dargush. Couple stress theory for solids. *International Journal of Solids and Structures*, 48(18):2496–2510, 2011.
- [27] H.R. Hertz. über die berührung elastischer körper (on contact between elastic bodies). In *Gesammelte Werke (Collected Works)*. Leipzig, Germany, 1895.
- [28] K.-I. Kanatani. A micropolar continuum theory for the flow of granular materials. *International Journal of Engineering Science*, 17(4):419–432, 1979.
- [29] D. Kolymbas. A rate-dependent constitutive equation for soils. *Mechanics Research Communications*, 4(6):367–372, 1977.
- [30] D. Kolymbas. A generalized hypoelastic constitutive law. In *Proc. XI Int. Conf. Soil Mechanics and Foundation Engineering, Vol. 5*, p2626, 1985.
- [31] E. Kröner. *Mechanics of generalized continua: proceedings of the IUTAM-symposium on the Generalized Cosserat Continuum and the Continuum Theory of Dislocations with Applications, Freudenstadt and Stuttgart (Germany) 1967*. Springer-Verlag, 1968.
- [32] N.P. Kruyt. Statics and kinematics of discrete cosserat-type granular materials. *International Journal of Solids and Structures*, 40(3):511–534, 2003.
- [33] N.P. Kruyt and L. Rothenburg. Micromechanical definition of the strain tensor for granular materials. *Journal of Applied Mechanics, Transactions ASME*, 63(3):706–711, 1996.
- [34] R.S. Lakes. Experiments in cosserat mechanics. page 626, 1985.
- [35] R.S. Lakes and H.C. Park. New experimental methods for cosserat elastic solids. volume 13, pages 334–335, 1985.
- [36] Y. Li, Y. Xu, and S. Jiang. Dem simulations and experiments of pebble flow with mono-sized spheres. *Powder Technology*, 193(3):312–318, 2009.
- [37] C.-L. Liao, T.-P. Chang, D.-H. Young, and C.S. Chang. Stress strain relationship for granular materials based on the hypothesis of best fit. *International Journal of Solids and Structures*, 34(31-32):4087–4100, 1997.

- [38] S. Luding. *Physics of dry granular media*, chapter Collisions & Contacts between two particles. NATO Advanced Study Institutes series. Series E, Applied sciences. Kluwer Academic, 1998.
- [39] S. Luding. *Behavior of Granular Media, Band 9*, chapter About contact force-laws for cohesive frictional materials in 2D and 3D, pages 137–147. Shaker Verlag, Aachen, 2006.
- [40] S. Luding. Cohesive frictional powders: Contact models for tension. *Granular Matter*, 10(4):235–246, 2008.
- [41] L.E. Malvern. *Introduction to the mechanics of a continuous medium*. Prentice-Hall series in engineering of the physical sciences. Prentice-Hall, 1969.
- [42] H.-B. Mühlhaus and I. Vardoulakis. Thickness of shear bands in granular materials. *Geotechnique*, 37(3):271–283, 1987.
- [43] D.C. Rapaport. *The Art of Molecular Dynamics Simulation*. Cambridge University Press, 2004.
- [44] M. Satake. Tensorial form definitions of discrete-mechanical quantities for granular assemblies. *International Journal of Solids and Structures*, 41(21):5775–5791, 2004.
- [45] G.F. Smith. On isotropic functions of symmetric tensors, skew-symmetric tensors and vectors. *International Journal of Engineering Science*, 9(10):899–916, 1971.
- [46] J. Tejchman and E. Bauer. Numerical simulation of shear band formation with a polar hypoplastic constitutive model. *Computers and Geotechnics*, 19(3):221–244, 1996.
- [47] P.A. Vermeer, S. Diebels, W. Ehlers, H.J. Herrmann, S. Luding, and E. Ramm. *Continuous and Discontinuous Modelling of Cohesive-Frictional Materials*. Lecture Notes in Physics Series. Springer, 2010.
- [48] C.-C. Wang. A new representation theorem for isotropic functions: An answer to Professor G. F. Smith’s criticism of my papers on representations for isotropic functions - Part 1. Scalar-valued isotropic functions. *Archive for Rational Mechanics and Analysis*, 36(3):166–197, 1970.
- [49] C.-C. Wang. A new representation theorem for isotropic functions: An answer to Professor G. F. Smith’s criticism of my papers on representations for isotropic functions - Part 2. Vector-valued isotropic functions, symmetric tensor-valued isotropic functions, and skew-symmetric tensor-valued isotropic functions. *Archive for Rational Mechanics and Analysis*, 36(3):198–223, 1970.

- [50] X.T. Wang. *An updated hypoplastic model, its implementation and its application in tunnelling*. PhD thesis, Institute of Geotechnical engineering, University of Natural Resources and Life Sciences, Vienna, 2009.
- [51] W. Wu. *Hypoplastizität als mathematisches Modell zum mechanischen Verhalten granularer Stoffe*. Veröffentlichungen des Institutes für Bodenmechanik und Felsmechanik der Universität Fridericiana in Karlsruhe. Institut für Bodenmechanik und Felsmechanik der Universität Karlsruhe, 1992.
- [52] W. Wu. On simple critical state model for sand. In *Proc. of the seventh Int. Symp. on Numerical Models in Geomechanics-NUMOG, Graz, Austria, Balkeman, 47-52*, 1999.
- [53] W. Wu and E. Bauer. A simple hypoplastic constitutive model for sand. *International Journal for Numerical & Analytical Methods in Geomechanics*, 18(12):833–862, 1994.
- [54] W. Wu and D. Kolymbas. Numerical testing of the stability criterion for hypoplastic constitutive equations. *Mechanics of Materials*, 9(3):245–253, 1990.
- [55] W. Wu and D. Kolymbas. *Constitutive Modelling of Granular Material*, chapter Hypoplastic then and now. Springer, 2000.
- [56] H. Xiao. On symmetries and anisotropies of classical and micropolar linear elasticities: A new method based upon a complex vector basis and some systematic results. *Journal of Elasticity*, 49(2):129–162, 1997.
- [57] F. Yang, A.C.M. Chong, D.C.C. Lam, and P. Tong. Couple stress based strain gradient theory for elasticity. *International Journal of Solids and Structures*, 39(10):2731–2743, 2002.
- [58] H.P. Zhu, Q.F. Hou, Z.Y. Zhou, and A.B. Yu. Averaging method of particulate systems and its application to particle-fluid flow in a fluidized bed. *Chinese Science Bulletin*, 54(23):4309–4317, 2009.